Computational Studies of Semiflexible Polymer Translocation in Nanopore Systems

by

Konstantinos Kastritis

A thesis submitted in partial fulfillment
of the requirements for the degree of

Master of Science in Materials Science

Faculty of Science

Ontario Tech University

Oshawa, Ontario, Canada

August 2019

Thesis Examination Information

Thesis Title: Computational Studies of Semiflexible Polymer Translocation in Nanopore Systems

An oral defense of this thesis took place on August 14, 2019 in front of the following examining committee:

Chair of Examining Committee	Anatoli Chkrebtii
Research Supervisor	Hendrick W. de Haan
Examining Committee Member	William Atkinson
Examining Committee Member	Franco Gaspari
Thesis Examiner	Lennaert van Veen

The above committee determined that the thesis is acceptable in form and content and that a satisfactory knowledge of the field covered by the thesis was demonstrated by the candidate during an oral examination. A signed copy of the Certificate of Approval is available from the School of Graduate and Postdoctoral Studies.

Abstract

The translocation of double stranded DNA (dsDNA) through nanopore systems is a field with rich physics and many promising technological applications. Double stranded DNA is not fully flexible, and the translocation dynamics of semiflexible molecules are not very well understood. In this thesis, in a set of articles, several aspects of translocation with semiflexible polymers in various nanopore systems are explored using molecular dynamics simulations. We look at the effect of the capture process on the tranlocation dynamics of semiflexible chains for standard nanopores in detail. In collaboration with experiment, we use simulations to explore the dynamics of dsDNA in a nanofiltered nanopore device with potential applications in DNA sequencing technology. A secondary use for the nanofiltered nanopore device as an entropic cage for DNA is also examined. Simulations are used to obtain insight into the dynamics of molecules during the trapping phase.

Keywords: polymer; semiflexible; translocation; physics; nanopores

Author's Declaration

I hereby declare that this thesis consists of original work of which I have authored. This is a true copy of the thesis, including any required final revisions, as accepted by my examiners.

I authorize the University of Ontario Institute of Technology to lend this thesis to other institutions or individuals for the purpose of scholarly research. I further authorize University of Ontario Institute of Technology to reproduce this thesis by photocopying or by other means, in total or in part, at the request of other institutions or individuals for the purpose of scholarly research. I understand that my thesis will be made electronically available to the public.

Statement of Contributions

For chapter 3, the EspressoMD software package was used to conduct the simulations. For chapters 2 and 4, a modified version of the HOOMD-blue software package was used as it can be used on GPUs, greatly increasing the speed of the simulations. The modifications were necessary because the software did not support nanopores and the type of electric field we needed. I implemented a nanopore geometry and a position dependent electric field that we could use for the type of simulations usually carried out in the cNab.Lab.

In the article included in chapter 2, I set up and conducted all the simulations. I modified the HOOMD-blue software package and implemented a nanopore as well a position dependent electric field, neither of which are included by default in the package. I analyzed all the data to produce the figures in the document, and interpreted the results. My co-authors, Martin Magill and Hendrick de Haan, assisted with the interpretation of the results, and helped edit my draft of the manuscript.

The work in Chapter 3 has been published as:

Kyle Briggs, Gregory R. Madejski, Martin Magill, Konstantinos Kastritis, Hendrick W. de Haan, James L. McGrath, Vincent Tabard-Cossa *DNA Translocations through Nanopores under Nanoscale Preconfinement* **ACS Nano Letters 18 (2017), no. 2, 660-668.**

For this article I carried out the simulation work and the initial modelling. Along

with Martin Magill and Hendrick de Haan, I interpreted the results and their relation to the experimental work. I wrote a draft of the simulation sections in the article and assisted in editing the entire manuscript. I helped edit the supplementary information that can be found in Appendix A.

The work in Chapter 4 has been published as:

Michelle H. Lam, Kyle Briggs, Konstantinos Kastritis, Martin Magill, Gregory R. Madejski, James L. McGrath, Hendrick W. de Haan, Vincent Tabard-Cossa *Entropic Trapping of DNA with a Nanofiltered Nanopore* **Accepted for publication in ACS Applied Nano Materials**

In this work I conducted all the simulations, as well as the modelling of the device. I analyzed the results and interpreted them along with my co-authors. I analyzed the TEM images of the device using software developed by collaborators at the McGrath group at the University of Rochester. I wrote the simulation sections, and the image analysis sections of the manuscript. I also wrote the simulation section in the supplementary information (Appendix B). I assisted in editing the entire document.

Acknowledgements

I would like to thank my supervisor, Dr. Hendrick de Haan, for his invaluable guidance and the many opportunities he gave me during my Master's Degree. I would also like to thank my supervising commitee, Dr. Bill Atkinson and Dr. Franco Gaspari, as well as the external reviewer, Dr. Lennaert Van Veen. I am also thankful to the members of the cNab.Lab for the help and support they provided over the course of this degree. Finally, I am very thankful to my family for supporting me throughout my academic endeavours.

Contents

List of Figures

Chapter 1

Introduction

This thesis is a collection of three articles that each study some aspect of the passage of semiflexible chains in nanopore systems. Two of the manuscripts presented are already published, with the third ready to be submitted for publication. Because of this, the first chapter is written with the intent to prepare the reader for the bulk of the thesis as the papers are written in standard article format and assume certain knowledge common to the field.

1.1 Nanopore Translocation

1.1.1 Nanopores

Nanopores are abundant in biological systems as they form the basis for the transport of molecules across phospholipid bilayers and cell membranes. As the name implies, nanopores are nanoscopic holes in a surface and they are usually formed by proteins that are embedded in a bilayer. In 1996 Kasianowicz et al. [19] demonstrated that molecules could be manipulated and monitored during its passage through an α-hemosylin protein channel. Their work paved the way for the study of passage

and detection of single molecules through nanometric channels. Since then, the α-hemosylin nanopore has been the target of extensive study. These types of nanopores are referred to as biological nanopores.

Nanopores can also be manufactured synthetically with a variety of methods [33, 11]. Although the details of each method are different, functionally they all lead to a nanometric hole in membrane. The materials used for these nanopores are usually silicon based with silicon nitride (SiN) being the most common. To contrast biological nanopores these are reffered to as solid-state nanopores.

1.1.2 Polymers

The primary interest in the study of nanopore systems lies in the detection and manipulation of polymers in solution. Polymers are structures formed by the repeated linking of units called monomers. Although monomers can be linked in a variety of ways [37], in this thesis we will be focusing on linear polymers.

In linear polymers, as shown in Figure 1.1, the monomers are linked in such a fashion that they form a chain with two free ends. A famous example of a linear polymer is the molecule fundamental to life as we know it, deoxyribonucleic acid (DNA). DNA exists as single stranded DNA (ssDNA) and double stranded DNA (dsDNA). The monomers in DNA are the primary bases adenine, thymine, guanine, uracil. The length of DNA is measured in terms of the bases. For instance, the length of double stranded DNA is measured in the number of base pairs (bp) that make up the molecule. The topologies of the two different variants are quite different with the famous double helix structure of dsDNA making it far more rigid than ssDNA. While both DNA variants are used in nanopore translocation experiments, the primary focus in literature is on dsDNA [42, 27].

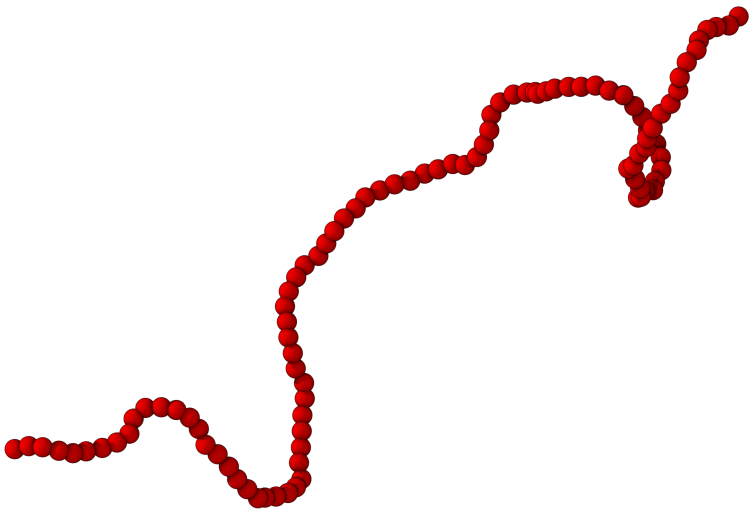

Figure 1.1: A ball-and-stick example of a linear polymer. The monomers are joined together to form a deformable chain.

1.1.3 Driven Polymer Translocation

The process of moving a DNA molecule across a hole in a membrane is known as nanopore translocation. Most standard nanopore systems are comprised of two chambers (called *cis* and *trans*) separated by a membrane containing the pore (shown in figure Figure 1.2). Polymers are placed in the cis chamber and must pass to the trans chamber. The passage of a polymer through a nanopore is called translocation. Usually, translocation does not occur spontaneously as it is more entropically favourable for the molecule to remain in free solution. Thus, some force is needed to pull the polymer from the cis side of the membrane to the trans side of the membrane. Translocation can be achieved in several ways each with their own mountain of literature [42]. In this thesis we shall focus on translocation driven by electric fields.

The basic idea of driven translocation is as follows: Consider a device containing fluid with some salt (usually potassium chloride) housing two chambers separated by

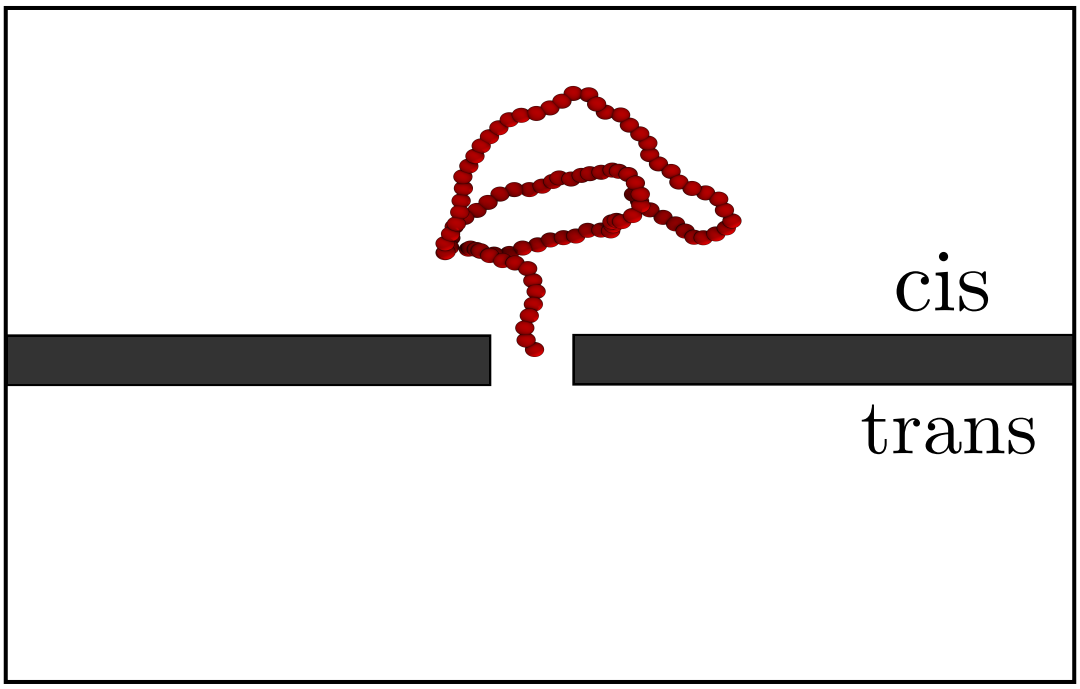

Figure 1.2: A schematic representation of a nanopore system. The linear polymer begins on the *cis* side of the membrane in some configuration before it is driven to the *trans* side.

a membrane with a nanopore. The application of a voltage drop across this device allows for the detection of ion flow through the nanopore via measurement of its conductance. As a molecule enters the nanopore and reduces the ion flow the current changes, thus allowing for a measurement of how long the molecule remained inside the channel and what type of molecule entered the channel [28].

1.1.4 Nanopore Applications

The most well known application of nanopores is in DNA sequencing. The idea behind sequencing is to linearly read the sequence of base pairs in the DNA. Perhaps the most notable example is DNA profiling in criminal investigations, where being able to identify and match DNA sequences is vital to resolving the case [24]. Another

notable use of nanopore sequencing that has recently become very popular is personalized ancestry and health predisposition reports. Companies like 23andMe and AncestryDNA provide genome sequencing services for relatively small fees. They use existing markers to analyse a customers DNA and determine their ancestral DNA composition as well as the impact of their genetic makeup on their health.

In addition to sequencing there are other nanopore applications that are still being worked on in scientific research and have yet to be commercialized. Some of those applications are sorting DNA and proteins by length [31, 34, 23], single molecule manipulation for studying nanoscopic biological processes [22, 39], detecting concentrations of molecules in solution [17], and many more [27].

1.2 Concepts from Statistical Physics

Before surveying the literature for simulations of the translocation of semiflexible polymers it is important to review some concepts from statistical and polymer physics. In this section we will briefly review several notions from statistical physics, including diffusion, the Langevin equation, and the relation between dissipation and fluctuations.

1.2.1 The Diffusion Equation - Brownian Motion

If we consider a spherical particle in a thermal bath with no external forces, the evolution of its probability density (PDF) in one spatial dimension can be described by the following partial differential equation (PDE)

$$\frac{\partial}{\partial t}p(x,t) = D\frac{\partial^2}{\partial x^2}p(x,t), \tag{1.1}$$

where D is the diffusion coefficient and $p(x,t)$ is the probability density of finding the particle at any point in space and time. The diffusion coefficient may also have spatial and temporal dependence, but for our purpose we consider the case of the diffusion coefficient being a constant. The rationale behind this equation is that the motion of a particle in such a thermal bath is caused by very frequent collision with the fluid molecules of the bath. Given the great complexity of the motion the classical equations are intractable analytically and a probabilistic approach is more fruitful.

Assuming the system is not bound in any spatial direction (i.e. it is infinite), then with $p(x,0) = \delta(x)$ as an initial condition (where δ is the Dirac delta function) the above PDE can be solved to obtain

$$p(x,t) = \frac{1}{\sqrt{4\pi Dt}} \exp(-x(t)^2/4Dt). \tag{1.2}$$

From this PDF it can be shown [4] that the variance in the position of the particle is

$$\langle x^2 \rangle - \langle x \rangle^2 = \langle \Delta x^2 \rangle = 2Dt. \tag{1.3}$$

In Equation 1.3, we see that the diffusion coefficient is related to the spreading of the particles position i.e. the variance of its displacement. The quantity $\langle \Delta x^2 \rangle$ is appropriately called the mean squared displacement. This was the result that Einstein arrived at in the early 20th century that lay the foundations of the mathematical description of Brownian motion.

1.2.2 A Stochastic Description of Brownian Motion

Another approach, and one more relevant to this thesis, comes from a special version of Newtons second law. The goal of this section is to review some details regarding

diffusion, the Langevin equation, and the relation between fluctuations and dissipation.

The classical equations of motion for a particle moving around in a thermal bath quickly become intractable, as the motion of the the particle is coupled to the motion of the myriad fluid molecules. However, using ideas from statistical mechanics we can modify the classical equations and render them much simpler. Instead of solving the classical equations for every collision between the fluid molecules and the Brownian particle, we can treat the bath as a continuous fluid and encode the effects of the collisions into an effective force acting on the Brownian particle. Assuming that the fluid is described by classical fluid dynamics, the equation of motion for the Brownian particle can be neatly written as

$$m\ddot{x} = F_{\text{drag}} + F_{\text{thermal}}, \tag{1.4}$$

where F_{drag} is the drag force imparted by the fluid, and F_{thermal} is the force that contains the net effect of collisions with fluid molecules. In the following sections we will discuss the form that these forces take.

1.2.2.1 Dissipation - Drag in a Viscous Fluid

Objects moving through fluids experience a drag force that affects their motion. The drag felt by an object is a function of its speed relative to the fluid flow. The strength of the drag force relative to the fluid flow is characterized by the Reynolds number, the dimensionless ratio between the force of drag and inertia

$$\text{Re} = \frac{\rho v L}{\mu}, \tag{1.5}$$

where ρ is the density the fluid, μ is the dynamic viscosity of the fluid, v is the characteristic speed of the object, and L its characteristic length.

In viscous flows with low Reynolds number, the drag force is a linear function of the velocity of the object in the fluid

$$F_{\text{drag}} = -\zeta \dot{x}, \tag{1.6}$$

where $\dot{x}$ is the velocity, and ζ is the drag coefficient. In the case of spherical objects moving through a viscous fluid the drag coefficient is given by Stokes's Law

$$\zeta = 6\pi\mu r, \tag{1.7}$$

where r is the radius of the spherical object.

1.2.2.2 Fluctuation - Thermal Noise

Random collisions due to the fluid molecules being in constant motion impart some momentum on the Brownian particle. Although the net displacement due to these collisions will average out to zero over time, their existence at any single moment in time is paramount for the description of the Brownian particles motion.

The effect of these collisions is modelled as thermal noise described by a stationary Gaussian process, $R(t, T)$, that satisfies

$$\langle R(t, T) \rangle = 0, \tag{1.8}$$

$$\langle R(t, T) R(t', T) \rangle = B(T)\delta(t - t'), \tag{1.9}$$

where $B(T)$ is a function of temperature who value determines the magnitude of the

fluctuations in the thermal noise. In other words, this function is independent at every moment in time, and zero when averaged over time. The random force describing the net effect of the collisions is then simply

$$F_{\text{thermal}} = R(t, T) \tag{1.10}$$

1.2.3 The Langevin Equation

Combining Equation 1.6 and Equation 1.10 we arrive at the following equation of motion

$$m\ddot{x} = -\zeta\dot{x} + R(t, T). \tag{1.11}$$

This is the second order Langevin equation (LE)[21], an example of a stochastic differential equation.

The LE can be solved as a first order inhomogeneous differential equation yielding

$$\dot{x}(t) = \dot{x}(0)\exp(-\zeta t/m) + \frac{1}{m}\int_0^t dt' \exp(-\zeta(t-t')/m)R(t', T). \tag{1.12}$$

The second term of this equation is a stochastic integral. These types of integrals can be interpreted (using the central limit theorem) as normal distributions with some mean and variance. As such, we will take ensemble averages and examine the resulting behaviour. By averaging Equation 1.12 and taking the properties of the noise term into account we find

$$\langle\dot{x}(t)\rangle = \langle\dot{x}(0)\rangle\exp(-\zeta t/m). \tag{1.13}$$

This is an unsurprising result; when the thermal noise is absent we recover the equa-

tions of damped motion. Due to the character of the fluctuations in the noise, it is the averages of the squared velocity and position that provide deeper physical insight.

From Equation 1.12 we can write the ensemble average of the squared velocity

$$\begin{aligned}\langle \dot{x}(t)\dot{x}(t)\rangle = &\langle \dot{x}(0)\dot{x}(0)\rangle \exp(-2\zeta t/m) \\ &+ \frac{2}{m}\int_0^t dt' \langle \dot{x}(0)\rangle \exp(-\zeta(2t-t')/m)\langle R(t',T)\rangle \\ &+ \frac{1}{m^2}\int_0^t dt' \int_0^t dt'' \exp(-\zeta(2t-t'-t'')/m)\langle R(t',T)R(t'',T)\rangle.\end{aligned} \tag{1.14}$$

From the properties of the random force (Equation 1.8), the middle term becomes zero and the last term is simplified thus leading to

$$\langle \dot{x}(t)\dot{x}(t)\rangle = \left(\langle \dot{x}(0)\dot{x}(0)\rangle - \frac{B}{2\zeta m}\right)\exp(-2\zeta t/m) + \frac{B}{2\zeta m}. \tag{1.15}$$

Taking the appropriate long time limit ($t \to \infty$) the expression becomes

$$\langle \dot{x}(t)\dot{x}(t)\rangle = \frac{B}{2\zeta m}, \tag{1.16}$$

which can be interpreted as the mean kinetic energy of the system. Equation 1.16 shows that at long times any kinetic energy is entirely due to the momentum imparted by random collisions, but we have yet to determine what B is. From equilibrium statistical mechanics we know that the mean kinetic energy of a particle should reach the value dictated by the equipartition theorem

$$\frac{1}{2}m\langle \dot{x}^2\rangle = \frac{1}{2}k_{\mathrm{B}}T, \tag{1.17}$$

where k_{B} is Boltzmann's constant, and T is the equilibrium temperature. Thus,

combining Equation 1.16 and Equation 1.17 we obtain the remarkable result

$$B = 2k_{\mathrm{B}}T\zeta. \tag{1.18}$$

The strength of the thermal fluctuations is coupled to the drag experienced by the Brownian particle. This result is a special case of the Fluctuation-Dissipation theorem, which states that whenever energy is dissipated by a process there is a corresponding fluctuation that transforms thermal energy into kinetic energy.

Although the details are beyond the scope of this thesis, the variance of the position in the long time limit can be similarly shown to be

$$\langle \Delta x(t) \Delta x(t) \rangle = 2\frac{k_{\mathrm{B}}T}{\zeta}t[7], \tag{1.19}$$

from which, by simple comparison with Equation 1.3, we can see that the diffusion coefficient is

$$D = \frac{k_{\mathrm{B}}T}{\zeta}. \tag{1.20}$$

This result is known as the Einstein relation and is yet another example of the Fluctuation-Dissipation theorem.

1.3 Introduction to Polymer Physics

In the previous section we discussed some results from statistical physics related to the motion of a single particle in a viscous fluid. In this section we will briefly review some notions from polymer physics and the motion of many interacting particles in solution. Given the simulation based nature of the content in this thesis, we will focus on linear polymer models that can be implemented numerically. The interested reader

may refer to these books[12, 8] that offer a more in-depth theoretical description of polymers.

Polymers are chains of many subunits, called monomers, bonded together. A polymer chain is always found in a bath of solvent (usually water) and will adopt random shapes due to interactions with the solvent. The shape of a polymer chain is commonly known as its conformation. The chain models in polymer physics are designed to capture topological features of the macromolecules often encountered in biology and chemistry while remaining simple enough so that they can be studied by the usual tools of physics. Simulations use discrete polymer models that are often called bead-spring models as they model macromolecules with spherical beads connected by springs. In the following sections we will review some common models of polymer physics.

1.3.1 Descriptions of Chain Conformation

Before discussing any specific chain model, it is important to quantify the notion of size for polymers. Intuitively, the total length of a chain of N monomers, called the contour length (L_c), measures the size of the polymer. Assuming all bonds in the chain have the same length, the contour length can be shown to be $L_c = bN$, where b is the bond legth. However, as we saw in the previous section, particles in a fluid bath will experience constant random collisions with the fluid molecules. Thus, the conformation of the polymer is constantly changing as the monomers interact with the solvent and therefore requires a statistical description. That being said, the contour length is appropriate for extremely rigid polymers that behave like rods.

If we consider a chain of N identical monomers there are two primary quantities used to measure the dimensions of any given conformation. The first quantity is the end-to-end distance (L_E), which is the difference between the coordinates of the end

monomers of the chain. In equilibrium, the average displacement between the end monomers is zero as the conformations a polymer can take are isotropic. However, L_{E} is a distribution across all conformations and while its mean is zero, its variance is given by

$$\langle L_{\mathrm{E}}^2 \rangle = \langle (\mathbf{r}_{\mathrm{N}} - \mathbf{r}_0)^2 \rangle, \tag{1.21}$$

where $\mathbf{r}_{\mathrm{N}}$ and $\mathbf{r}_0$ are the positions of the monomers at the two ends of the chain. The square root of Equation 1.21 can be roughly interpreted as the diameter containing most of the chain segments. It is worth noting that the end-to-end distance is not always a good measure of instantaneous chain size as the end monomers can be very close to each other, leading to very small end-to-end distances, while the chain is actually extended.

The second quantity is the radius of gyration. The square of the radius of gyration is the spread of monomer positions relative to the center of mass (COM) of the chain (i.e. the second moment of the monomer position distribution)

$$R_{\mathrm{g}}^2 = \frac{1}{N+1} \sum_{i=0}^{N} \langle (\mathbf{r}_i - \mathbf{r}_{\mathrm{COM}})^2 \rangle, \tag{1.22}$$

where $\mathbf{r}_i$ is the position of the ith monomer, $\mathbf{r}_{\mathrm{COM}}$ is the COM of the chain, and N is the total number of monomers. In other words, the chain can be thought of occupying a volume of a sphere of radius R_{g}, which makes the radius of gyration a very useful measure of polymer conformation. Note that care must be taken when interpreting the conformation of a chain as a sphere with radius given by the average value of the radius of gyration. Over all conformations the chain is isotropic, but the instantaneous shape of the polymer at any moment in time can be anisotropic [37, 12].

The difference between L_{E} and R_{g} is shown in Figure 1.3.

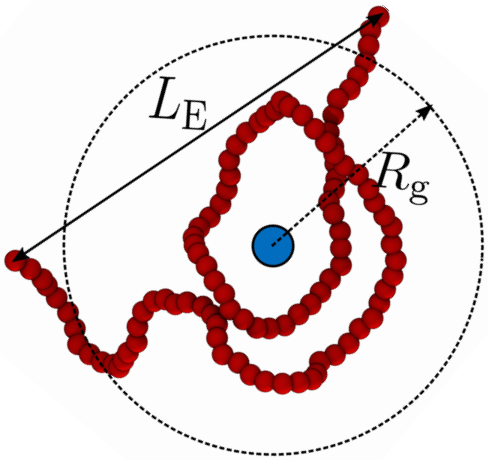

Figure 1.3: Schematic illustrating the difference between the size of the chain as given by the radius of gyration and the end-to-end distance. The blue circle represents the center of mass of the chain. The dashed circle is that formed from the radius of gyration.

1.3.2 Ideal Chains

The simplest representation of linear polymer molecules is the so called ideal chain. In this model, N identical monomers are bonded together to form a chain with interactions defined only between adjacent monomers. The ideal chain is analogous to an uncorrelated random walk in which each step is a bond between monomers. The average of the coordinate difference between the end monomers ends up being zero, but the square can be averaged over all conformations to obtain the end-to-end distance

$$\langle L_{\mathrm{E}}^2 \rangle = b^2 N. \tag{1.23}$$

The squared radius of gyration averaged over all conformations for an ideal chain can be shown [37, 12] to be

$$\langle R_{\mathrm{g}}^2 \rangle = \frac{b^2 N}{6}. \tag{1.24}$$

This chain model is often called the freely jointed chain.

1.3.3 Real Chains

In reality, polymers are under constraints that strongly influence their available conformations. These constraints come in the form of excluded volume effects which originate from the fact that real molecules cannot overlap, as is possible for non-adjacent monomers in the ideal chain. The net effect is that the available free volume for the chain is smaller than the volume of the system containing the polymer. As such, real polymer chains are swollen compared to the ideal chains, making them self-avoiding random walks. In real chains, the average radius of gyration can be shown to scale as

$$R_{\mathrm{g}} \sim b N^{\nu} [37], \tag{1.25}$$

where ν is called the Flory exponent. The average end-to-end distance can be found to scale in the same way. This chain model is commonly referred to as the freely jointed chain with excluded volume. The value of the Flory exponent can be calculated to be $\nu \approx 0.588$ [37, 12, 38] for 3 dimensions. In particular, this value of the flory exponent is for a good solvent, where the polymer can be fully dissolved and the excluded volume interactions are strong [37]. There are a few ways to carry out the calculation of the exponent. A simple argument by Flory himself involves computing the effective free energy of the entire chain and then minimize that with respect to the radius of gyration [14]. This method provides a good estimate for the exponent. A more precise approach makes use of the renormalization group theory. In essence, one

can self-consistently rescale the free energy of the chain and obtain a set of equations that can be solved to give the Flory exponent [38]. The details of these calculations are beyond the scope of the thesis.

1.3.4 Semiflexible Chains

So far in our discussion of chain models we have neglected the rigidity in the backbone of the polymer. A famous example of a semi-rigid biopolymer is double stranded DNA, the subject of a lot of experimental studies in nanopore translocation [42]. As such, it is important to consider the case where a polymer is not completely rigid (i.e. a rod) nor completely flexible (the freely jointed chain) but instead semiflexible.

Rigidity can be introduced to the ideal chain in the form of angular correlations between consecutively bonded monomers. The most common discrete model for doing so is the Kratky-Porod model [12], also known as the wormlike chain (WLC) though the latter name is more commonly used for the continous version. In this thesis we will be using the two terms interchangeably to mean a semiflexible chain model.

The average squared radius of gyration of a semiflexible chain can be shown to be

$$\langle R_{\mathrm{g}}^2 \rangle_{\mathrm{WLC}} = \frac{1}{3} L_{\mathrm{c}} \ell_{\mathrm{p}} - \ell_{\mathrm{p}}^2 + 2\frac{\ell_{\mathrm{p}}^3}{L_{\mathrm{c}}} - 2\frac{\ell_{\mathrm{p}}^4}{L_{\mathrm{c}}^2}\Big[1 - \exp\big(-L_{\mathrm{c}}/\ell_{\mathrm{p}}\big)\Big] [37], \tag{1.26}$$

where ℓ_{p} is the length at which the correlations between consecutive monomers decay. This correlation length is most commonly called the persistence length of the chain. This expression is significantly more complicated than the one for the ideal chain, making semiflexible chains harder to treat theoretically. The end-to-end distance for the wormlike chain is similarly complicated and can be shown to

$$\langle L_{\mathrm{E}}^2 \rangle = 2\ell_{\mathrm{p}} L_{\mathrm{c}} \left[1 - \frac{\ell_{\mathrm{p}}}{L_{\mathrm{c}}}\left(1 - \exp\big(-\frac{L_{\mathrm{c}}}{\ell_{\mathrm{p}}}\big)\right)\right] [37]. \tag{1.27}$$

It can be shown that taking the limit of infinite and zero persistence length in the expressions above recovers the behaviour of rods and ideal chains, respectively.

A very useful connection between semiflexible and ideal chains is the notion of the Kuhn length. The Kuhn length is defined as the effective bond length at which the segments of a semiflexible chain with N monomers behave as if they were ideal. The criterion for such behaviour is that the end-to-end distance is given by $\langle L_{\mathrm{E}}^2 \rangle \sim N_{\mathrm{k}}$, where N_{k} is the number of Kuhn segments. The Kuhn length (ℓ_{k}) can be found to be equal to twice the persitence length, $\ell_{\mathrm{k}} = 2\ell_{\mathrm{p}}$ [37]. The number of Kuhn segments can be obtained from $N_{\mathrm{k}} = \frac{N}{\ell_{\mathrm{k}}}$.

1.3.5 Electrostatics of Polymers in Solution

The polymer models discussed so far make no explicit mention of charges. The electrostatics in the solvent affect the motion of polymer regardless of any bare charge on the molecule. The goal of this section is to briefly describe the role of electrostatics in polymer solutions.

As mentioned before, the nanopore and the polymer exist in a bath of solvent. For translocation experiments, the solvent is usually water and some salt (most commonly KCl and LiCl). The solution of water and salt is overall neutral. However, the ions from each constituent molecule of the salt dissociate due to the polar nature of water, resulting in charge distributions that have long range correlations (due to electrostatics). Adding an object to this solution (such as a nanopore or a polymer) causes ions to adsorb to the surface of the object due to chemical reactions. Following that, ions of opposite charge to those adsorbed on the surface create a layer at the interface of the object and the solvent, and oppositely charged ions remain near the interface. In particular, for a polymer in solution an ion cloud is formed around the charges of the molecule thereby shielding the interactions between monomers.

These solutions are characterized by two different length scales over which electrostatic interactions take place. The first length scale is the Bjerrum length, ℓ_{B}. This length is the distance at which the electric energy between two charges is equal to the thermal energy. If the inter-ion distance is greater than ℓ_{B}, their interaction strength would be weaker. Conversely, if the distance is smaller, their interaction strength would be stronger. The Bjerrum length is an intrinsic property of the solvent and depends strongly on the dielectric constant. For water solutions the Bjerrum length is approximately $\ell_{\mathrm{B}} \approx 0.7\,\mathrm{nm}$ [26].

The second characteristic length scale is the Debye length, ℓ_{D}. The Debye length is the correlation length for ion-ion interactions. For charged objects in these solutions, the Debye length is comparable to the thickness of the ion cloud formed by the charges attempting to minimize their local energy (i.e. they try to pair up with opposite charges). When the distance from the interface is larger than the Debye length, the effect of the ion cloud is no longer present. The Debye length depends on the dielectric properties of the solvent.

The details of the charge distribution on the polymer itself are quite complicated. The effective polymer charge due to ionization depends on many variables such as the flexibility of the chain, the size of the ions in the solvent, the local dielectric constant near the chain, the dielectric constant of the solvent, and temperature [26]. In essence, ions of opposite charge (called counterions) adsorb on the polymer creating a counterion worm [26] that accompanies the chain. When the polymer is subject to changes due to an external electric field, the counterion worm moves in the opposite direction to the polymer, due to their opposite changes, and a new counterion worm envelops the chain. This is an example of electrohydrodynamics (EHD) at play.

Translocation experiments are conducted in the high salt concentration limit. Conveniently, in the high salt concentration limit ($c_{\mathrm{salt}} \approx 0.1 - 1\,\mathrm{M}$[26]), the electro-

static interactions between segments of the chain turn out to be short ranged, and thus can be subsumed into the exluded volume of each monomer.

1.3.6 Polymer Dynamics in Solution

In this section we will review some of the dynamical properties of polymers in solution. In particular, we will focus on the effective drag experienced by the polymer.

As we saw in subsection 1.2.3, particles in free solution will diffuse with a diffusion coefficient dictated by the Einstein relation (Equation 1.20). There are two commonly used models for relating the diffusion of each constituent monomer to the diffusion coefficient of the center of mass of the chain. The first model is called the Rouse model. In this theory, hydrodynamic interactions between different parts of the chain are neglected. The Rouse model predicts that, in the absence of hydrodynamics, the drag coefficient of an N monomer chain is simply the sum of the drag coefficients experienced by the monomers

$$\zeta_{\text{Rouse}} = N\zeta. \tag{1.28}$$

The second model is known as the Zimm model. In Zimm's theory the effect of hydrodynamic interactions between the monomers and the fluid is included directly in the equations of motion by the Oseen tensor [37]. In particular, in Zimm's approach the hydrodynamics are pre-averaged so that tensor may be decoupled from the equations of motion [37]. The Zimm theory posits that the chain drags some of the fluid in its vicinity with it as it moves. Through scaling arguments, the theory predicts that the drag coefficient experienced by a chain of N monomers is

$$\zeta_{\text{Zimm}} \sim N^{\nu}\zeta, \tag{1.29}$$

where ν is the Flory exponent. From this scaling relation we see that long chains diffuse faster in the Zimm model than the Rouse model.

The Zimm model is more accurate for describing the motion of chains in free solution in the absence of external forces. However, in the presence of an electric field it is the Rouse model that accurately captures the diffusion of the polymer. The reason for this is the electric field results in screening of the long range hydrodynamic effects between distant parts chain [26]. This occurs due to the counterion worm described in the previous section. As the electric field moves the counterions around, water is dragged with them resulting in a disruption of the long range effects due to the fluid. In fact, this is the underlying mechanism for the famous free draining property of DNA.

1.4 Molecular Dynamics Simulations

In the previous section several physical notions from statistical physics and polymer physics were introduced. This section will present the methods used for implementing numerical simulations of semiflexible polymers.

Molecular dynamics (MD) is based on the idea that in classical Newtonian mechanics we can use arbitrary potential functions to model any physical process involving particles. MD simulations consist of numerically solving the classical equations of motion[2]

$$\frac{\partial \mathbf{x}_i}{\partial t} = \mathbf{v}_i, \tag{1.30}$$

$$\frac{\partial \mathbf{v}_i}{\partial t} = \frac{\mathbf{F}_i}{m_i}, \tag{1.31}$$

where i is an integer particle index in the range $[0, N)$, m_i is the mass of the ith particle, and $\mathbf{F}_i$ is the force acting on the ith particle due to all interactions in the system.

Molecular dynamics is a very robust computational method and can be used to model systems at all scales. It is commonly used to model biological and chemical systems at atomic length scales, at the limits of experimental resolution.

The biological systems in this thesis consist of polymers, solvent, and nanopores. Although it is possible to represent all of these in remarkable atomic detail, the simulations quickly become computationally intractable as the number of atoms, and therefore the computational complexity, increase.

1.4.1 Coarse-Graining

In normal MD, every solvent molecule interacts with every particle, which is very computationally expensive at the system sizes we are intested in. So, in this thesis, we will use models that are intricate enough to capture the complexity of polymer interactions in nanopore systems while still remaining computationally feasible to simulate. The polymers will be coarse-grained to chains of monomers with their solvent interactions implicit to the equations of motion. In addition, membranes and nanopores will be abstracted to reflecting boundary conditions.

1.4.2 Langevin Dynamics

Langevin dynamics is a modified MD approach to model physical systems. The core notion is that by the use of stochastic differential equations, models with little detail can be used to simulate a physical system while simultaneously accounting for any omitted complexity.

In Langevin dynamics, the solvent is approximated as a fluid that models the interactions between solvent molecules and particles. For nanopore systems the interactions of interest are the dissipation of energy via drag, and thermal fluctuations. To this effect, the second-order Langevin equation (Equation 1.11) is used. In subsection 1.2.2 the Langevin equation was presented in one dimension to illustrate the relevant physics, however the simulations are conducted in three dimensions, thus the Langevin equation reads

$$m\ddot{\mathbf{x}} = \sum_i \nabla U_i - \zeta\dot{\mathbf{x}} + \sqrt{2\zeta k_{\mathrm{B}}T}\boldsymbol{\xi}(t). \tag{1.32}$$

For practical convenience, the random term has been decomposed into its magnitude and a three dimensional stationary Gaussian process, $\boldsymbol{\xi}(t)$, with each component independent of the others

$$\langle \xi_i(t) \rangle = 0 \tag{1.33}$$

$$\langle \xi_i(t)\xi_j(t') \rangle = \delta_{ij}\delta(t-t'), \tag{1.34}$$

where δ_{ij} is the Kronecker delta. The gradient term is the sum of all external forces acting on the particles in the system.

1.4.3 Coarse-Grained Polymers

In this section we will construct a coarse grained polymer as a chain of monomers using forces. All of the forces used to create the polymer can be obtained by taking the gradient of a potential $\mathbf{F} = -\nabla U$. Thus, for convenience and for parity with literature, the forces will be discussed in terms of the potentials that generate them.

In this thesis, bonds betweens pairs of monomers will be modelled using the finitely

extensible non-linear elastic (FENE) potential

$$U_{\mathrm{FENE}}(r) = -\frac{1}{2}kr_{\mathrm{max}}^2 \ln\left(1 - \frac{r^2}{r_{\mathrm{max}}^2}\right), \tag{1.35}$$

where r is the center to center distance between the bonded monomers, and the constants k and r_{max} represent the stiffness and the maximum possible extension of the bond, respectively. While a Hookean spring ($U_{\mathrm{Hook}} = \frac{1}{2}kr^2$) could in principle be used, the FENE potential is found to be a better model for the behaviour of real polymers. A Hookean spring would allow the bonds to far exceed their equilibrium length without the force diverging (i.e. the bond breaking) whereas in FENE, the energy needed to stretch the bond beyond the maximum possible extension diverges to infinity. In reality, excessive stretching of the polymer results in the chemical bonds between its constituents breaking, and thus the FENE potential is more physically sound.

To model the excluded volume effect described in the polymer physics section, we will use a truncated and shifted Lennard-Jones (LJ) potential called the Weeks-Chandler-Andersen potential (WCA)

$$U_{\mathrm{WCA}}(r) = \begin{cases} 4\epsilon\left[\left(\frac{\sigma}{r}\right)^{12} - \left(\frac{\sigma}{r}\right)^{6}\right] + \epsilon & r < r_c \\ 0 & r \geq r_c \end{cases}, \tag{1.36}$$

where r is the center to center distance between the interacting monomers, ϵ is the interaction strength, σ the monomer diameter, and r_c the cut-off distance, whose value is set to the minimum of the LJ potential at $r_c = 2^{1/6}\sigma$. Like in the LJ potential, the first term exists to prevent overlapping particles and the second term is a phenomenological scaling relation that accounts for the van der Waals forces (the instantaneous dipole induced interactions) between particles.

In contrast to the LJ potential, the WCA potential only models the repulsive interactions between particles. The choice of cut-off in the interaction radius means that the monomers are not hard spheres but instead soft spheres of slightly larger effective radius. The reason for this choice is that pure hard sphere interactions would cause the potential to diverge upon edge-to-edge contact between monomers (which occurs at $r = \sigma$), leading to discontinuous forces. In other words, hard sphere monomers would feel no force while the monomers are separated by more $1\,\sigma$ and then instantaneously feel an incredibly large force. Resolving this behaviour would require an incredibly fine discretization of time (i.e. a really small time step) or defining some elastic collision between the hard spheres. For simulations such as the ones in this thesis, it is much more desirable to define continuous forces. A comparison between the two potentials is shown in Figure 1.4.

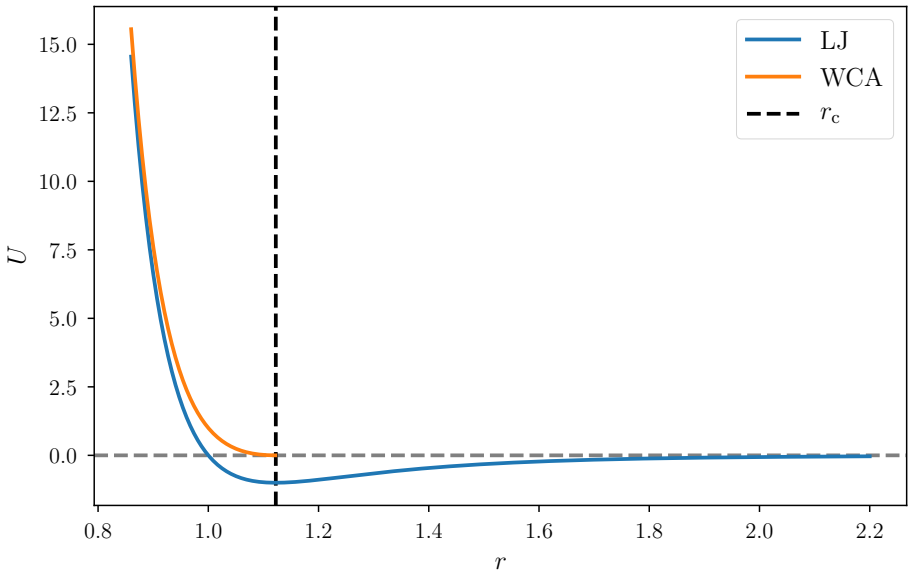

Figure 1.4: Comparison between the LJ and WCA potentials. The grey dashed line represents the line at $U = 0$. The black dashed line corresponds to the location of the minimum in the LJ potential at $r = r_c$.

The semiflexibility of the polymer will be modelled using a harmonic three body

potential

$$U_{\text{angle}}(\theta) = \frac{1}{2} k_{\text{angle}} \theta^2, \tag{1.37}$$

where the angle θ is the angle formed by three consecutive monomers, and k_{angle} is the stiffness of the spring. This potential ensures that there is an energetic cost for deviating from a rest angle of π radians. The stiffness of the angle bond can be related to the persistence length of the polymer via $\ell_{\text{p}} \approx \frac{k_{\text{angle}}}{k_{\text{B}}T}$ [20], thus the persistence length of the chain can be modified by varying the stiffness of the angle bond. The net effect of WCA, FENE, and the angle potential is shown schematically in Figure 1.5.

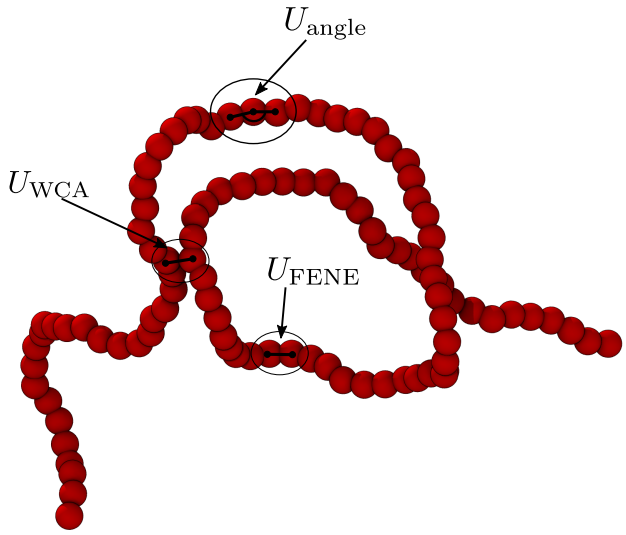

Figure 1.5: Schematic illustration of the WCA, FENE, and harmonic angle potentials on a coarse-grained polymer.

1.4.4 Simulation Details

The simulations in this thesis operate in a self-consistent set of units with distance, mass, and energy as fundamental. The unit of energy (ϵ) will be taken to be the thermal energy, $k_{\mathrm{B}}T$, with the units of mass and length will be taken to be the monomer diameter(σ) and mass (m), respectively.

1.4.4.1 Electrostatics in the Simulation

Each monomer in the simulations is assumed to have unit charge. We make the assumption that the Debye length is covered by the excluded volume interaction, thus placing our polymers in a high salt concentration solvent. This means that the only electrostatic force on the monomers is the one directly exerted by the electric field.

1.4.4.2 Dynamics in the Simulation

The dynamics of the coarse-grained polymer in the simulations in this thesis are described by the Rouse theory, as the solvent is implicit and there are no long range hydrodynamic interactions between different parts of the chain. This means that the center of mass diffusion of the chain is given by

$$D_{\mathrm{COM}} = \frac{k_{\mathrm{B}}T}{N\zeta}. \tag{1.38}$$

1.4.4.3 Tuning Simulations to Experiment

We can tune certain aspects of the simulation to match experimental conditions. For example, setting the monomer width fixes all other length scales in the system since they are all expressed in units of σ. However, matching the voltage (and therefore the electric field strength) is slightly more complicated as it plays a role in the drift-

diffusion balance in the system and can't be directly set by deriving the appropriate unit using mass, energy, and length. If we were to derive the voltage directly we would have to tune the effective charge density on the chain, which would then inform the effect the field has on the polymer. However, as noted in the solution electrostatics section previously, getting the charge distribution on the polymer is a very complicated problem, and specific solutions only exist in certain narrow limits [26]. To get around these complicating factors, we set the charge on every monomer to unity, and to get the voltage we instead directly match the drift-diffusion balance between experiment and simulation, as outlined by de Haan et al. [10]. The balance between drift and diffusion is characterized by the dimensionless quantity known as the Péclet number

$$\mathrm{P}\acute{e} = \frac{vL}{D}, \tag{1.39}$$

where v is the characteristic velocity, L the characteristic length, and D the characteristic diffusion coefficient.

The diffusion coefficient is something that can be measured in both experiment and simulation, the characteristic velocity is set as the drift velocity of the polymer, and the characteristic length is usually taken as some representative chain contour length. The drift velocity, although easy to obtain in simulations, is not directly measured in experiments. Instead, experiments measure the mobility of the polymer, which is related to the drift velocity via

$$v_{\mathrm{drift}} = \mu \frac{\Delta V}{L}, \tag{1.40}$$

where ΔV is the voltage drop and L is the same length as above. In the simulations the mobility is simply $\mu = 1/\zeta$. In experiments, the mobility of the molecule depends on the concentration and the type of salt added to the solution.

By matching the Péclet number between simulation and experiment, we obtain an expression for the simulation voltage

$$\mathrm{P}\acute{e}_{\mathrm{exp}} = \mathrm{P}\acute{e}_{\mathrm{sim}}, \tag{1.41}$$

$$\Delta V_{\mathrm{sim}} = \Delta V_{\mathrm{sim}} \frac{\mu_{\mathrm{exp}}}{\mu_{\mathrm{sim}}} \frac{D_{\mathrm{sim}}}{D_{\mathrm{exp}}}. \tag{1.42}$$

This approach to obtaining the voltage does not account for the fact that semiflexible polymers have an energy cost for bending. As a result, the voltage obtained from this analysis gives a good order of magnitude estimate for what the simulation voltage should be, but not an exact value as it usually needs to be increased by $\approx 30\%$(or more, depending on pore size) in order to match reference experimental occurrences of folded translocations.

1.4.4.4 Mapping timescales

As we are interested in measuring translocation times, we need a way to map the times we obtain in the simulations to the ones observed in experiment. We obtain this map by equating the drift velocities for experiment and simulation

$$v_{\mathrm{exp}}[\frac{m}{s}] = v_{\mathrm{sim}}[\frac{\sigma}{\tau}], \tag{1.43}$$

where the brackets contain the units. Similarly to the voltage calculation, we can isolate for the value of one unit of time in the simulations relative to one second

$$[\tau] = \frac{\mu_{\mathrm{sim}}}{\mu_{\mathrm{exp}}} \frac{\Delta V_{\mathrm{sim}}}{\Delta V_{\mathrm{exp}}} \frac{L_{\mathrm{exp}}}{L_{\mathrm{sim}}} [\frac{\sigma}{m} s]. \tag{1.44}$$

These equations above relate simulation units to SI units. In practice, we fix the

value of σ and ζ and use these equations for obtaining values that can be compared to experiment.

1.4.4.5 Bond-Crossing

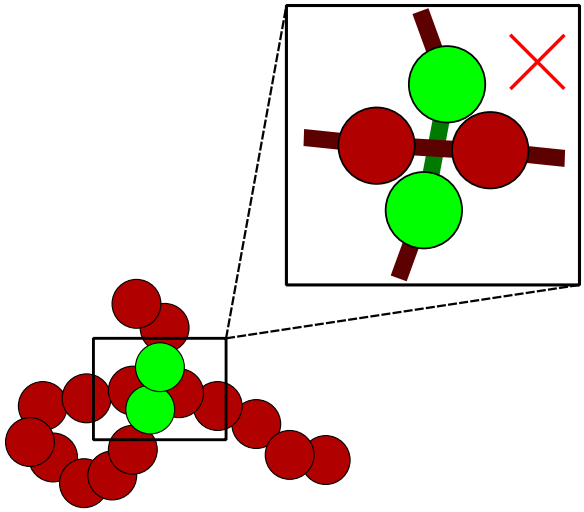

Figure 1.6: Schematic depiction of bond crossing. The green particles should not be able of cross the red bond. The dark lines red represents standard FENE bonds and dark green represent bonds that are not allowed.

The values for the constants in FENE will be chosen such that they prevent errors in the polymer topology known as bond crossing. As the name implies, bond crossing occurs when the bond connecting two monomers crosses the bond connecting two different monomers, as shown in Figure 1.6. In reality, this would never occur as bonds cannot cross one another.

If allowed to happen, bond crossing introduces a significant source of error as the polymer is able to instantaneously adopt conformations that would normally require a long time to achieve. In our nanopore systems the conformation of the polymer plays an important role as the chain interacts with the membrane, and bond crossing would allow for non-physical conformations to advance through the nanopore.

In this thesis we will use the values for FENE that were found to minimize bond

crossing by Kremer and Grest [15]. These values are $k = 30k_{\mathrm{B}}T/\sigma^2$ and $r_{\max} = 1.5\sigma$. Grest and Kremer [15] found that this spring constant did not allow for the maximum extension of the bond to be greater than $1.2\,\sigma$ at $\epsilon = 1k_{\mathrm{B}}T$[15]. Given that our simulations will be for semiflexible chains, the angle bond also assists in preventing bond crossing by rendering it even further energetically unfavourable. The net effect of combining the WCA and FENE potentials is shown in Figure 1.7. The most salient feature of Figure 1.7 is that the equilibrium bond length for pairs of monomers in the chain is ≈ 0.97.

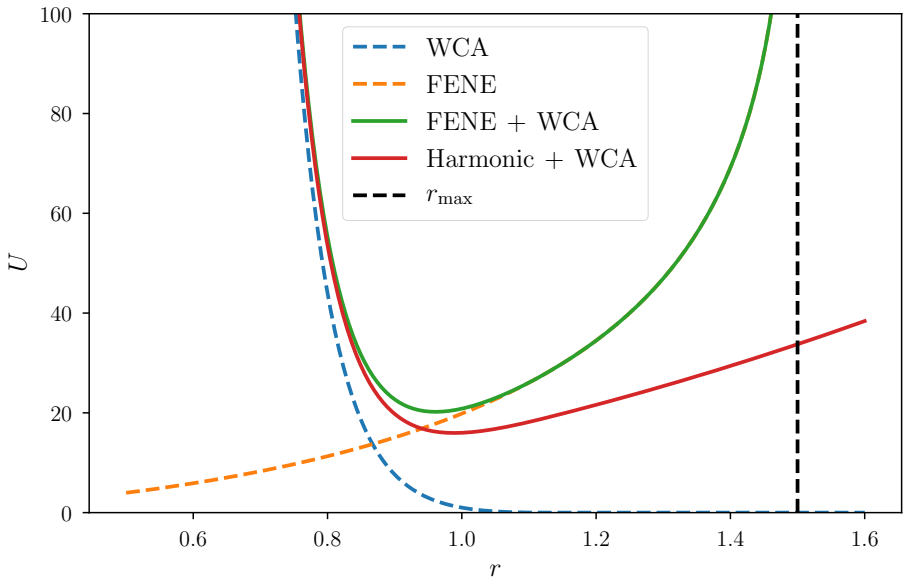

Figure 1.7: Combination of the WCA and FENE potentials at the values of Grest and Kremer [15]. The black dashed line corresponds to the maximum extension of the bond. The WCA and Harmonic spring potential is added for comparison.

1.4.4.6 Numerical Integration

The dynamics of the polymer model presented thus far are obtained by simultaneously solving the Langevin equation for all the monomers in a chain. This leads to N coupled stochastic differential equations which must be integrated numerically.

A very common numerical integration algorithm is the velocity Verlet algorithm [40]. Given initial positions and velocities, as well as a timestep Δt, the algorithm updates the states of the particles using

$$\mathbf{x}_i(t + \Delta t) = \mathbf{x}_i(t) + \mathbf{v}_i(t)\Delta t + \frac{1}{2}\mathbf{a}_i(t)\Delta t^2 \tag{1.45}$$

$$\mathbf{v}_i(t + \Delta t) = \mathbf{v}_i(t) + \frac{1}{2}[\mathbf{a}_i(t + \Delta t) + \mathbf{a}_i(t)]\Delta t \tag{1.46}$$

where $\mathbf{v}_i$ and $\mathbf{a}_i$ are the velocity and acceleration of the ith particle, and $\mathbf{r}_i$ the position. The specific version of the above algorithm used for this thesis, known as the half-step velocity Verlet, is conducted in the following steps:

1. At time t, compute the net force on each monomer,$\mathbf{F}_i(t)$, using $\mathbf{x}_i(t)$ and $\mathbf{v}_i(t)$. Compute the acceleration, $\mathbf{a}_i(t) = \mathbf{F}_i(t)/m_i$.

2. For each monomer compute the half-step velocities, $\mathbf{v}_i(t + \frac{1}{2}\Delta t) = \mathbf{v}_i(t) + \frac{1}{2}\mathbf{a}_i(t)\Delta t$.

3. Update the position of each monomer with $\mathbf{x}_i(t + \Delta t) = \mathbf{x}_i(t) + \mathbf{v}_i(t + \frac{1}{2}\Delta t)\Delta t$.

4. Recompute forces and accelerations with the updated positions.

5. Update the velocities of each monomer with $\mathbf{v}_i(t + \Delta t) = \mathbf{v}_i(t + \frac{1}{2}\Delta t) + \frac{1}{2}\mathbf{a}_i(t + \Delta t)\Delta t$.

6. Repeat.

In this thesis the HOOMD-blue [1] software package was used for the numerical integration as well as the implementation of the interactions between monomers. Although other software packages exist, the main advantage of HOOMD is that it can run entirely on GPUs, which significantly speeds up calculations.

1.4.4.7 Boundary Conditions

For the nanopore systems presented in the articles included in this thesis, the polymer interacts with a membrane containing a cylindrical hole. The membrane is modelled as a planar reflecting wall, with the interior walls of the nanopore also being reflecting.

In the HOOMD-blue software package [1], there are no pre-made nanopore geometries. As a result, the geometry had to be defined as a valid interaction at the GPU level. The nanopore was implemented using WCA potentials to define repulsive interactions with the reflecting walls that represent the pore and the membrane. These forces are calculated as if the membrane and the nanopore were made from infinitely many particles of unit size, such that there is a complete covering of their surface. The code used to generate the nanopore, as well as some additional details, can be found in Appendix C.

1.5 Literature Review

The physics of translocation through a pore has been the subject of intense research over the past few decades with hundreds of articles in experiment, simulation, and theory [27, 32]. The growth of the field has also lead to a considerable amount of research in nanopore fabrication and engineering. Current research experiments in the fields seeks to improve aspects of nanopores in order to reduce the variability inherent to the translocation process. In theory and simulation, ongoing work seeks to validate theoretical models and reproduce experimental results in order to gain insight on certain aspects of the problem that are poorly understood. In the following sections we will review some key results.

1.5.1 Experimental studies

There are several review papers [42, 27] that summarize the successes of nanopore translocation experiments as well as future prospects. As mentioned in the introduction, the first use of nanopores as DNA sequencing devices was [19] using biological nanopores. However, over the years synthetic nanopores have become the preferred method of conducting translocation experiments as they can be tuned to specific applications [27].

1.5.2 Simulation and Theoretical Studies.

The vast majority of theoretical and simulation research is done on freely jointed chains with excluded volume [32]. Although the focus of this thesis is on semiflexible polymers, it is instructive to review key ideas from the literature of freely jointed chains as there are some overlaps in concepts.

Much like experimental studies, theoretical and simulation work in the field is interested in the scaling laws of various quantities as a function of chain length. A key idea from theory is that the process of a polymer translocation through a pore can be decomposed into two stages: capture and translocation. In the capture stage, the polymer diffuses around in solution following its placement in the device. After some time the chain makes contact with the nanopore and eventually enters the pore. The translocation stage is the motion of the chain while it is inside the nanopore up until it wholly crosses the membrane.

1.5.2.1 Unbiased Translocation

Early theoretical work was done on unbiased translocation, where the polymer passively enters the nanopore to initiate translocation. Work carried out by Sung and

Park [36] in 1996, describes translocation as the result of a stochastic process and modeled the polymer as a very long ideal chain. They were able to quantify the notion of an energy barrier needed for translocation. The free energy barrier idea rested on the fact that the polymers conformation is affected by interactions with the membrane, thus leading to a reduction in its entropy. Muthukumar [25] further extended the results of Sung and Park [36] to real chains.

Both studies were analytic in nature and used the Fokker-Planck (FP) formalism[26], which uses free energy functions to analyse the dynamics. A key assumption in the FP method is that while translocation occurs the segments of the chain that are not translocating remain in equilibrium (i.e. the translocation stage is quasi-static). However, this picture is incorrect, as it implies that the translocation time is shorter than the relaxation time for long chains, which is in contradiction with the initial assumption [6].

Following these results the field saw a huge body of simulation literature attempting to find the scaling of translocation time as a function of chain length. Surprisingly, simulation studies kept finding different scaling exponents leading to a lack of consensus on the underlying physics. Work by de Haan and Slater [9] showed that the origin of the differing scaling laws was the variance in simulation conditions and were able to reconcile the apparent discrepancies in literature.

1.5.2.2 Driven Translocation

The addition of an external field driving the polymer and facilitating translocation lead to further surges in research. The external force changes the scaling of the translocation time and so a theoretical picture was highly sought after. To predict the scaling the quasi static approach was once again invoked. In contrast to unbiased translocation, where the energy barrier is rather flat, the addition of a force

tilts the energy landscape. Thus, in the quasi static picture, translocation is completely dominated by drift at large forces. Of course, since unbiased translocation was non-equilibrium, driven translocation is likely to also have non-equilibrium effects. The field again saw a surge of simulation articles trying to find the scaling of the translocation time. Once again, differing methodologies lead to wildly different scaling exponents.

1.5.2.3 Tension Propagation

The idea of tension propagation, an analytic theory proposed by Sakaue [29] and eventually refined by Ikonen et al. [18], provided resolution to the search of scaling exponents for driven translocation. The primary insight behind the theory of tension propagation is that if the chain is in an equilibrium conformation at the beginning of translocation, the effect of the external force is only felt by the parts of the chain local to the pore. The perturbation on the chain then propagates through the chain as a wave of tension with finite speed, leaving a portion of the chain at equilibrium at the onset of translocation. Using both analytic and numerical techniques, Ikonen et al. [18] finalized the theory of tension propagation, finding that the length of the chain and its interactions with the pore have a great impact on the dynamics and recovering excellent agreemnt with previous results. Furthermore, Ikonen et al. [18] demonstrated that experiments and simulations work with chain lengths that are too short to approximate the long chain regime, which is a common assumption in theoretical results.

1.5.2.4 Capture

So far we have dicussed the translocation stage but have neglected discussing the capture stage. In both unbiased and driven translocation, capture can be readily

ignored under the assumption that the polymer initiates translocation in an equilibrium conformation. For this reason, the majority of simulation studies do not include capture. However, recent simulation work has called into question the validity of the equilibrium assumption. The application of an external field would result in tension propagating along the polymer prior to reaching the nanopore. The resulting conformational changes would render the translocation dynamics far from equilibrium.

Simulation work by Farahpour et al. [13] found that, for freely jointed chains, the chain conformations are impacted by the interplay of two effects: the electrophoretic force pulling the polymer toward the pore, and the non-linear dependence of the electric field on distance. Simulating many different chain lengths, they found that these effects induce elongated conformations on the chain, resulting in different translocation dynamics. In 2016, Vollmer and de Haan [41] explicitly tested the inclusion of capture in translocation simulations for freely jointed chains. They compared translocation results for what they term as the standard [32] and capture protocols, schematically shown in Figure 1.8. Vollmer and de Haan [41] found that the inclusion of capture greatly changes confromation of the chain at the onset of translocation with the polymers adopting elongated conformations. These conformational changes result in very different scaling exponents for translocation time between the two protocols. Moreover, they found that the drift-diffusion balance also alters the dynamics. They observed that stronger forces lead to more elongated conformations, and therefore longer translocation times, changing the scaling exponents again. Vollmer and de Haan [41] conclude that it is not just the translocation stage that is not in equilibrium but the entire process. This thesis expands on this work by studying the effects of capture on the translocation dynamics of semiflexible chains.

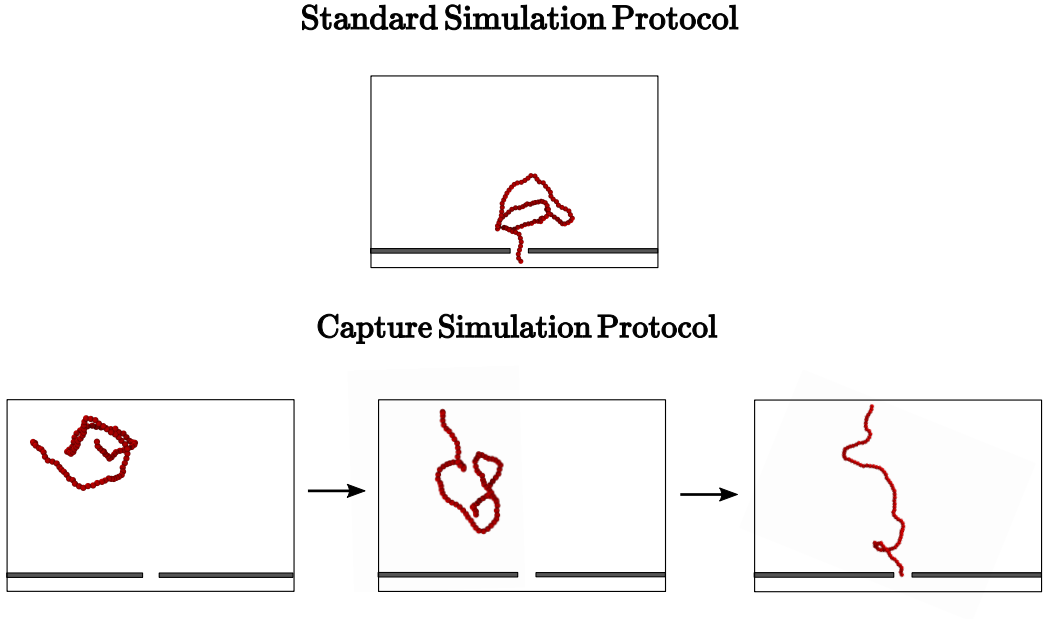

Figure 1.8: Simplified schematic overview of the two different simulation protocols for driven translocation.

1.5.2.5 Semiflexible chains

Most of the experimental literature for nanopore translocation uses double stranded DNA. As discussed before, due its high rigidity, dsDNA is best described by the wormlike chain model. The wormlike chain model incorporates the rigidity of the molecule as directional correlations between monomers resulting in a semiflexible chain. Although the freely jointed chain has been the subject of a very large amount of research, the same is not true for semiflexible chains. There are two primary reasons for this. The first is that a lot of experiments use very long double stranded DNA ($\lambda - DNA$) which is well approximated by a freely jointed chain. The second reason is that the directional correlations make the theoretical treatment of the translocation of semiflexible chains much harder to carry out, resulting in difficulty interpreting results.

The earliest study of semiflexible chains in the context of nanopore translocation was by Bhattacharya [3] in 2012, where they explored the mean first passage times of the monomers of the chain in two dimensions using simulations. Bhattacharya [3] found that in two dimensions, the theory of tension propagation does not account for the dynamics of semiflexible chains. However, certain aspects of the theory (such as the tension wave) are still present. In 2017, Sarabadani et al. [30] were able to modify the equations of tension propagation to describe the dynamics of the chain as it is being pulled through the nanopore in the standard protocol. Their modification allowed them to recover the scaling regimes for the power law behaviour of the translocation time for constant persistence length. They showed that their predicted values for the scaling exponent provide good agreement with experiments.

In 2018, Suhonen and Linna [35] studied the effect of rigidity on the dynamics of driven semiflexible translocation using simulations. They found that the translocation time increases as the persistence length increases. They found that the polymer segment on the *trans* side of the pore has a large effect on the dynamics as when it buckles the friction felt by that part of the chain is reduced. This is an effect that does not occur in the freely jointed chain, where the behaviour of the chain segment in the *cis* side dominates the dynamics. Furthermore, they showed that in the limit of long chains the freely jointed behaviour is recovered. Recent work by Wu et al. [43] in 2019 explored the non-equilibrium nature of semiflexible chain translocation. Using simulations with the standard protocol they showed that, at all persistence lengths, semiflexible chains are not in equilibrium during translocation. They found that at very high persistence lengths, the non-equilibrium effects on translocation diminish. They identified the criterion for this transition in the dynamics to be the radius of gyration being smaller than the persistence length of the chain. They attribute the transition to the increased viscous drag experienced by the monomers in stiffer chains

due the increased strength in the correlations. Their results on the scaling of the translocation time with increasing persistence length were similar to the findings of Suhonen and Linna [35].

1.6 Presentation of the thesis

The goal of this thesis is to contribute to our understanding of the nanopore translocation dynamics of semiflexible polymers. As we've been seeing, the translocation of polymers through nanopores is a complex problem with many avenues to explore, as there are a variety of factors that may affect the dynamics of the chain. The articles presented in this thesis (Chapters 2 - 4) were either published or submitted to peer-reviewed journals during the course of my degree. The list below summarizes the main findings of each article.

Chapter 2 K. Kastritis, M. Magill, H. W. de Haan. *Diffusion-Limited Dynamics of Semiflexible Polymer Translocation with Capture* ***To be Submitted***

As mentioned in previous sections, current literature indicates that the capture process is certain to have an effect on the translocation dynamics. However, simulations with the capture process included are few as it can be computationally expensive (especially at low voltage). In addition, the standard simulation protocol for polymer translocation, the quasi-static picture, is very successful and can faithfully provide insight on certain phenomena. As such, capture is often omitted from simulations studies under the assumption that the polymer is already threaded into the nanopore. Various articles [16, 13, 41] show that for driven translocation of the freely jointed chain, capture can introduce non-equilibrium conformations. However, little work is done on the effects of the capture process on semiflexible chain dynamics

The goal of the work presented in chapter 2 is to study in detail how the process of capture by a nanopore affects the dynamics of translocation for semiflexible polymers. We model the polymer using a the wormlike chain model, and standard coarse-grained Langevin dynamics [32] along with an analytic expression for the electric field Farahpour et al. [13]. We use nine different pore radii and three different persistence lengths and observe great variability in the translocation dynamics. Restricting our attention to three limits of pore sizes (small, medium, large) for the manuscript, we explore the origin of the variability and classify the types of events observed in our translocation time distributions. We find the presence of non-equilibrium conformations due to the electric field to be responsible for the variation with pore width, primarily by stretching the chain as it moves toward the nanopore. Counter-intuitively, these non-equilibrium conformations dominate the conformation space as the pore size increase, whereas one would normally expect folded conformations to do so due to the ease of overcoming the bending energy needed to fold through the pore. Moreover, we find that the primary effect of varying the persistence length is determining at what pore size folded conformations start being possible. In addition, we find that our classification is robust across persistence lengths. The results we obtain highlight the importance of the capture process for semiflexible chains and further, the non-equilibrium nature of nanopore translocation.

Chapter 3 Kyle Briggs, Gregory R. Madejski, Martin Magill, Konstantinos Kastritis, Hendrick W. de Haan, James L. McGrath, Vincent Tabard-Cossa *DNA Translocations through Nanopores under Nanoscale Preconfinement* **ACS Nano Letters 18 (2017), no. 2, 660-668.**

Chapter 3 is the first article in our collaboration with the Tabard-Cossa lab at

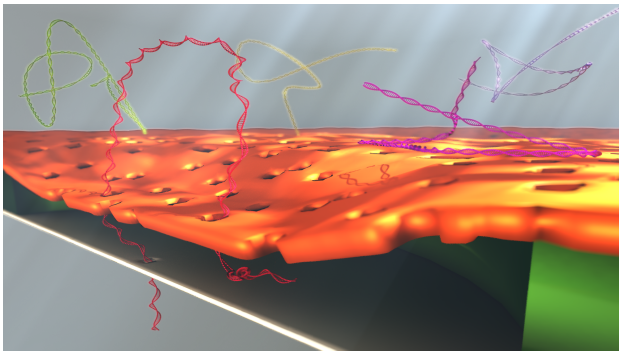

Figure 1.9: 3D render of the nanofiltered nanopore device in operation for standard translocation experiments.

the University of Ottawa [5]. In this work we used our models for semiflexible polymer translocation to gain insight on the dynamics of DNA in a nanofiltered nanopore device. Unlike standard nanopores where a single membrane with a nanoscopic hole separate two chambers, the nanofilered nanopore devices introduces a nanoporous filter in series with a standard nanopore, separated by a spacer which serves as a cavity for the polymers to enter, as shown in Figure 1.9. The design of the device, as well as the materials used for the nanofilter, prevent direct measurements across the filter. Thus, current traces may only be obtained at the standard pore, aptly called the sensing pore. Due to this limited experimental resolution, we use simulations to gain insight on the physics of DNA moving through the device. As in the previously described article, we use the wormlike chain model with Langevin dynamics. For the electric field in this device we use finite element methods to solve Laplaces equation and obtain a numerical solution on a mesh.

Consistent with the experimental results, we find a minimum in the coefficient of variation for the translocation time, indicating that the presence of the filter eliminates the dependence of the translocation time distributions on pore size. Through simulations we discover that the nanofilter induces a transition in the

dynamics by virtue of preconfinement. For chains with contour length much smaller than the height of the cavity, the filter is mostly negligible as they behave like rods and freely diffuse in the system. As the contour length of the chain becomes larger than the height of the cavity, part of the chain can still be in the filter at the onset of translocation through the sensing pore resulting in longer translocation times due the increased drag. For chains with contour length between the two regimes, the filter only stretches the polymer thus allowing for significantly reduced variation in the translocation times and therefore providing an explanation for the origin of the minimum in the coefficient of variation.

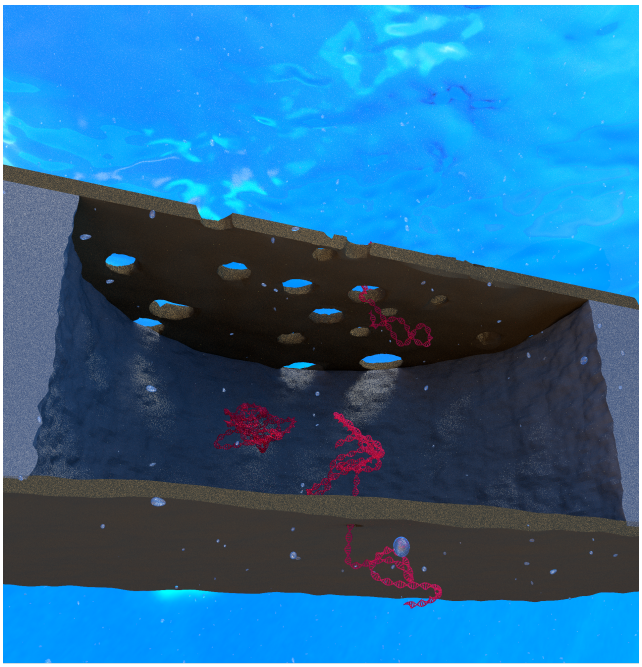

Figure 1.10: 3D render of the nanofiltered nanopore device in operation as an entropic cage for dsDNA.

Chapter 4 Michelle H. Lam, Kyle Briggs, Konstantinos Kastritis, Martin Magill, Gregory R. Madejski, James L. McGrath, Hendrick W. de Haan, Vincent Tabard-Cossa *Entropic Trapping of DNA with a Nanofiltered Nanopore* **Accepted for publication in ACS Applied Nano Materials**

Chapter 4 presents our second article in collaboration with the Tabard-Cossa lab. This time we investigate the viability of a modified nanofiltered nanopore device as an entropic cage for DNA. In contrast to the article in Chapter 3, the device here has a larger cavity and smaller filter pores. This design allows for experimentation with larger molecules. The device has two modes of operation: diffusive trapping and driven trapping. Our simulation work focuses on the diffusive trapping mode. In this mode, the molecules were loaded into the device from the sensing pore. Once loading was complete, the voltage was turned off for up to 30 seconds. During that time the DNA would either escape or remain in the cavity. Unexpectedly, while long DNA strands (7 kbp) remained trapped for the times tested, the shortest DNA strand (1.2 kbp) exhibited leakage through the filter. To investigate this phenomenon we perform simulations of the device.

Conducting many-body simulations for 30 seconds of real time is challenging to do directly. Instead, we use an effective multiscale approach. We decompose the motion of the polymer into two regimes; one close to the filter pore and one in the bulk of the cavity. As the internal degrees of freedom of the chain become important near the nanofilter we use the wormlike chain model and coarse-grained Langevin dynamics to obtain the probability of a polymer performing unbiased translocation through the mebrane before diffusing away from the nanofilter. In the bulk of the cavity we model the DNA molecules as single particles representing their center of mass with their motion given by Brownian dynamics. We couple the two simulations by a special boundary condition on

the Brownian dynamics side of the simulations.

From the simulations, and TEM image analysis, we find that the escape dynamics in the device are governed by a population of large, merged pores on the nanofilter. Moreover, we find that small pores offer a negligible contribution to the escape rate as only a handful of merged pores are needed for the simulations to have good agreement with the experimental results. The presence of these merged pores is a consequence of the manufacturing process for the nanofilter, indicating that it can be tuned to be advantageous for the desired application.

Chapter 2

Dynamics of Semiflexible Polymer Translocation with Capture

Diffusion-Limited Dynamics of Semiflexible Polymer Translocation with Capture

Konstantinos Kastritis,[1] Martin Magill,[1] and Hendrick W. de Haan[1,*]

[1] *University of Ontario Institute of Technology*
Faculty of Science

(Dated: August 29, 2019)

I. ABSTRACT

The passage of double stranded DNA through solid-state nanopores is an ever growing field in biophysics research, with many promising technological applications. However, the physics of semi-rigid molecules undergoing nanopore translocation is not very well understood. In this work we use Molecular Dynamics to look at the effect of the capture process on the translocation dynamics of semiflexible polymers. We examine the distributions of the translocation time and how they vary as a function of pore radius. In particular, we explore how changing the pore radius, in addition to the inclusion of capture, results in non-equilibrium conformations at the onset of translocation. We classify the resulting conformations and observe that non-equilibrium conformations dominate as the radius of the pore increases.

II. INTRODUCTION

Nanopores have been the subject of intense study for nearly twenty years due to their promising biomedical applications [1]. The seminal work carried out by Kasianowicz *et al.* [2] showed that DNA could be driven through a biological nanopore and paved the way for controlled molecular transport across membranes. The experimental concepts of translocation for single molecule manipulation were then extended to solid-state artificial nanopores [3] that could be applied to various problems, with DNA sequencing being the most notable [4].

Nanopore translocation has also been the subject of a significant amount of theoretical and numerical work [5]. Concepts from polymer physics allow for the description of complicated macromolecules with mechanical models of beads connected by springs. Simulations of these idealized polymers in nanopore systems yield insights on the physics of the entire process of molecule translocating though a nanopore.

A significant amount of research in both experiments and simulation is conducted with driven translocation [6], using electric fields to drive the molecule towards the nanopore. Recent work [7, 8] has shown that the process via which the polymer approaches the nanopore, called capture, plays an important role in the translocation dynamics. Vollmer and de Haan [7] introduce a delineation between what they term as the standard simulation protocol and the capture simulation protocol. The standard simulation protocol is one where the polymer is assumed to be in quasi-static equilibrium prior to initiating translocation and is therefore initialised with part of the chain already in the nanopore and the rest of the chain in equilibrium [5, 6]. In contrast, the capture simulation protocol posits that the polymer is only in equilibrium far from the pore and the interaction with the electric field can lead to non-equilibrium effects. For this reason the polymer is initialized far away from the membrane and the process of the electric field pulling the polymer toward the pore is simulated.

Until recently, most of the theoretical and simulation work in the field was performed on the freely jointed chain. The freely jointed model has been a strong basis for theoretical work, resulting in its dynamics under driven translocation being fully characterised by the theory of tension propagation [9–11]. The freely jointed chain is a very successful model in describing molecules that have low rigidity or are very long. However, in experiments, semiflexible polymers such as double stranded DNA are of primary interest. A remarkable property of double stranded DNA is its high rigidity compared to most other polymers, which is due to its famous double helix configuration. As such, a description of the dynamics of semiflexible chains is of great interest.

The wormlike chain model [12] is a way of introducing rigidity into the freely jointed chain via directional correlations along the backbone of the polymer. These directional correlations result in segments of the chain acting as rods whose stiffness decays as a function of distance along the polymer. This correlation length is called the persistence length, ℓ_p, of the chain and is intimately related to the bending energy of the chain. This additional constraint makes the polymer semiflexible.

One of the earliest studies on the driven translocation of semiflexible polymers was in two dimensions by Bhattacharya [13]. They explored the mean first passage time of the monomers and the scaling exponent for the translocation time as a power law in polymer length. They found that the freely jointed tension propagation theory can still describe certain aspects of semiflexible chains.

More recently, work by Sarabadani *et al.* [14] explored the universal scaling exponents of semiflexible chains in three dimensions and provided a modified tension propagation model for the dynamics of the process. Work by Suhonen and Linna [15] further investigated the effect of rigidity on the process by varying the friction felt by the monomers in addition to varying the driving force. They

* Hendrick.deHaan@uoit.ca

found that the overall scaling of the parameters changes significantly from the freely jointed version. Work by Wu *et al.* [16], showed the effect of rigidity on the scaling behaviour of the translocation time. They found that, in the standard protocol, although semiflexible polymers are not in equilibrium during translocation, they experience weaker non-equilibrium effects at very large persistence lengths, with their radius of gyration being close to the equilibrium value.

Semiflexible chains were also used in simulations of proof-of-concept sorting by micro-channel nanopores in work by Magill *et al.* [17]. There, capture was included but the details of the process and its effect on the dynamics were not explored.

In previous work conducted by the authors [18], semiflexible chains were used to simulate a more faithful DNA model to the experimental setup of a nanofiltered nanopore device. A transition was found from the rodlike limit to semiflexibility that minimizes the variation in translocation times. Interestingly, the transition was present, although more subtle, even when the nanofilter was not in the device (i.e. when it was just a nanopore).

In this manuscript, we present simulations of the dynamics of the capture and translocation of semiflexible polymers. We explored in detail how variations in pore width affect the conformations of the chains at all stages of the translocation process. Further, we investigated the effect of rigidity on the conformations available to chain at the onset of translocation, and how these affect the subsequent dynamics.

III. METHODOLOGY

Simulations were conducted using standard coarse-grained Langevin dynamics (LD) [6] with a wormlike chain model composed of N spherical monomers. The drag experienced by the monomers is given by Stoke's law. The thermal fluctuations due to solvent interactions are implicitly modelled with a noise term added to the equation of motion

$$m\ddot{\vec{x}} = -\sum_i \nabla U_i(\vec{x}) - \zeta\dot{\vec{x}} + \sqrt{2\zeta k_{\mathrm{B}}T}\vec{\xi}(t), \qquad (1)$$

where ζ is the drag coefficient and $k_{\mathrm{B}}T$ is the thermal energy. The gradient term encodes all other forces in the system. The fluctuation term $\vec{\xi}(t)$ is a noise function that satisfies

$$\langle\vec{\xi}(t)\rangle = 0, \qquad (2)$$

$$\langle\xi_i(t)\xi_j(t')\rangle = \delta_{ij}\delta(t-t'). \qquad (3)$$

The velocity Verlet algorithm was used to evolve the system in time, using the numerical implementation found in the HOOMD-blue molecular dynamics software package for the Python language [19, 20].

The bonds between adjacent pairs of particles were modelled using the finitely extensible nonlinear elastic (FENE) potential

$$U_{\mathrm{FENE}}(r) = -\frac{1}{2}kr_{\mathrm{max}}^2 \ln\left(1 - \frac{r^2}{r_{\mathrm{max}}^2}\right), \qquad (4)$$

where the constants k and r_{max} represent the stiffness and the maximum possible extension of the bond, respectively. The repulsive interaction between monomers was modelled using the Weeks-Chandler-Andersen (WCA) potential

$$U_{\mathrm{WCA}}(r) = \begin{cases} 4\epsilon\left[\left(\frac{\sigma}{r}\right)^{12} - \left(\frac{\sigma}{r}\right)^{6}\right] + \epsilon & r < r_c \\ 0 & r \geq r_c \end{cases}, \qquad (5)$$

where ϵ is the interaction strength, σ the monomer diameter and $r_c = 2^{1/6}\sigma$ the cut-off distance. Chain stiffness was modelled by a three-body harmonic potential

$$U_{\mathrm{angle}}(\theta) = \frac{1}{2}k_{\mathrm{angle}}(\theta)^2, \qquad (6)$$

where the angle θ is the angle formed by any three consecutive monomers along the chain.

All units in the simulations were derived from a self-consistent set of units with length, mass, and energy as fundamental. The units of mass and length were taken to be the diameter (σ) and mass (m) of a monomer. The unit of energy was chosen to be the thermal energy, $k_{\mathrm{B}}T$. Within this system of units, time is measured by $t_{\mathrm{sim}} = \sigma\sqrt{m/k_{\mathrm{B}}T}$. The value of σ in the simulations was set to unity with its equivalent value in real units chosen to be 5nm. The drag coefficient, ζ, was also set to unity.

The persistence length of the polymer is $\ell_{\mathrm{p}} \approx \frac{k_{\mathrm{angle}}}{k_{\mathrm{B}}T}\sigma$ [21]. The persistence length of the chain was set to $\ell_{\mathrm{p}} = 10\,\sigma$ unless otherwise noted. In our choice of parameters the persistence length of double stranded DNA (≈ 50 nm) corresponds to $10\,\sigma$. The parameters of the FENE bond were set to $k = 30k_{\mathrm{B}}T/\sigma^2$ and $r_{\mathrm{max}} = 1.5\sigma$ in order to minimize bond crossing [22].

The geometry for a pore in a membrane is a custom implementation in HOOMD-blue. WCA forces were used to define the repulsive monomer-membrane interaction. For these calculations the radial distance was computed from the center of the spherical monomer to the nearest point in the membrane. Due to the nature of the excluded volume interaction with the membrane the effective radius of the nanopore was defined as $r_{\mathrm{eff}} = r_{\mathrm{nominal}} - \frac{\sigma}{2}$. The effective thickness of the membrane was defined as $t_{\mathrm{eff}} = t_{\mathrm{nominal}} + \sigma$.

A total of two thousand translocation events were collected for each simulation conducted. The metrics presented in this work were obtained for a range of effective pore radii ($0.60\,\sigma \leq r_{\mathrm{p}} \leq 4.5\,\sigma$) and for three different persistence lengths ($\ell_{\mathrm{p}} = 1\,\sigma$, $10\,\sigma$, $20\,\sigma$). The pore thickness was fixed to $t_{\mathrm{eff}} = 1\,\sigma$. The length of the polymer was fixed at $N = 100\,\sigma$ across all simulations.

A. Electric field model

To model the effect of the applied voltage across the membrane, we used the method developed by Kowalczyk *et al.* [23]. In particular, we use the same implementation of this method as Farahpour *et al.* [8] used to examine chain elongation. In this approach, the nanopore is approximated by a one sheeted hyperboloid in oblate spheroidal coordinates. The corresponding potential for the electric field through such a pore is obtained by solving Laplace's equation yielding

$$\Phi(\mu, \nu, \phi) = \frac{V_0}{\pi} \arctan(\sinh(\mu)), \tag{7}$$

where V_0 is the fixed voltage drop across the system.

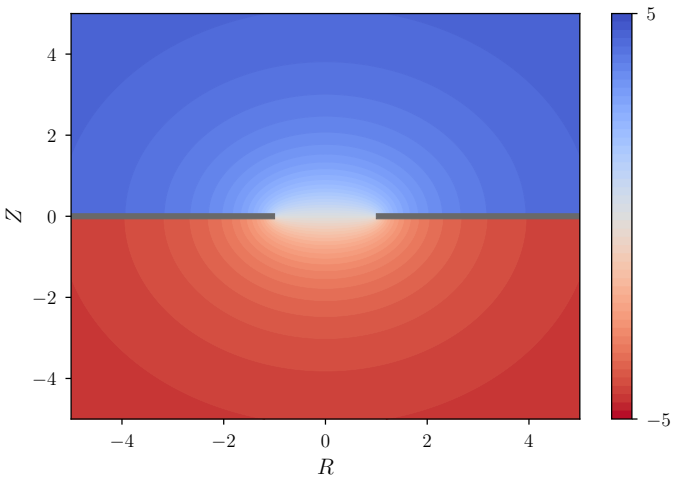

FIG. 1. View of the potential in a cross-section of the pore geometry. The color corresponds to the values of Φ as obtained from Equation 7 transformed into cylindrical coordinates, where R is radius from the center of the pore and Z the height from the center of the pore. For this image, the radius of the pore was set to $r_\mathrm{p} = 1$, and the applied voltage was $V_0 = 10$.

As shown in Figure 1, this potential models the electric field through a small aperture in a membrane when the effective thickness is vanishingly small. The density of equipotential lines show intensity. The field becomes very strong inside the pore and the potential decays as a r^{-1} relative to the pore.

B. Deformation Radius

To model the capture process, we initialise the polymers at a sufficient distance from the pore that the electric field would not significantly deform their conformations from equilibrium. The equilibrium average radius of gyration for a semiflexible chain is given by

$$\langle R_\mathrm{g}^2 \rangle_\mathrm{SF} = \frac{1}{3} L_\mathrm{c} \ell_\mathrm{p} - \ell_\mathrm{p}^2 + 2\frac{\ell_\mathrm{p}^3}{L_\mathrm{c}} - 2\frac{\ell_\mathrm{p}^4}{L_\mathrm{c}^2}\left[1 - e^{\left(-L_\mathrm{c}/\ell_\mathrm{p}\right)}\right], \tag{8}$$

where L_c is the contour length of the chain Doi and Edwards [12]. To determine the initialisation distance, simulations were conducted with the polymer $150\,\sigma$ from the mouth of the nanopore. Recall that the polymer length used here is $100\,\sigma$. The deformation of the chain is measured as it evolves in time under the influence of the field. The simulation is terminated when a single monomer reaches the nanopore.

We measured the deformation of the chain via the component of its gyration tensor directed from the pore to its center of mass. We call this radial radius of gyration. For these simulations, the middle monomer is fixed to only move in the central axis of the nanopore with the rest of the chain behaving as normal. Figure 2 shows the radial radius of gyration as a function of the distance from the radially closest monomer in the chain to the mouth of the pore, r_min.

As shown in Figure 2, the mean radial radius of gyration increases significantly beyond fluctuations from the equilibrium value as the polymer approaches the nanopore, indicative of the chain becoming stretched due to the electric field. Additionally, Figure 2 suggests that when the chain is placed $150\,\sigma$ from the pore, there is a selection bias and chains with low $R_\mathrm{g}^\mathrm{radial}$ at placement diffuse further away and remain coiled relative to the nanopore, as the effects of the electric field diminish.

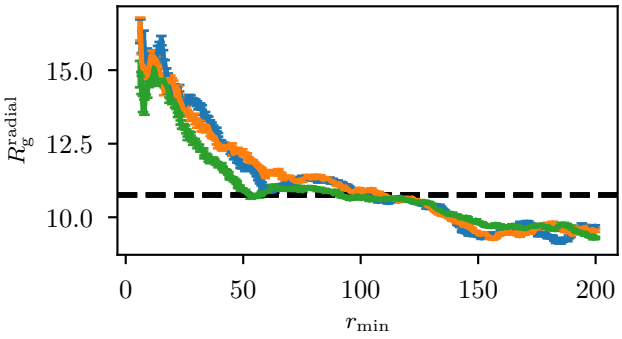

FIG. 2. $R_\mathrm{g}^\mathrm{radial}$ binned by the radial distance r_min of the monomer closest to the nanopore. The black dashed line represents one third of the radius of gyration of the worm like chain calculated with Equation 8 which corresponds to being at an equilibrium conformation in the direction radial to the pore.

C. Equilibration

In a separate simulation, with no electric field or nanopore present, the chain was equilibrated with its middle monomer fixed in space while the remaining monomers are allowed to diffuse. The polymer is allowed to equilibrate for $t_\mathrm{eql} = 10(N\ell_\mathrm{p})^2$ at a reduced friction coeffient, $\zeta^* = 0.1\zeta$. A database of ten thousand equilibrium conformations with which to initialise the polymer

was generated.

D. Simulation Procedure

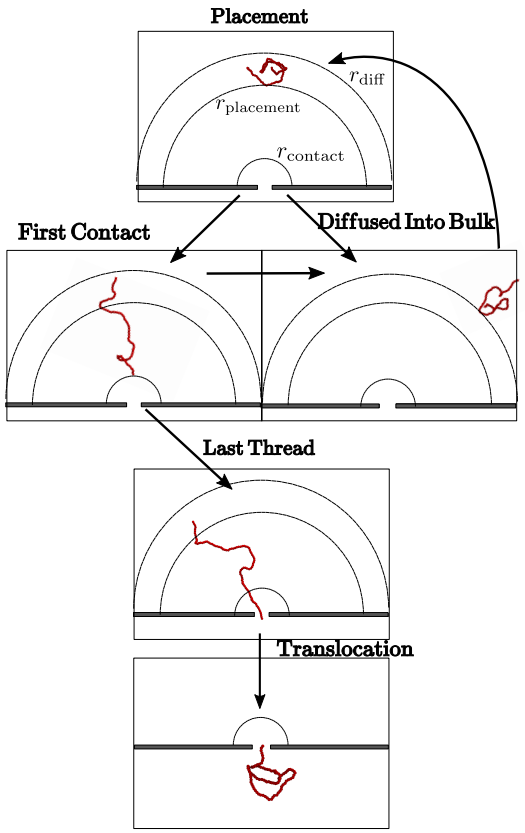

FIG. 3. Schematic detailing the protocol used to conduct the simulations. The polymer begins in an equilibrated conformation with the monomer closest to the pore at $r_{\text{placement}}$. If the entire chain is further than r_{diffused} away from the mouth of the nanopore, the event is terminated and restarted with a new equilibrium conformation. A polymers first contact with the nanopore is designated by any monomer being within r_{contact}. First/Last thread occur when any part of the chain enters the trans side of the membrane.

The procedure used to conduct the simulations is illustrated in Figure 3. Each stage is described below.

Placement: At the beginning of the simulation a random equilibrium conformation is chosen from the database. The monomer radially closest to the nanopore is placed on a hemisphere of radius $r_{\text{placement}}$ centered at the pore with the rest of the chain translated accordingly. Following placement, the system is evolved via LD with the electric field present. The placement radius, $r_{\text{placement}}$, for a chain is defined as the last intersection of the curves in Figure 2 with the equilibrium value.

Diffused Into Bulk: Should at any time the entire chain diffuse too far away from the pore, the event is considered a failure, and the chain is re-initialized by picking another equilibrium conformation. The cutoff radius for this was chosen to be $r_{\text{diffused}} = r_{\text{placement}} + 3\sqrt{\langle R_{\text{g}}^2 \rangle_{\text{SF}}}$.

Contact: The chain is determined to have made contact with the nanopore if any monomer is within the contact radius. The contact radius was that of a hemisphere centered around the mouth of the nanopore. The numerical value chosen was $r_{\text{contact}} = 6\,\sigma$ and was kept constant across pore sizes. See Appendix A for more details.

First/Last Thread: Prior to beginning the translocation process, the polymer can partially thread into the pore but subsequently retract to the *cis* chamber without translocating. The first such attempt at threading made by the chain is defined as first thread and the last successful attempt is defined as the last thread. Note that first thread and last thread can be the same event if there are no retractions to the *cis* side of the membrane.

Post-Translocation: After the last monomer has successfully moved to the *trans* side of the membrane, the event is termed successful and the simulation for that polymer terminates.

At all stages listed above the components of the radius of gyration were recorded. For every successful event we obtained the translocation time, the time of first contact and the times of first and last thread, with the translocation time computed from the time of last thread. In addition, the indices of the monomers that initiated contact, first thread, and last thread were recorded.

The thread and contact monomers indices were used to define the normalized thread and contact locations along the chain, respectively. Following a procedure similar to [24], we sought to compute a normalized location along the chain by decomposing it in a short arm and a long arm. Because the chain is symmetric, one arm is always closer to an end. However, in contrast to their work, where charge deficits had to be used to infer the decomposition, we directly use the monomer indices to determine the length of the short (l_{short}) and the long arm (l_{long}). Taking the length of each arm, the normalized location along the chain was given by

$$s = \frac{l_{\text{short}}}{L_{\text{c}}}. \tag{9}$$

For the two smallest pores ($0.60\,\sigma$, $1.1\,\sigma$) some filtering of the data was necessary due to polymers diffusing far from the pore even after contact, more details can be found in Appendix A.

IV. RESULTS

A. Translocation Dynamics

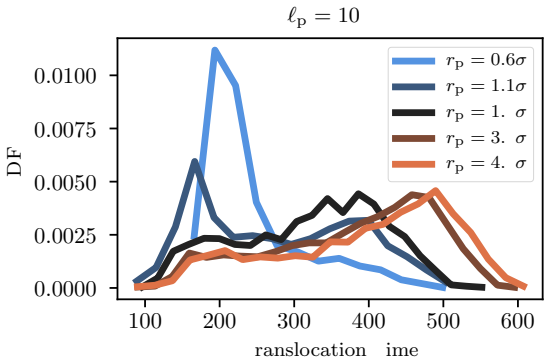

FIG. 4. Distributions of translocation times through the nanopore for various pore radii at $\ell_p = 10$.

Figure 4 shows the distributions of translocation time at various pore radii. At $r_p = 0.6\,\sigma$, the smallest pore examined, the distribution is unimodal with a long tail. As pore radius increases, a transition from long-tailed unimodal distribution to bimodal distributions can be seen.

In this section we will be examining simulations with three representative pore sizes (with numerical values corresponding to the limits of small, medium, and large) to classify the events that generate the behaviour observed in Figure 4. We will show that the peaks actually best described by four subpopulations some of which were given names.

Figure 6 shows several quantities as functions of translocation time in all three cases. The first row shows the distributions of translocation times for these pore sizes. The second row shows which part of the chain first contacted the nanopore. The third row shows the time a polymer takes to go from first contact to last thread. The fourth row shows the part of the chain that last attempted to initiate translocation. The last row shows the radial radius of gyration of the polymer at the time of last thread.

We first examine the behaviour of the polymers in the small pore at $r_p = 0.6\,\sigma$. Because of the small pore radius, all events threaded by an end (Figure 6b) regardless of the monomer that initiated first contact(Figure 6d). The waiting time (Figure 6c) paints an interesting picture - fast translocation events wait longer between contact and last thread while slow translocation events wait for a much shorter amount of time. This trend is suggestive of the polymer having drastically different conformations at the onset of translocation between the two types of events, as we know that stretched chains take longer to translocate. Indeed, looking at Figure 6e we see that events with long translocation times and short waiting times have significantly larger radial radius of gyration at the onset of translocation (i.e. at last thread), indicating stretched conformations. In contrast, events with fast translocation time have increasingly longer waiting times. In these waiting times the polymers become compressed against the nanopore, as evidenced by the radial radius of gyration in Figure 6e. Thus, we can readily identify two types of events. We classified events with long waiting times and fast translocations as "slow thread – fast translocation" events. Consequently, events that exhibit short waiting times and slow translocation were classified as "fast thread – slow translocation" events.

Next, we look at a medium pore with $r_p = 1.1\,\sigma$. Similar to the case of a small pore the waiting time readily allows us to identify the two broad types of events defined previously (slow thread – fast translocation, fast thread – slow translocation). Immediately, we can see that the relative fraction of fast thread – slow translocation events has increased dramatically compared to the small pore. However, unlike the small pore, the medium pore is large enough to allow folded translocation (Figure 6c). Nevertheless, the folded events behave like the slow thread – fast translocation events. For this reason, we classified these folded events as "folded slow thread – fast translocation".

Last, we explore the large pore limit with $r_p = 3.5\,\sigma$. Rather surprisingly, the waiting time no longer delineates different types of events, as it remains constant and small at all translocation times. Indeed, looking at Figure 6e, the radial radius of gyration distribution, it can be seen that there were no states where the polymers were compressed against the pore membrane. Further, the contact and thread locations are now significantly correlated at all translocation times, indicating that the polymers maintain their conformations from first contact. Together, these observations indicate that polymers are successfully translocaing on their first attempts with little delay. Fast thread – slow translocation events are still present as recognized by their long translocation times and elongated conformations, but slow thread – fast translocation events identified in the case of the small pore are no longer present in the large pore limit. At this large pore, folded events are different than before. They now have a distinct behaviour characterized by fast translocations and short waiting times. We classified these events as "fast thread – fast translocation". At this pore size we also see rare events with triple monomer occupancy in the pore at the onset of translocation (green lines in Figure 6), as shown in Figure 5. These events make analysis more complicated at large pores as additional conformations can emerge.

The fast thread – slow translocation events with R_g^{radial} close to the equilibrium value in Figure 6o are the result of chains in conformations where both ends experience similar forces dragging them towards the pore. Given that at larger pores the electric field extends further and polymers retain their conformation at first contact during last thread, these conformations have a smaller R_g^{radial}.

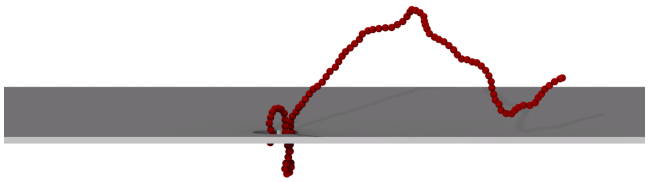

FIG. 5. Snapshot of a triple occupancy event from the simulations. These events have fast translocation times as a large part of the chain gets pulled through the pore at once.

Rather counterintuitively, fast thread – slow translocation events dominate the translocation time distributions, when one might expect fast-fast events to be more prominent, as it is easier to overcome the bending energy at larger pores. We attribute this phenomenon to the presence of the electric field. As the pore size increases, the electric field extends farther and stretches chains during capture, meaning that the monomer initiating first contact is physically close to the monomer initiating last thread.

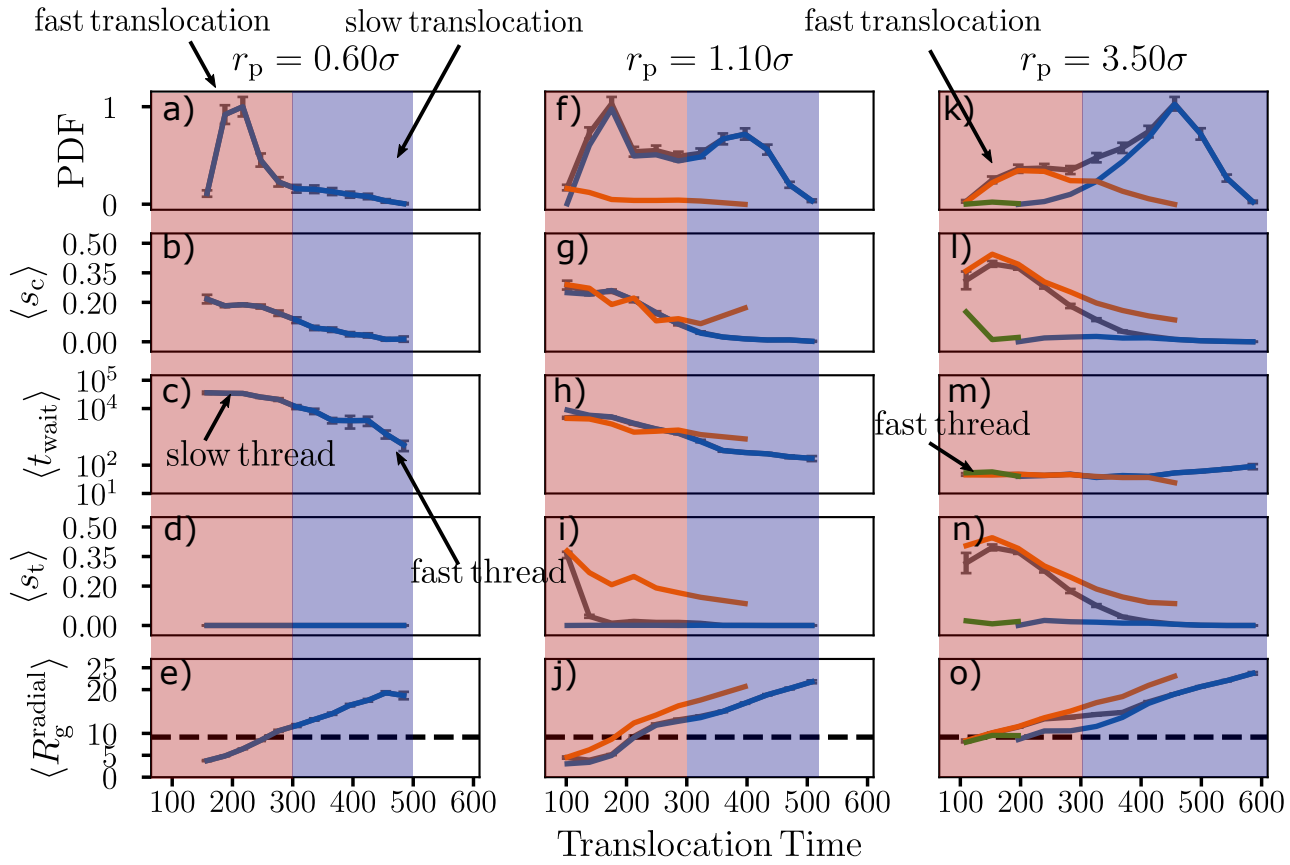

FIG. 6. Metrics as a function of translocation time for the successful events in three different pore sizes. a) The distribution of translocation times, b) the contact location,s_c, along the chain, c) the time a chain waited between first contact and last thread, d) the thread location, s_t, along the chain, e) the radial radius of gyration,R_g^{radial}, at the moment of last thread. The colored lines represent the different classes of events present in the distributions. Grey is the average over all events, blue is only the single file events, orange is the folded events, and green is events that exhibited triple occupancy in the pore at the onset of translocation. The shaded regions delineate between fast translocations and slow translocations. The red shading corresponds to short translocation times and the blue to long translocation times.

The electric field also plays a role in unwrapping polymers in asymmetrically folded conformations as they approach the nanopore. This counterintuitive effect occurs due to the smaller arm of the fold experiencing less drag than the longer arm, which has to pull the remainder of the chain along. We characterized the magnitude of this effect by looking at the fraction of events that contacted the nanopore near the ends of the chain as a function of

pore radius, as shown in Figure 7. Consistent with our classification of events, Figure 7 shows that as the pore size increases so does the fraction of polymers that contact the nanopore close to a free end ($s_c <= 0.1$). This is suggestive of the polymers adopting non-equilibrium conformations. Specifically, the chains are stretched prior to translocating and remain stretched during translocation.

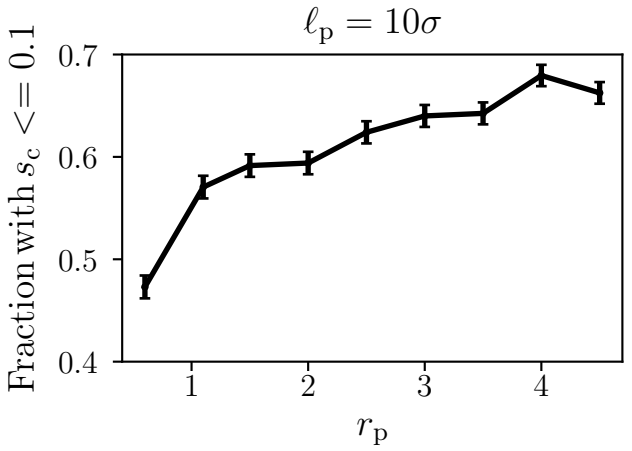

FIG. 7. Percent of contact locations with a value close to the ends of the chain ($s_c \leq 0.1$) as a function of pore radius.

B. The Effect of Persistence Length

In addition to varying the pore size, we explored different persistence lengths. The classification of events in the section above remained applicable for the two additional persistence lengths studied ($\ell_p = 1\,\sigma, 20\,\sigma$). Figure 8 shows the percent folding fraction as a function of pore radius for all three persistence lengths studied.

The most salient feature of Figure 8 is that folded conformations emerge at different pore sizes for different persistence lengths. For stiffer polymers ($\ell_p = 20\,\sigma$) than those examined in the previous section ($\ell_p = 10\,\sigma$), the threshold pore size for folding to occur has increased. Conversely, for less stiff chains, the threshold pore size has decreased when compared to the previous section. This is a direct consequence of the bending energy being a function of persistence length, making it significantly harder for folded conformations to occur below at certain pore sizes. Moreover, as persistence length increases the total fraction of folded events decreases, which we attribute to non-equilibrium conformations becoming more prominent at larger pores in addition to folding becoming more difficult.

V. CONCLUSIONS

In this work we explored the capture and translocation dynamics of semiflexible chains. We showe that increases

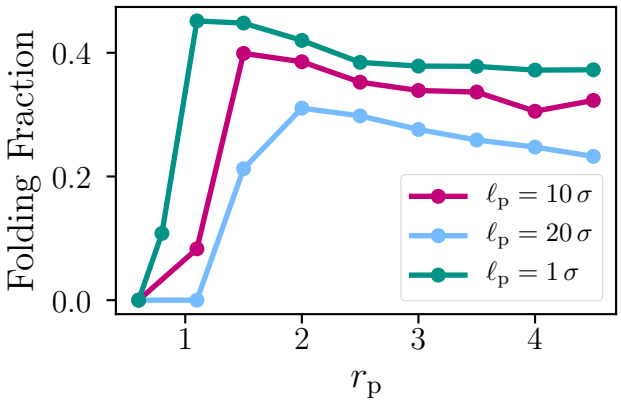

FIG. 8. The fraction of events that initiated translocation in a folded conformation across pore radii and persistence lengths.

in pore width can affect the conformation of the polymer as it is approaching the pore, leading to different translocation dynamics. We find that the deformations imparted by the field on the chain result in conformations that are not in equilibrium.

We classified the events into four types. In small pores we find two types of events, slow thread – fast translocation and fast thread – slow translocation, neither of which are present in the standard simulation protocol. Slow thread – fast translocation events have long waiting times with short translocation times, as they are compressed against the membrane prior to translocating. Fast thread – slow translocation events are characterized by elongated conformations, long translocation times, and short waiting times. As slightly larger pore sizes, both types of events are still present, but it becomes possible for chains to fold through the pore. Events folding through medium pores generally behave as slow thread – fast translocation events; they fold during the prolonged waiting between first contact and last thread. Further increases in pore size eliminate events with long waiting times entirely, as the barrier to thread after contact becomes negligible. Fast thread – slow translocation events become the dominant population. Folded events emerge due to the bending energy being easily overcome at large pores. Due to their folded conformation, these events have short waiting times and short translocation times. We find this classification of events to be valid for a range of persistence lengths, with the thresholds for different types of events changing.

The overall behaviour of the capture and translocation of semiflexible polymers with increasing pore width is very rich. Counterintuitively, as pore width increases, a bias emerges due to the electric field that favors stretched non-equilibrium conformations. We previously showed that similar effects can be achieved by pre-confining the polymer and forcing extended conformations as desired for various applications [18].

[1] M. Wanunu, Physics of life reviews **9**, 125 (2012).
[2] J. J. Kasianowicz, E. Brandin, D. Branton, and D. W. Deamer, Proceedings of the National Academy of Sciences **93**, 13770 (1996).
[3] C. Dekker, Nature nanotechnology **2**, 209 (2007).
[4] D. Branton, D. W. Deamer, A. Marziali, H. Bayley, S. A. Benner, T. Butler, M. Di Ventra, S. Garaj, A. Hibbs, X. Huang, *et al.*, in *Nanoscience And Technology: A Collection of Reviews from Nature Journals* (World Scientific, 2010) pp. 261–268.
[5] M. Muthukumar, *Polymer translocation* (CRC Press, 2016).
[6] G. W. Slater, C. Holm, M. V. Chubynsky, H. W. de Haan, A. Dubé, K. Grass, O. A. Hickey, C. Kingsburry, D. Sean, T. N. Shendruk, *et al.*, Electrophoresis **30**, 792 (2009).
[7] S. C. Vollmer and H. W. de Haan, The Journal of chemical physics **145**, 154902 (2016).
[8] F. Farahpour, A. Maleknejad, F. Varnik, and M. R. Ejtehadi, Soft Matter **9**, 2750 (2013).
[9] T. Sakaue, Physical Review E **76**, 021803 (2007).
[10] T. Saito and T. Sakaue, The European Physical Journal E **34**, 135 (2011).
[11] P. Rowghanian and A. Y. Grosberg, Physical Review E **86**, 011803 (2012).
[12] M. Doi and S. F. Edwards, *The theory of polymer dynamics*, Vol. 73 (oxford university press, 1988).
[13] A. Bhattacharya, Polymer Science Series C **55**, 60 (2013).
[14] J. Sarabadani, T. Ikonen, H. Mökkönen, T. Ala-Nissila, S. Carson, and M. Wanunu, Scientific Reports **7**, 7423 (2017).
[15] P. M. Suhonen and R. P. Linna, Physical Review E **97**, 062413 (2018).
[16] F. Wu, Y. Fu, X. Yang, L.-Z. Sun, and M.-B. Luo, Journal of Polymer Science Part B: Polymer Physics (2019).
[17] M. Magill, E. Waller, and H. W. de Haan, The Journal of Chemical Physics **149**, 174903 (2018).
[18] K. Briggs, G. Madejski, M. Magill, K. Kastritis, H. W. de Haan, J. L. McGrath, and V. Tabard-Cossa, Nano letters **18**, 660 (2017).
[19] J. A. Anderson, C. D. Lorenz, and A. Travesset, Journal of Computational Physics **227**, 5342 (2008).
[20] J. Glaser, T. D. Nguyen, J. A. Anderson, P. Lui, F. Spiga, J. A. Millan, D. C. Morse, and S. C. Glotzer, Computer Physics Communications **192**, 97 (2015).
[21] L. D. Landau and E. M. Lifshitz, *Course of theoretical physics* (Elsevier, 2013).
[22] G. S. Grest and K. Kremer, Physical Review A **33**, 3628 (1986).
[23] S. W. Kowalczyk, A. Y. Grosberg, Y. Rabin, and C. Dekker, Nanotechnology **22**, 315101 (2011).
[24] M. Mihovilovic, N. Hagerty, and D. Stein, Physical Review Letters **110**, 028102 (2013).

Appendix A: Polymers that diffuse after contact

Although we expected that the chains would stay near the nanopore after contact, our choice to keep the contact radius constant across pore radii resulted in that not being the case for the smallest pores. The chains would diffuse far away but not so far that they were considered diffused into the bulk.

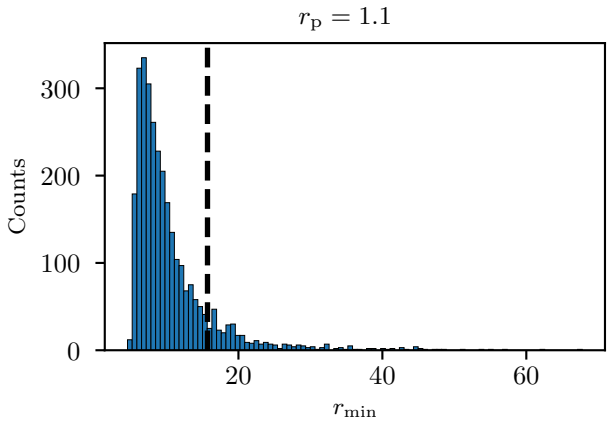

FIG. 9. The radial distance of the monomer closest to the pore after contact. The black dashed line corresponds to the cutoff $\langle R_g \rangle_{SF}$.

To understand the magnitude of this occurence we kept track of the distance the entire polymer had diffused away from the pore after first contact. Figure 9 shows a histogram of the maximum distance the monomer radially closest to the pore would have over the course of a simulation over all succesfull translocation events. As shown in Figure 9, most polymers diffuse around the vicinity of the pore, and only a few tend to drift away. To account for this, we implemented a cutoff distance. Once the entire polymer diffused past this cutoff distance it would be counted as a new event. To obtain an estimate of the cutoff we look to the deformation radius simulation for the pore size at hand as our main concern is the conformation of the chain changing significantly should the chain move too far. Figure 10 shows the radial radius of gyration for $r_p = 1.1\sigma$ as a function of r_{min}.

Upon examining Figure 10 we see that the polymers radial radius of gyration is mostly the same up to $\approx 15\,\sigma$ away from the pore. Indeed, if we look at the dashed line in Figure 9 we see that this cutoff does a good job of including the fluctuations near the pore while excluding the long tail of events that diffused further.

Appendix B: Re-defining translocation by an end

The semiflexibility inherent to our polymer model is not compatible with the simplest definition of translocation by an end ($s_t > 0$). Due to the semiflexibility there are strong correlations between the exact ends of the chain and several monomers nearest to the ends. For a better working definition, we relaxed the criterion for folded translocation to include the monomers nearest to

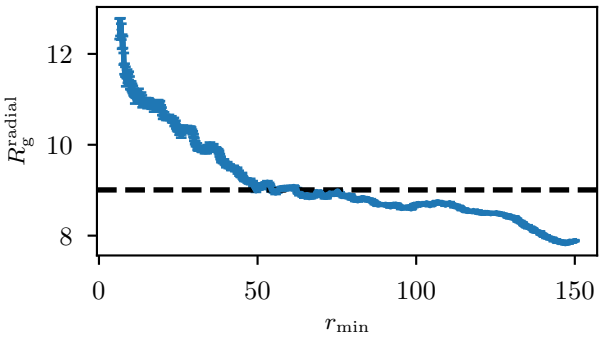

FIG. 10. R_g^{radial} binned by the radial distance r_{min} of the monomer closest to the nanopore. The black dashed line represents one third of the radius of gyration of the worm like chain calculated with Equation 8 which corresponds to being at an equilibrium conformation in the direction radial to the pore.

the ends of the chain. To determine a suitable cutoff, we looked at the correlation between the first contact location and the last thread location only for events that folded under the simple definition. Figure 11 shows contact location and thread location for events whose thread location was not the end monomers of the polymers. As shown in Figure 11, at values lower than $s_t \approx 0.1$ the translocation times are rather high, a feature corresponding to elongated conformations, and they start to decrease as we move away from that value. Using this result, we chose our criterion for folding as $s_t \geq 0.1$.

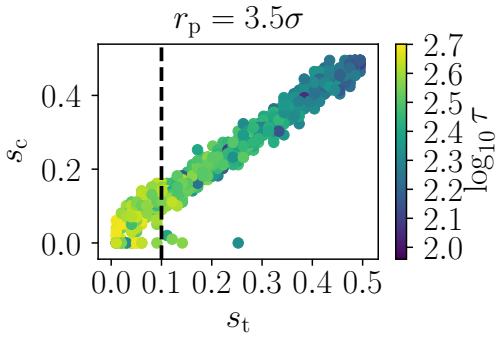

FIG. 11. The correlation of contact location and thread location with the color being the log of translocation time. The data is filtered to only include events that threaded by any monomer other than the ends of the chain.

Chapter 3

DNA Translocations through Nanopores under Nanoscale Preconfinement

NANO LETTERS
Cite This: Nano Lett. 2018, 18, 660−668
Letter
pubs.acs.org/NanoLett

DNA Translocations through Nanopores under Nanoscale Preconfinement

Kyle Briggs,[†] Gregory Madejski,[‡] Martin Magill,[§] Konstantinos Kastritis,[§] Hendrick W. de Haan,[§] James L. McGrath,[‡] and Vincent Tabard-Cossa*[,†]

[†]Department of Physics, University of Ottawa, Ottawa, Ontario K1N 6N5, Canada
[‡]Department of Biomedical Engineering, University of Rochester, Rochester, New York 14627, United States
[§]Faculty of Science, University of Ontario Institute of Technology, Oshawa, Ontario L1H 7K4, Canada

Supporting Information

ABSTRACT: To reduce unwanted variation in the passage speed of DNA through solid-state nanopores, we demonstrate nanoscale preconfinement of translocating molecules using an ultrathin nanoporous silicon nitride membrane separated from a single sensing nanopore by a nanoscale cavity. We present comprehensive experimental and simulation results demonstrating that the presence of an integrated nanofilter within nanoscale distances of the sensing pore eliminates the dependence of molecular passage time distributions on pore size, revealing a global minimum in the coefficient of variation of the passage time. These results provide experimental verification that the inter- and intramolecular passage time variation depends on the conformational entropy of each molecule prior to translocation. Furthermore, we show that the observed consistently narrower passage time distributions enables a more reliable DNA length separation independent of pore size and stability. We also demonstrate that the composite nanofilter/nanopore devices can be configured to suppress the frequency of folded translocations, ensuring single-file passage of captured DNA molecules. By greatly increasing the rate at which usable data can be collected, these unique attributes will offer significant practical advantages to many solid-state nanopore-based sensing schemes, including sequencing, genomic mapping, and barcoded target detection.

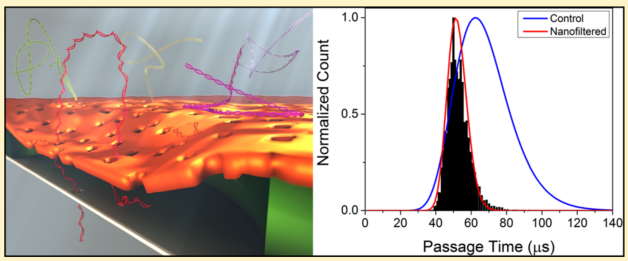

KEYWORDS: *Nanopore, nanotechnology, nanofabrication, DNA, entropy, nanoconfinement*

When a single biopolymer such as DNA translocates a nanopore, the dynamics of molecular transport are complex.[1−5] The speed during passage is thought to be dependent on the fraction and conformation of the molecule outside the pore,[6] as well as being subject to thermal fluctuations and transient interactions with the pore walls and membrane materials.[7−9] The net effect is for the molecular motion to be afflicted by a wide distribution of passage speeds, both due to inter- and intramolecular velocity fluctuations.[1] Such a spread in passage times confounds simple translation of time to molecular position, complicating mapping applications, and greatly limits the ability of the nanopore to distinguish charged molecules by size compared to traditional gel-based electrophoresis techniques.

Most experimental efforts aimed at controlling the speed of molecular translocation through a solid-state nanopore have focused on slowing DNA by various means, including interfacing the pore with a gel;[10,11] by judicious choice of electrolyte, both aqueous[12] and ionic-liquid;[13] by laser-modulating the surface charge density;[14] by adjustment of the viscosity;[15] or by using different membrane materials.[16,17] While these methods are able to slow DNA translocations to varying degrees, they generally do so at the cost of wider passage time distributions.

Few studies have considered the factors that contribute to the wide distributions of passage times. Experimentally, the choice of salt solution has been shown to have a significant effect on the width of passage time distributions,[12] while a pore with diameter matched to the size of DNA limited DNA self-interaction and reduced the variation in passage time.[18] Barcoded molecules have also been used to explore intramolecular variation in passage times, revealing speed up toward the end of the translocation,[19] and it was found that Brownian motion alone is insufficient to explain the observed variations.[20,21] Simulation work, on the other hand, has demonstrated that polymers are perturbed from equilibrium by the extended electric field gradient during the capture process,[22] changing the passage time distribution compared to equilibrium predictions. In addition, molecules which are extended prior to translocation have longer passage times due to increased drag forces.[6]

Received: September 20, 2017
Revised: October 27, 2017
Published: October 31, 2017

DOI: 10.1021/acs.nanolett.7b03987
Nano Lett. 2018, 18, 660−668

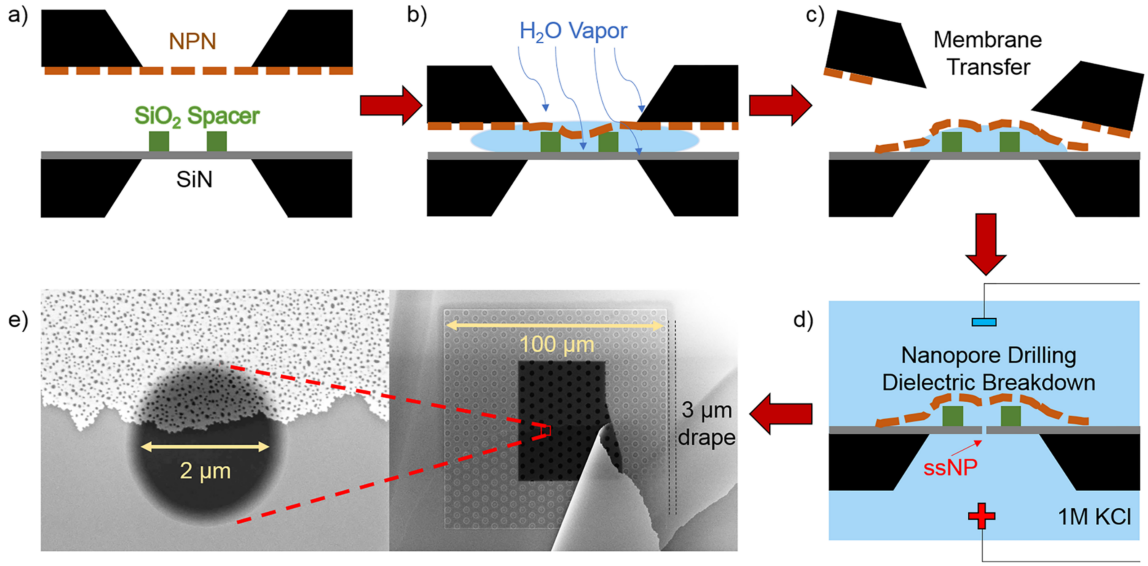

Figure 1. (a) 50 nm NPN membrane is aligned to a 20 nm SiN membrane, patterned with a 200 nm SiO_2 spacer. (b) Condensation of water vapor penetrates the NPN membrane, inundates the nanocavity, and draws the NPN membrane to the SiO_2 spacer. (c) The NPN membrane is torn away from the carrier chip by surface tension and remains attached to the SiO_2 spacer and SiN surface. (d) Nanopore fabrication by a controlled breakdown with the nanofilter already in place. (e) SEM image of a device after step c. A section of NPN membrane is torn away, revealing the SiO_2 spacer underneath. The pore may be formed in any oxide microwell in the darker central region, which corresponds to the free-standing SiN membrane. The device shown in this SEM image has a 2 μm microwell, whereas the devices used in the rest of the paper use 1 μm microwells.

Unfortunately, while the dominant mechanism responsible for high variability in passage time is thought to be the large conformational entropy available to DNA molecules prior to translocation through the nanopore,[23] experimental verification has remained difficult due to the complexity of fabricating devices with sufficiently confining geometries in the vicinity of a nanopore.[24−27] Recent work, employing the confining geometry of nanopipette-based conical nanopores, has provided evidence that polymer entropy prior to translocation is related to mean passage time but did not consider the standard deviation.[28] In this work, we present the first experimental verification that entropy reduction through preconfinement of DNA reduces the passage time variation inherent in nanopore transport processes. Confinement is achieved by taking advantage of the extreme flexibility and permeability of ultrathin (50 nm) nanoporous silicon nitride (NPN) membranes[29,30] to place them within nanoscale distances of a solid-state nanopore sensor while still allowing fluidic contact in an innovative single-molecule biosensor configuration.

The nanofiltered nanopore device architecture realizes a two-membrane system, comprised of an ultrathin, nanoporous layer of 50 nm thick NPN membrane, separated by a 200 nm gap from a 20 nm thick silicon nitride (SiN) membrane. This essentially creates an architecture comprising two pores in series. NPN is a recently developed highly porous nanomembrane technology with tunable pore sizes (20−80 nm) and porosities (1−40%).[29] The gap between the nanofilter and SiN membranes is achieved through the lithographic patterning of a hexagonal grid of 1 μm diameter holes in a 200 nm thick SiO_2 layer deposited on top of SiN. A backside etch then creates a freestanding SiN membrane beneath cylindrical SiO_2 cavities spaced 5 μm apart. The nanofilter is passively held in place directly above these oxide wells, most likely by van der Waals forces. A schematic and electron microscopy images of the device assembly process are shown in Figure 1.

Unless otherwise noted, the nanofilter membranes used in this work had a porosity of 5%, with an average pore diameter of 49 ± 8 nm (mean ± standard deviation), corresponding to a number density of ~25 pores/μm^2. With this setup, each 1 μm diameter circular oxide microwell (0.785 μm^2) contains 20 ± 5 pores. Wetting of the space between the membranes is achievable due to the extraordinary high gas permeability of the ultrathin nanofilter membrane.[31] This device is mounted in a fluidic flow-through cell, exposed to an aqueous salt solution, and a single nanopore is fabricated in the SiN membrane using controlled breakdown (CBD), described elsewhere.[32,33] The CBD process produces a single nanopore in one of the oxide wells at random.[34] Due to the low electrical resistance of ultrathin highly porous NPN, the presence of the nanofilter has negligible effect on CBD and on the electrical characteristics of the resulting single nanopore (referred to hereafter as the sensing pore). Further details of the NPN material properties, pore fabrication process, and nanosensor electrical characterization are presented in Supplementary Section S1.

Simulations were also conducted to better understand the behavior of nanofiltered pores. A standard coarse-grained polymer model was used to model the DNA chains.[35] The driving electric field was solved numerically between the nanofilter and the sensing pore, and approximated analytically elsewhere. Only a single pore in the nanofilter was explicitly represented in simulations, placed 150 nm off-axis from the sensing pore, which was located in the center of the microwell. Further details of the simulation setup are provided in Supplementary Section S2.

Double-stranded DNA (dsDNA) molecules of lengths varying from 100 bp to 4000 bp are introduced to the cis (nanofilter) side of the system and are driven through the system by a voltage bias of 200 mV in 3.6 M LiCl pH 8 unless otherwise noted. Because the resistance of the sensing pore dominates that of the nanofilter, the current blockage that is sensed is due entirely to the interaction between dsDNA

DOI: 10.1021/acs.nanolett.7b03987
Nano Lett. 2018, 18, 660−668

molecules and the sensing pore, while the nanofilter remains electrically invisible. Interestingly, the capture rate of nanofiltered devices is comparable to the capture rate of control devices in most cases. Detailed event counts and capture rates are available in Supplementary Table S1 and Supplementary Section S3.

Following Mihovilovic et al.,[36] we define type 1 events to be single-file passage of dsDNA, type 21 events to be partially folded events in which the event begins in the folded state. More complex event shapes are indicated by longer strings of integers, which correspond to integer multiples of the single-file dsDNA blockage in the order in which they appear. Events containing levels which do not correspond to an integer multiple of the level 1 blockage are labeled anomalous and are excluded from subsequent analysis. These comprise less than 5% of events overall and are typically attributed to interactions of DNA with the access regions of nanopores,[37] or to fitting artifacts.

We first consider the kinetics of passage of molecules which pass the sensing pore in an unfolded type 1 configuration. Figure 2a–c show schematic representations of possible conformations of dsDNA prior to translocation through the sensing pore. As can be seen in Figure 2d, when $N \lesssim 1300$ bp, there is a single population of passage times for single-file passage which is well-characterized by a log-normal distribution. For $N \gtrsim 1300$ bp (Figure 2e and f), a one-sided tail appears in addition to the log-normal component, comprising events with very long passage times. We attribute the log-normal portion of the passage time distributions to unhindered passage through the two serial membranes. Details of the analysis, along with event counts, are shown in Supplementary Section S3.

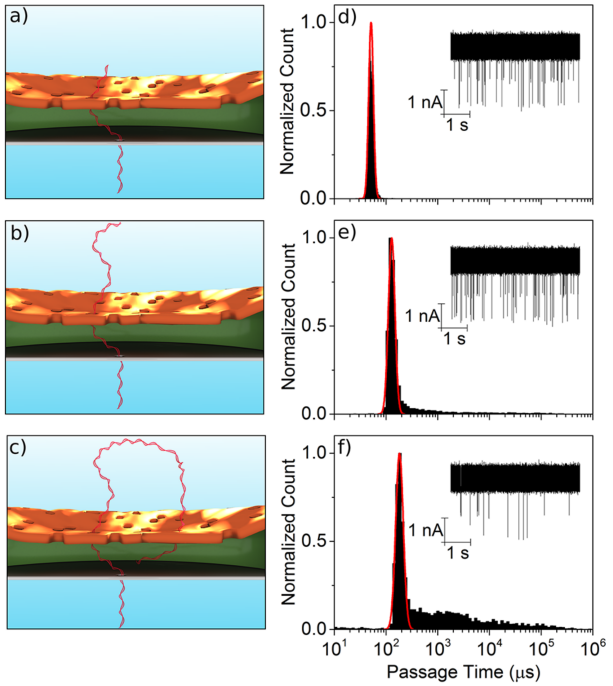

Figure 2. (a, b, c) Schematic representations of 1000, 2000, and 3000 bp dsDNA traversing the nanofiltered pore device, respectively. Vertical distance and DNA length is to scale. (d, e, f) Passage time histograms of unfolded type 1 events for the corresponding lengths of dsDNA. All three histograms are obtained using the same pore, while the pore grew during the course of the experiment (4.3 h), from top to bottom, from 6.7 nm, to 7.3 nm, and finally to 8.0 nm, respectively. Insets: time series of dsDNA translocations (including folded events) for the corresponding histogram. Data recorded at 4.166 MHz sampling rate, digitally filtered with a low-pass Bessel filter at 900 kHz, and down-sampled to 2.5 MHz for plotting.

Figure 3 shows properties of unhindered dsDNA passage time distributions as a function of the number of base pairs N, representing fits to data extracted from a total of 1.3 million individual DNA translocations through eight nanofiltered pores and seven control pores.

The mean passage time τ for nanofiltered pores is fitted well by a single power law,

$$\tau(N) = \tau_0 N^p \tag{1}$$

which yields an exponent of $p_{exp} = 1.19 \pm 0.06$, as shown in Figure 3a. This exponent is in reasonable agreement with previous studies on regular solid-state nanopores.[36,38,39] Error bars define the 95% confidence interval for the fit parameters. Control devices without the nanofilter (Figure 3b) behave similarly, but with slightly larger spread in mean passage times. Simulations (Figure 3c) also show power law scaling, though the exponent, $p_{sim} = 1.61 \pm 0.02$, is larger than in the experimental case. This is consistent with previous work, since simulations typically find scaling exponents which are larger than those extracted from experiments.[40,41]

The effect of the nanofilter becomes more apparent when considering the standard deviation σ of the passage time (Figure 3d–f), where the nanofilter usually results in significantly lower standard deviations than the control case. Experimental data with the nanofilter are fitted by a two-power law:

$$\sigma(N) = \sigma_0\left(\left(\frac{N}{N^*}\right)^q + \left(\frac{N}{N^*}\right)^r\right) \tag{2}$$

The experimental best-fit exponents for this form are $q_{exp} = 0.5 \pm 0.3$ and $r_{exp} = 2.0 \pm 0.6$, in reasonable agreement with $q_{sim} = 0.3 \pm 0.5$ and $r_{sim} = 2.1 \pm 0.2$ for the simulated data. The standard deviation thus exhibits a crossover between different power laws for small and large N, as discussed below.

As a consequence of the mean and standard deviation passage times scaling behavior, the coefficient of variation σ/τ exhibits nonmonotonic behavior and has a global minimum which can be seen in Figure 3g and i. The origins of this minimum can be explained by examining the simulation data for the translocation time and standard deviation (Figure 3c and f). At short lengths, the standard deviation grows weakly with increasing DNA length. In this limit, the DNA is rod-like, and thus increasing the length of the DNA causes minute variations in the available conformations at the start of translocation. On the other hand, for rod-like polymers, the friction coefficient grows approximately with the length of the rod,[42] and thus, the translocation time does increase significantly. Hence, a weakly growing standard deviation normalized by an increasing translocation time yields a decreasing coefficient of variation. This rod-like limit breaks down around the Kuhn length, where the variation of initial conformations increasingly influences the distribution of translocation times. Indeed, the standard deviation is seen to increase strongly with increasing length for $N > 300$ bp (slightly above the Kuhn length in simulations). The onset of this additional source of variation causes the increase in standard

DOI: 10.1021/acs.nanolett.7b03987
Nano Lett. 2018, 18, 660–668

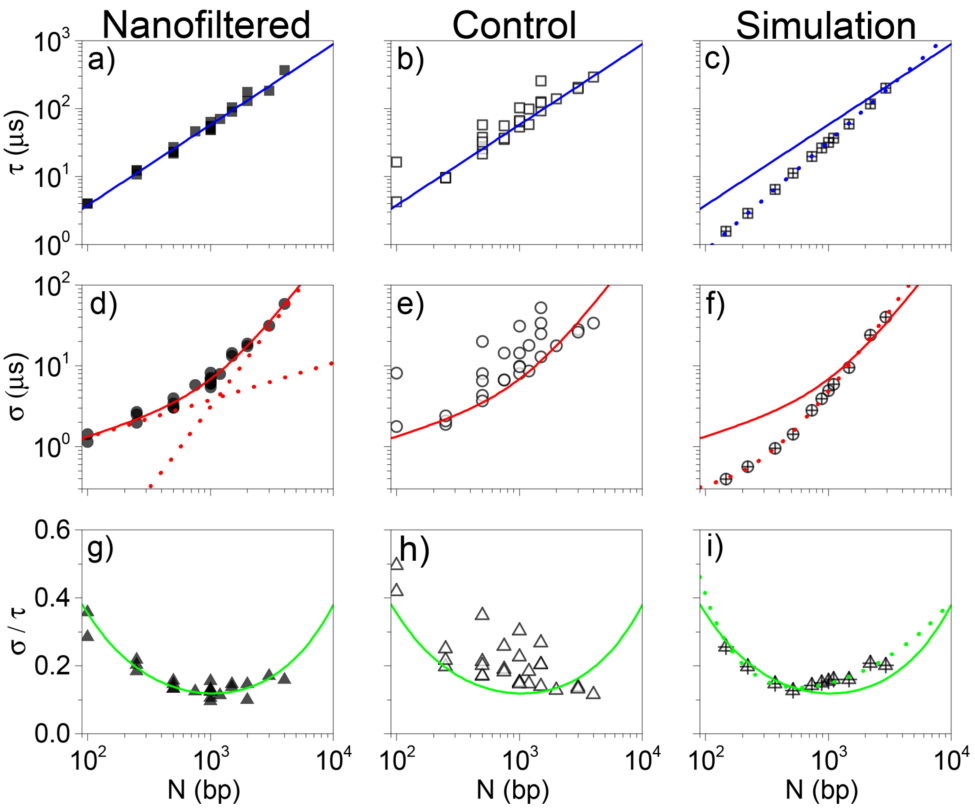

Figure 3. Mean passage times for (a) nanofiltered, (b) control, and (c) simulated nanofiltered pores as a function of DNA length. The solid blue lines are a fit of eq 1 to the data in a, while the dashed line in c is a fit to the simulated data. Standard deviation of passage times for (d) nanofiltered, (e) control, and (f) simulated nanofiltered pores. The solid red lines are a fit of eq 2 to the data in panel d. The dotted lines in d show the two power laws separately, while the dotted line in f shows the two-power fit to the simulated results. Coefficient of variation for (g) nanofiltered, (h) control, and (i) simulated nanofiltered pores. The solid green lines are the quotient of the fits in a and d, while the dotted line in panel i is the quotient of the fits to simulated data.

deviation to outpace that in the mean passage time, thus increasing the coefficient of variation. The combination of these effects is a minimum between these two regimes.

In the controls (Figure 3e), we see that deviations from the fit to nanofiltered pore data are always biased toward larger standard deviations (note the log scale). For a given molecular size, sensing pores equipped with a nanofilter set a lower bound for the standard deviation that is achievable by the sensing pore. To understand this trend, we consider recent simulation work which showed that the gradient in the electric field outside of nanopores can stretch out polymers as they are captured prior to translocation since polymer segments that are closer to the pore experience a larger electrophoretic force than those further away.[22,43] The distance from the pore at which elongation occurs can be estimated by considering the capture distance at which the electrophoretic force overcomes diffusion, which is proportional to the square of the pore diameter.[44] The experimental data in Figure 4 are collected for several devices in which the sensing pore diameter was varied between 3 and 14 nm. This translates into a variation of the capture distance over more than an order of magnitude. Hence, in the absence of the nanofilter, the DNA will be consistently elongated for large pores but much less so for small pores. The effects of this are experimentally observed in the control data in Figure 4b: large pores exhibit a smaller variation in the conformation of the dsDNA prior to translocation and thus a smaller standard deviation in the translocation times compared to the more variable conformations expected for smaller pores. In the presence of the nanofilter, sufficiently long dsDNA must uncoil to thread through the nanofilter and is thus biased to approach the sensing pore in an elongated conformation independent of the sensing pore size. Consequently, the nanofilter reduces the variability in the initial conformation and improves the standard deviation beyond what can be consistently achieved with large sensing pores alone and more importantly removes the dependence of passage time standard deviation on sensing pore size and stability. We demonstrate that this effect can be used to improve the resolution and the reliability of nanopore polymer size spectroscopy, an application which is discussed in Supplementary Section S4.

It is also interesting to note that the normalized mean passage time has a pore size dependence, with smaller control pores actually leading to slower translocation than their nanofiltered counterparts. Since an elongated polymer is expected to have more drag and thus take more time to translocate,[6] this is counterintuitive. We attribute this observation to additional friction arising from interactions between the coiled polymers that approach small control pore both with itself (coil−coil interactions) and the surrounding membrane (coil−membrane interactions), as depicted in Figure 4d. Because these polymers are not elongated, their conformation renders them more prone to interact with the membrane surrounding the mouth of the pore, potentially leading to temporary weak sticking, whereas elongated

DOI: 10.1021/acs.nanolett.7b03987
Nano Lett. 2018, 18, 660−668

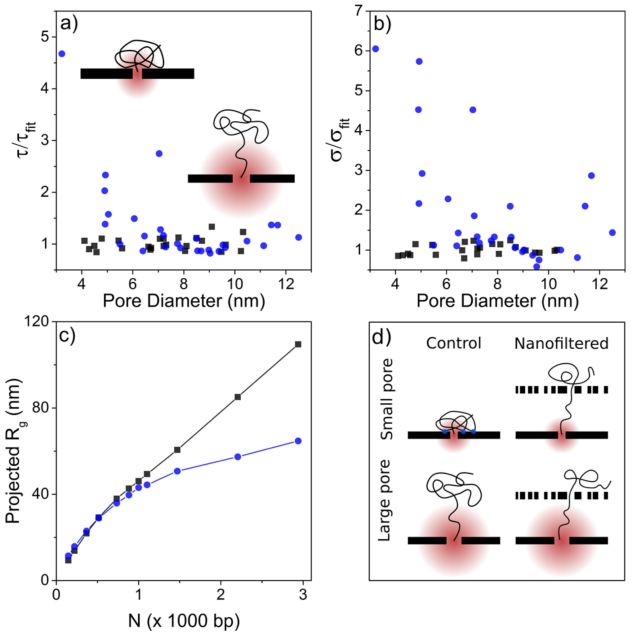

Figure 4. (a) Experimental mean passage times normalized by the fit of eq 1 as a function of sensing pore size for both nanofiltered (black squares) and control pores (blue circles). Inset schematics show the stretching of the polymer as it enters the capture radius of control pores for two different pore sizes. (b) Experimental standard deviation normalized by the fit of eq 2 as a function of sensing pore size. (c) Simulated projection of the radius of gyration on the vector connecting the sensing pore and the center of mass of the DNA at the moment of capture, for molecules initialized with one end in the nanofilter (black squares) versus one end in the sensing pore (blue circles). (d) Schematics illustrating the expected conformations of polymers at the onset of translocation for small and large pores with and without the nanofilter. Red gradients depict the electric profile outside the pore, while blue dots represent the potential interaction sites between the polymer and the membrane outside the pore.

polymers will not be subject to this slowing effect. The proposed mechanisms slowing translocation in the control pores are explored in more detail in Supplementary Section S5.

To further elucidate the origin of the minimum in the coefficient of variation and to confirm that molecules which pass through the nanofilter tend to be more elongated than those that do not, additional simulations were conducted wherein the dsDNA was initialized by equilibrating with one end fixed in the sensing pore (Figure 4c). In this configuration, DNA are much less elongated on average. However, in these simulations where the nanofilter plays little to no role, the crossover in the standard deviation of the passage time and the global minimum in the coefficient of variation are still observed, albeit at slightly shorter chain lengths. The fact that this crossover behavior is also visible as the lower bound in the control experiments for both standard deviation (Figure 3d) and the coefficient of variation (Figure 3g) point to a molecular property of the polymers, namely, the polymer stiffness, being responsible for the presence of the minimum in the coefficient of variation, rather than the presence of the nanofilter. The nanofilter is the mechanism by which the sensing pore can achieve the minimal standard deviation required to actually map the transition. Therefore, fundamental physics of polymer translocations are revealed by the presence of the nanofilter. This crossover behavior has always been present but has until now been indistinguishable from noise.

In principle, prestretching of the polymer is not the only way in which to achieve a reduction in the standard deviation of the passage time. As long as the conformational entropy is reduced, the passage time will be more consistent regardless of the subset of conformation space that is selected. Different confining geometries prior to translocation through the pore can in theory produce similar effects.[23] However, Figure 4a suggests that membrane interactions may play an important role in variability in the translocation process. Prestretching is capable of mitigating membrane interactions while simulta-

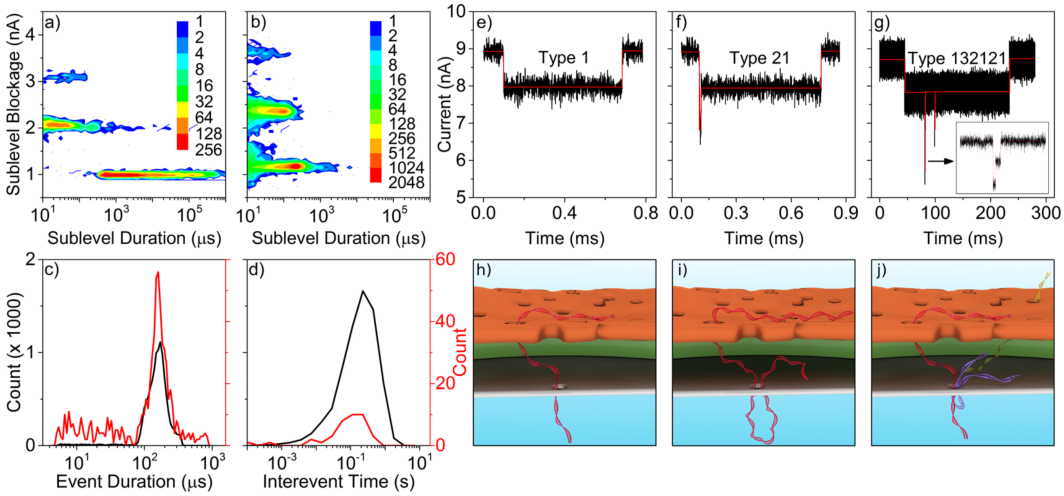

Figure 5. (a) Heat map of sublevels within events, showing blockage depth as a function of sublevel duration for events which fall within the tail of long events for 3000 bp dsDNA in an 8.0 nm nanofiltered pore. (b) For comparison, the sublevel breakdown for a control pore (no nanofilter), showing that the long tail of events is absent. (c, d) Distribution of passage times and interevent times respectively for superimposed events within long single-level events (red) compared to the passage time distribution for unhindered events from the same pore (black). (e–g) Examples of a single-level, unfolded type 1 event, a briefly initially folded type 21 event, and a more complex event, respectively, from among the 3000 bp double-threaded events. (h–j) schematic representations of the molecular conformations giving rise to each of the corresponding event signatures above. Red DNA represents a polymer which is adsorbed to the filter, while other colors translocate freely.

DOI: 10.1021/acs.nanolett.7b03987
Nano Lett. 2018, 18, 660–668

neously reducing conformational entropy, which need not be the case for any confining geometries.

While large control pores can sometimes approach the performance of nanofiltered pores, the results presented in Figures 3 and 4 show that the presence of the nanofilter idealizes the sensing pore, allowing the system to consistently achieve a minimal standard deviation and coefficient of variation. In addition, a remarkable feature of nanofiltered pores is the fact that this minimization happens independent of sensing pore size. In several cases the pore size was observed to grow over the course of a single experiment (Supplementary Table S1), without compromising the improvement to the passage time characteristics. This independence of the sensor on both pore size and pore stability, made possible by the presence of the nanofilter within nanoscale distances of the sensing pore, is a feature of clear importance to many solid-state nanopore-based technologies.

We attribute the long events which appear in Figure 2e and f to translocation which has one end of the dsDNA temporarily adsorbed to the nanofilter during capture of the other end by the sensing pore. Several other plausible explanations for the long events are discussed and ruled out in Supplementary Section S6. To support this picture, we define adsorbed events as events with passage times exceeding four standard deviations above the mean for the log-normal portion of the passage time distribution on a log-scale. Figure 5a shows the sublevel blockage depth as a function of duration for all of the events with long passage times for 3000 bp molecules translocating a nanofiltered pore. It can be compared to the full set of sublevels for a similar control pore (Figure 5b), which does not have the extended tail of long events. While most long events show a single blockage level (Figure 5c and h), blockage states corresponding to occupation of the pore by more than one dsDNA molecule are present in some events. These deeper blockage levels are always very short compared to the unfolded sublevel and for the majority of events appear only at the very start of events (type 21, Figure 5f and i). These latter events correspond to a dsDNA adsorbed on the nanofilter, which is captured in a folded configuration very near an end and then proceeds to occupy the pore in an unfolded conformation for the remainder of its length. However, there is a significant population of complex events which contain levels corresponding to two and three times the single occupation level in the middle of an extended stretch of single occupancy, which cannot generally be explained by interactions of a single molecule with the pore (Figure 5g and j). We attribute these superimposed events to simultaneous translocation of a second, unhindered dsDNA molecule, while the pore is partially occluded by a single DNA molecule adsorbed on the nanofilter. To support this, we note that the passage time distributions for superimposed events are similar to those for regular unhindered events (Figure 5c). The interevent time distributions for superimposed events are also consistent with the unhindered translocations (Figures 5d).

As dsDNA length increases even further, the passage time distribution eventually becomes dominated by long events as all of the molecules thread through multiple pores in the nanofilter and arrive with both ends in the sensing pore in a double-threaded configuration. The sensing pore then exhibits very predictable clogging modes closely matching the expected blockage level for folded dsDNA, which we attribute to simultaneous capture of both ends of the DNA by the sensing pore while it is double-threaded through two pores in the nanofilter. Additional discussion of clogging by long molecules is presented in Supplementary Section S6.

In addition to augmenting the standard deviation of molecular passage time distributions through a nanopore, the large degree of conformational entropy available to semiflexible polymers also leads to folded translocation, in which a polymer is captured from somewhere along the length of the molecule and translocates in a hairpin conformation. This is particularly problematic for genomic mapping and barcoding schemes in which a DNA molecule is tagged with a marker, either to determine the presence or location of a particular sequence,[45−47] the presence of a target,[20] or to map the velocity profile of translocating molecules.[19] In such applications, folded translocations are generally excluded from data analysis, which can result in having to ignore many translocation events entirely. As a result, ensuring single-file passage of dsDNA through pores of any size is of high technological importance for many diagnostic and genomics applications[20,45,47,48] that rely on detecting and mapping bound probes. While it is possible to restrict folding by using a nanopore too small to allow it, this is often incompatible with bulky labeling schemes and can be sensitive to pore instability.[49,50]

We observed complete elimination of dsDNA folding during translocation through the sensing pore in two nanofiltered pore devices, despite the sensing pore being sufficiently large in both cases to allow for folded passage. The first of these pores is discussed in detail in Supplementary Section S7. Both of these devices had in common a low event rate compared to the rest of the nanofiltered devices. Due to the variability of folding behavior between nanofiltered devices, the origin of this effect must lie with the particular details of each individual nanofilter. We hypothesize that the mechanism behind folding suppression is the variation in the local distribution of nanofilter pore positions in the vicinity of the sensing pore. As discussed in Supplementary Section S7, only a small number of nanofilter pores which are very close to the sensing pore are active and have a sufficiently high electric field to capture dsDNA, so the local nanofilter pore distribution can be different between devices. In particular, if a device has two active nanofilter pores which are very close together compared to the extent of the dsDNA, the probability of a dsDNA molecule threading through both nanofilter pores will be high. Because of the electric field gradient between the two membranes, double-threaded polymers will tend to favor capture by one end, and translocation will proceed unfolded due to the resulting elongation.

To test this hypothesis, we performed experiments using a different nanofilter material, which had slightly smaller pores (38 ± 12 nm) but higher porosity (16 ± 3%), yielding more closely spaced nanofilter pores which would promote double-threading. Due to the smaller nanofilter pores, a higher voltage of 400 mV was required to obtain a sufficiently high event rate to gather statistics.

A dramatic demonstration of the hypothesized physical picture is shown in Figure 6. The device suppressed folding almost completely during the first part of the experiment (Figure 6a and b). Subsequently, the sensing pore clogged and exhibited increased noise centered around a single-occupancy clog for a few minutes. When the clog cleared the sensing pore, with the open pore current baseline returning to its previous value, subsequent events presented folding (Figure 6a and c). The most likely explanation is that one of the two closely spaced nanofilter pores was permanently clogged during the

DOI: 10.1021/acs.nanolett.7b03987
Nano Lett. 2018, 18, 660−668

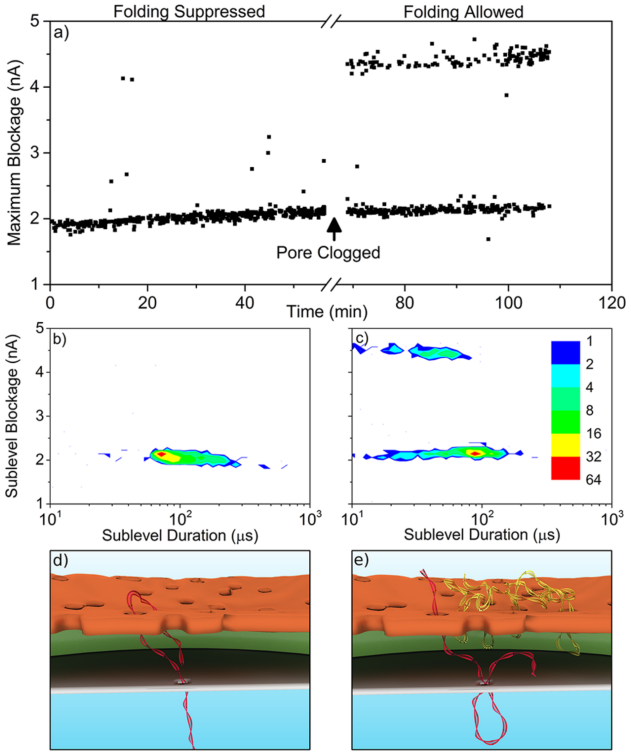

Figure 6. (a) Maximum blockage as a function of experiment time, showing near-complete suppression of folding during the first half of the experiment, followed by allowing folding after a period of prolonged clogging. The single-occupancy blockage level is around 2 nA for this 5.4 nm sensing pore. (b) Heat map of the sublevels for events from the folding-suppressed half of the experiment. (c) Heat map of the sublevels for events from the folding-allowed half of the experiment, following clogging of the sensing pore. (d) Schematic of the hypothesized mechanism of folding suppression consisting of two closely spaced nanofilter pores. (e) Schematic depicting how the folding suppression can be lost when one or more of the active nanofilter pores is clogged.

period in which the sensing pore was clogged, and since the local properties of the nanofilter no longer promoted double-threading, folding was no longer suppressed.

In light of this, we expect that folding suppression can be achieved reliably if the nanofilter parameters can be chosen so as to promote double threading of DNA molecules en route to the sensing pore. As long as the edge-to-edge distance between adjacent active nanofilter pores is smaller than the free solution radius of gyration of the polymer, we expect this probability to be high, while small nanofilter pores will promote unwinding of the dsDNA molecule as it passes into the space between the membranes. Further discussion of folding kinetics can be found in Supplementary Section S7.

One of the reasons preconfinement of molecules through the use of two-membrane systems has proven experimentally challenging is the difficulty inherent in producing two adequately spaced, precisely sized, serial nanopores while having fluidic access to the nanoscale gap between them for the purposes of wetting. The nanofiltered pore device presented herein creates a composite structure which achieves an optimal balance between these requirements while keeping the complexity minimal: the ultrathin, porous nanofilter material allows easy wetting and simple fluidic and electrical access to the intermediate space for the purposes of nanopore fabrication by CBD, which guarantees the presence of appropriately aligned nanopores without requiring visual confirmation, and eliminates both the requirement for precise nanopore size and the deleterious effects of size instability during sensing.

The combined simulation and experimental results obtained on this nanofiltered pore device demonstrate the strong influence the capture process has on the dynamics of DNA translocation and reveal the presence, previously hidden in the noise, of a minimum in the normalized variance of translocation times that is inherent to semiflexible polymers. The presence of the nanofilter upstream of the nanopore sensor prestretches the polymer, which offers a significant reduction in variation of passage times. This composite structure will enable a broad range of applications and provide enhanced sensing capabilities. It can be leveraged to provide more precise polymer size separation and to suppress folded translocations, thus forcing single-file passage, of critical importance for many life science and health applications, including DNA sizing, barcoded target detection, and genome mapping.

Methods. *Nanofilter Assembly.* The NPN nanofilter membranes and SiN/oxide microwell substrate chips (SiMPore Inc., West Henrietta, NY) are cleaned with a nitrogen flow, followed by 38 W air plasma for 40 s to make all surfaces hydrophilic. Both the substrate and nanofilter chips are placed into gentle contact using a custom aluminum jig and placed in a −15° C freezer for 2 min to cool below room temperature. The assembly is then exposed to fine mist produced by a vaporizer, which condenses on the cooled surface and fills the cavity between the two membranes. As the liquid evaporates through the nanofilter, surface tension pulls the two membranes into contact, which then remain sealed together once all of the liquid has evaporated. The two chips are then separated mechanically, and the nanofilter is left behind in contact with the substrate chip. To completely seal the nanofilter and to reduce chip capacitance, polydimethylsiloxane (PDMS) is then painted over the entire chip surface, leaving only the free-standing membrane portion exposed. This assembly can be stored until use.

Just before use, the assembly is air plasma cleaned at 38 W for 40 s to make all surfaces hydrophilic. The cleaned assembly is then placed in a sealed container with ambient air (40% humidity), and this container is placed in the −15° C freezer for up to 5 min. The cooling condenses humidity in the microwell, wetting the gap between the two membranes.

Nanopore Fabrication by CBD. Nanopores are fabricated in nanofilter assemblies via CBD, which is described elsewhere.[32] Briefly, pores are formed in 1 M KCl pH 10 using a slowly increasing voltage ramp from −10 V to −18 V applied to the nanofilter side of the assembly, with the trans side grounded. Typical fabrication times are between 5 and 10 min. Once fabricated, the salt solution is changed to 3.6 M LiCl pH 8, and depending on the initial pore size, the diameter is adjusted using 3−4 V 4s square voltage pulses until the desired pore in the range of 6−15 nm is achieved. Depending on the IV and noise characteristics, pores are sometimes aged before use.[7]

Data Acquisition and Analysis. NoLimits dsDNA molecules (Life Technologies Inc.) in the range of 100−4000 bp are premixed to the desired concentration (between 3 and 76 nM) and injected into the vicinity of the pore using a custom PEEK flow cell.

Data are acquired in MATLAB R2013a (32-bit) using the Chimera VC100 current amplifier with 200 mV applied unless

DOI: 10.1021/acs.nanolett.7b03987
Nano Lett. 2018, 18, 660−668

otherwise noted, sampled at 4.166 MHz, with a hardware two-pole low-pass Bessel filter at 1 MHz cutoff frequency. Data are postfiltered for analysis at 900 kHz using a digital low-pass Bessel filter and analyzed to extract passage times and sublevel structure using both the adept2state module of MOSAIC[51,52] (https://pages.nist.gov/mosaic/) for 100 bp molecules which do not fold, and a custom implementation of the CUSUM+ algorithm[52,53] for the rest of the events (https://github.com/shadowk29/CUSUM). Both analysis programs are available freely online. Nonlinear fitting results are obtained using Origin 9.1.

■ ASSOCIATED CONTENT

Supporting Information

The Supporting Information is available free of charge on the ACS Publications website at DOI: 10.1021/acs.nanolett.7b03987.

Physical properties of nanofilters (Section S1); simulation setup (Section S2); analysis of passage time distributions (Section S3); size separation of dsDNA by mean passage time (Section S4); slower passage times in small control pores (Section S5); long passage time events (Section S6); folding distributions (Section S7) (PDF)

Water vapor swells the nanofilter, which is tented over an array of 200 nm high, 2 μm diameter columns, leaving a ring cavity around each column. Newton's colors form as water vapor is breathed over top of the structure, and are eliminated as the water evaporates in room air (AVI)

Wet nanofilter stability. A wetted nanofilter (0.7 mm × 3 mm) is exposed to repeated menisci in a microfluidic channel (AVI)

A wrinkled nanofilter is torn on meniscus. As the meniscus passes over a wrinkled nanofilter, it is torn away from the substrate and redeposited (AVI)

An illustrative simulation of an N = 200 (~3000 bp) polymer translocating through the nanofilter and eventually being captured by the sensing pore (AVI)

An animated schematic description of the fabrication and operation of the complete nanofiltered nanopore device (AVI)

■ AUTHOR INFORMATION

Corresponding Author

*E-mail: tcossa@uOttawa.ca, 613-562-5800 x6964.

ORCID

Vincent Tabard-Cossa: 0000-0003-4375-717X

Author Contributions

V.T.C. and K.B. designed the experimental study. K.B. performed nanopore experiments and wrote the first draft. K.B. and M.M. analyzed nanopore experiments. G.M. and J.L.M. developed NPN material. G.M. and K.B. developed nanofiltered pore device assembly protocols. H.W.d.H. designed the simulation study. K.K. and M.M. performed and analyzed simulations. G.M. generated schematic renders. All authors contributed to revision of the manuscript.

Funding

This work was supported in part by the Natural Sciences and Engineering Research Council of Canada (NSERC) and by the province of Ontario through their Early Researcher Award to V.T.C., by NSF PFI-BIC no. 1237699 to J.L.M., and by NIH R21EB024120 to both V.T.C. and J.L.M.

Notes

The authors declare the following competing financial interest(s): J.L.M. declares a competing financial interest as a co-founder and equity holder of SiMPore Inc., a commercial manufacturer of NPN and silicon-based membrane materials. V.T.C. and K.B. declare a competing financial interest in the form of a patent on the nanofiltered nanopore device. All other authors declare no competing financial interests.

■ ACKNOWLEDGMENTS

The authors would like to thank James Roussie and SiMPore Inc. for generous donations of expertise and NPN membrane materials. K.B. acknowledges the financial support provided by the NSERC Vanier program for postgraduate fellowships. The authors acknowledge Tucker Burgin for this work evaulating the membrane stability of fabricated nanopore devices.

■ REFERENCES

(1) Carson, S.; Wanunu, M. *Nanotechnology* **2015**, *26*, 1−14.
(2) Heerema, S. J.; Dekker, C. *Nat. Nanotechnol.* **2016**, *11*, 127−136.
(3) Dekker, C. *Nat. Nanotechnol.* **2007**, *2*, 209−215.
(4) van Dorp, S.; Keyser, U. F.; Dekker, N. H.; Dekker, C.; Lemay, S. G. *Nat. Phys.* **2009**, *5*, 347−351.
(5) Gershow, M.; Golovchenko, J. A. *Nat. Nanotechnol.* **2007**, *2*, 775−779.
(6) Lu, B.; Albertorio, F.; Hoogerheide, D. P.; Golovchenko, J. A. *Biophys. J.* **2011**, *101*, 70−79.
(7) Briggs, K.; Kwok, H.; Tabard-Cossa, V. *Small* **2014**, *10*, 2077−2086.
(8) He, Y.; Tsutsui, M.; Fan, C.; Taniguchi, M.; Kawai, T. *ACS Nano* **2011**, *5*, 5509−5518.
(9) Aksimentiev, A.; Heng, J. B.; Timp, G.; Schulten, K. *Biophys. J.* **2004**, *87*, 2086−2097.
(10) Waugh, M.; Carlsen, A.; Sean, D.; Slater, G. W.; Briggs, K.; Kwok, H.; Tabard-Cossa, V. *Electrophoresis* **2015**, *36*, 1759−1767.
(11) Squires, A. H.; Hersey, J. S.; Grinstaff, M. W.; Meller, A. *J. Am. Chem. Soc.* **2013**, *135*, 16304−16307.
(12) Kowalczyk, S. W.; Wells, D. B.; Aksimentiev, A.; Dekker, C. *Nano Lett.* **2012**, *12*, 1038−1044.
(13) Feng, J.; Liu, K.; Bulushev, R. D.; Khlybov, S.; Dumcenco, D.; Kis, A.; Radenovic, A. *Nat. Nanotechnol.* **2015**, *10*, 1070−1076.
(14) Di Fiori, N.; Squires, A.; Bar, D.; Gilboa, T.; Moustakas, T. D.; Meller, A. *Nat. Nanotechnol.* **2013**, *8*, 946.
(15) Fologea, D.; Uplinger, J.; Thomas, B.; McNabb, D. S.; Li, J. *Nano Lett.* **2005**, *5*, 1734−1737.
(16) Larkin, J.; Henley, R.; Bell, D. C.; Cohen-Karni, T.; Rosenstein, J. K.; Wanunu, M. *ACS Nano* **2013**, *7*, 10121−10128.
(17) Kwok, H.; Waugh, M.; Bustamante, J.; Briggs, K.; Tabard-Cossa, V. *Adv. Funct. Mater.* **2014**, *24*, 7745−7753.
(18) Carson, S.; Wilson, J.; Aksimentiev, A.; Wanunu, M. *Biophys. J.* **2014**, *107*, 2381−2393.
(19) Plesa, C.; van Loo, N.; Ketterer, P.; Dietz, H.; Dekker, C. *Nano Lett.* **2015**, *15*, 732−737.
(20) Bell, N. A. W.; Keyser, U. F. *Nat. Nanotechnol.* **2016**, *11*, 1−28.
(21) Bell, N. A. W.; Keyser, U. F. *arXiv* **2016**, 1−5.
(22) Vollmer, S. C.; de Haan, H. W. *J. Chem. Phys.* **2016**, *145*, 154902.
(23) Sean, D.; de Haan, H. W.; Slater, G. W. *Electrophoresis* **2015**, *36*, 682−691.
(24) Liu, X.; Skanata, M. M.; Stein, D. *Nat. Commun.* **2015**, *6*, 6222.
(25) Langecker, M.; Pedone, D.; Simmel, F. C.; Rant, U. *Nano Lett.* **2011**, *11*, 5002−5007.
(26) Harms, Z. D.; Mogensen, K. B.; Nunes, P. S.; Zhou, K.; Hildenbrand, B. W.; Mitra, I.; Tan, Z.; Zlotnick, A.; Kutter, J. P.; Jacobson, S. C. *Anal. Chem.* **2011**, *83*, 9573−9578.

DOI: 10.1021/acs.nanolett.7b03987
Nano Lett. 2018, 18, 660−668

(27) Pedone, D.; Langecker, M.; Abstreiter, G.; Rant, U. *Nano Lett.* **2011**, *11*, 1561−1567.
(28) Bell, N. A. W.; Chen, K.; Ghosal, S.; Ricci, M.; Keyser, U. F. *Nat. Commun.* **2017**, *8*, 380.
(29) DesOrmeaux, J. P. S.; Winans, J. D.; Wayson, S. E.; Gaborski, T. R.; Khire, T. S.; Striemer, C. C.; McGrath, J. L. *Nanoscale* **2014**, *6*, 10798.
(30) Gillmer, S. R.; Fang, D. Z.; Wayson, S. E.; Winans, J. D.; Abdolrahim, N.; DesOrmeaux, J.-P. S.; Getpreecharsawas, J.; Ellis, J. D.; Fauchet, P. M.; McGrath, J. L. *Thin Solid Films* **2017**, *631*, 152−160.
(31) Kavalenka, M. N.; Striemer, C. C.; Fang, D. Z.; Gaborski, T. R.; McGrath, J. L.; Fauchet, P. M. *Nanotechnology* **2012**, *23*, 145706.
(32) Kwok, H.; Briggs, K.; Tabard-Cossa, V. *PLoS One* **2014**, *9*, e92880.
(33) Briggs, K.; Kwok, H.; Tabard-Cossa, V. *Small* **2014**, *10*, 2077−2086.
(34) Briggs, K.; Charron, M.; Kwok, H.; Le, T.; Chahal, S.; Bustamante, J.; Waugh, M.; Tabard-Cossa, V. *Nanotechnology* **2015**, *26*, 084004.
(35) Slater, G. W.; Holm, C.; Chubynsky, M. V.; de Haan, H. W.; Dube, A.; Grass, K.; Hickey, O. A.; Kingsburry, C.; Sean, D.; Shendruk, T. N.; Zhan, L. *Electrophoresis* **2009**, *30*, 792−818.
(36) Mihovilovic, M.; Hagerty, N.; Stein, D. *Phys. Rev. Lett.* **2013**, *110*, 1−5.
(37) Carlsen, A. T.; Zahid, O. K.; Ruzicka, J.; Taylor, E. W.; Hall, A. R. *ACS Nano* **2014**, *8*, 4754−4760.
(38) Storm, A. J.; Chen, J. H.; Zandbergen, H. W.; Dekker, C. *Phys. Rev. E* **2005**, *71*, 51903.
(39) Storm, A. J.; Storm, C.; Chen, J.; Zandbergen, H. *Nano Lett.* **2005**, *5*, 1−5.
(40) De Haan, H. W.; Sean, D.; Slater, G. W. *Phys. Rev. E* **2015**, *91*, 1−10.
(41) Ikonen, T.; Bhattacharya, A.; Ala-Nissila, T.; Sung, W. *Phys. Rev. E* **2012**, *85*, 1−7.
(42) Teraoka, I. *Polymer Solutions: An Introduction to Physical Properties*; John Wiley & Sons, Inc, 2002.
(43) Farahpour, F.; Maleknejad, A.; Varnik, F.; Ejtehadi, M. R. *Soft Matter* **2013**, *9*, 2750.
(44) Rowghanian, P.; Grosberg, A. Y. *Phys. Rev. E* **2013**, *87*, 1−8.
(45) Morin, T. J.; Shropshire, T.; Liu, X.; Briggs, K.; Huynh, C.; Tabard-Cossa, V.; Wang, H.; Dunbar, W. B. *PLoS One* **2016**, *11*, e0154426.
(46) Singer, A.; Wanunu, M.; Morrison, W.; Kuhn, H.; Frank-kamenetskii, M.; Meller, A. *Nano Lett.* **2010**, *10*, 738−742.
(47) Atas, E.; Singer, A.; Meller, A. *Electrophoresis* **2012**, *33*, 3437−3447.
(48) Plesa, C.; Ruitenberg, J. W.; Witteveen, M. J.; Dekker, C. *Nano Lett.* **2015**, *15*, 3153−3158.
(49) van den Hout, M.; Hall, A. R.; Wu, M. Y.; Zandbergen, H. W.; Dekker, C.; Dekker, N. H. *Nanotechnology* **2010**, *21*, 115304.
(50) Rollings, R.; Graef, E.; Walsh, N.; Nandivada, S.; Benamara, M.; Li, J. *Nanotechnology* **2015**, *26*, 997−1003.
(51) Balijepalli, A.; Ettedgui, J.; Cornio, A. T.; Robertson, J. W. F.; Cheung, K. P.; Kasianowicz, J. J.; Vaz, C. *ACS Nano* **2014**, *8*, 1547−1553.
(52) Forstater, J. H.; Briggs, K.; Robertson, J. W. F.; Ettedgui, J.; Marie-Rose, O.; Vaz, C.; Kasianowicz, J. J.; Tabard-Cossa, V.; Balijepalli, A. *Anal. Chem.* **2016**, *88*, 11900−11907.
(53) Raillon, C.; Granjon, P.; Graf, M.; Steinbock, L. J.; Radenovic, A. *Nanoscale* **2012**, *4*, 4916−4924.

DOI: 10.1021/acs.nanolett.7b03987
Nano Lett. 2018, 18, 660−668

Chapter 4

Entropic Trapping of DNA with a Nanofiltered Nanopore

ACS APPLIED NANO MATERIALS
Cite This: ACS Appl. Nano Mater. XXXX, XXX, XXX−XXX
Article
www.acsanm.org

Entropic Trapping of DNA with a Nanofiltered Nanopore

Michelle H. Lam,[†] Kyle Briggs,[†] Konstantinos Kastritis,[§] Martin Magill,[§] Gregory R. Madejski,[‡] James L. McGrath,[‡] Hendrick W. de Haan,*[,§] and Vincent Tabard-Cossa*[,†]

[†]Department of Physics, University of Ottawa, Ottawa, ON K1N 6N5, Canada
[‡]Department of Biomedical Engineering, University of Rochester, Rochester, New York 14627, United States
[§]Faculty of Science, University of Ontario Institute of Technology, Oshawa, ON L1G 0C5, Canada

Supporting Information

ABSTRACT: Elucidating the kinetics of DNA passage through a solid-state nanopore is a fertile field of research, and mechanisms for controlling capture, passage, and trapping of biopolymers are likely to find numerous technological applications. Here we present a nanofiltered nanopore device which forms an entropic cage for DNA following first passage through the nanopore, trapping the translocated DNA, and permitting recapture for subsequent reanalysis and investigation of kinetics of passage under confinement. We characterize the trapping properties of this nanodevice by driving individual DNA polymers into the nanoscale gap separating the nanofilter and the pore, forming an entropic cage similar to a "two pores in series" device, leaving polymers to diffuse in the cage for various time lengths, and attempting to recapture the same molecule. We show that the cage results in effectively permanent trapping when the radius of gyration of the target polymer is significantly larger than the radii of the pores in the nanofilter. We also compare translocation dynamics as a function of translocation direction to study the effects of confinement on DNA just prior to translocation, providing further insight into the nanopore translocation process. This nanofiltered nanopore device realizes simple fabrication of a femtoliter nanoreactor in which to study fundamental biophysics and biomolecular reactions on the single-molecule level. The device provides an electrically permeable single-molecule trap with a higher entropic barrier to escape than previous attempts to fabricate similar structures.

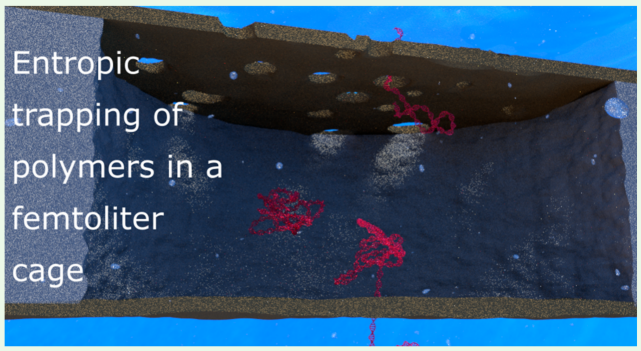

KEYWORDS: *nanopore, nanotechnology, nanofabrication, DNA, entropy, nanoconfinement, nanoporous membrane*

INTRODUCTION

Nanopores allow for highly sensitive electrical detection of single biomolecules,[1] and many applications have gained attention in recent years. Among them are DNA sequencing,[2,3] investigating single biomolecular reactions,[4] identifying particular sequences of DNA through the use of barcodes,[5] and elucidating fundamental physics of polymers and their transport through pores at the single-molecule level,[6−9] which is intrinsic to many processes of life.[10−13]

The study of confinement effects on DNA prior to translocation through a nanoscale pore has been undertaken before to examine the drift-diffusion model under various levels of confinement[14,15] compared to free solution,[8] the passage time dependence on DNA conformation,[7] and the trapping of DNA in entropic cages.[16] While a handful of studies have explored single-molecule entropic trapping with nanopores,[16] the potential escape routes are generally quite large compared to relevant target polymers for biomedical applications, and as we will demonstrate, entropy-based traps quickly lose their efficiency as polymer length decreases. The ability to trap relatively short polymers would be very useful. For example, M13 (~7000 bp, radius of gyration 150 nm, contour length 2500 nm) is of great interest as a scaffold for the assembly of DNA origami nanostructures[17−19] or as a barcoding nanocarrier for biosensing applications.[20−24] In order for the trap to apply a confining effect to the molecule of interest, the largest linear dimension of the escape routes in the trap (the major axis of the pores) must be small compared to the free solution radius of gyration of the polymer. This condition is not possible to realize for short polymers by using previously reported trap configurations and fabrication approaches.

In addition to entropic traps, several other polymer trapping methods have been explored. The use of plasmonic nanostructures has been proposed and validated in simulation, in which near-field excitation of a plasmonic structure is used to apply optical forces directly to DNA.[25,26] Trapping of long polymers has been demonstrated experimentally using a two-pore system, in which the DNA molecule is caught and stretched between two competing nanopores.[27,28] Using

Received: April 2, 2019
Accepted: June 19, 2019
Published: June 19, 2019

DOI: 10.1021/acsanm.9b00606
ACS Appl. Nano Mater. XXXX, XXX, XXX−XXX

nanopores smaller in diameter than DNA has also been shown to enable long passage times and temporary trapping of polymers.[29,30] Finally, dielectrophoresis has been used to trap and concentrate DNA prior to interrogation with a nanopore.[31]

In this work, we propose the use of ultrathin nanoporous silicon nitride[7,32] (NPN) membranes as a capping nanofilter layer for a confining well above a nanopore to entropically confine polymers for long times. This allows us to considerably improve on the trapping efficiency, since the reduced size of escape routes in the nanofilter layer provides a higher entropic barrier to escape than previously reported trap architectures.

Briggs et al. previously reported integration of NPN nanofilter membranes upstream of nanopore sensors to affect translocation kinetics.[7] Here, we present the use of these nanofiltered nanopore devices in reverse configuration as an entropic nanocage.

EXPERIMENTAL SECTION

Device Geometry. The entropic trapping device employed in this work consists of a SiN_x membrane separated from a nanoporous nitride membrane (a nanofilter) by a SiO_2 spacer containing a hexagonal grid of microwells with a diameter of ~4.5 μm. The assembly and construction of the nanofiltered nanopore device are described in full elsewhere and are schematically illustrated in Figure 1,[7] utilizing a water-vapor delamination approach to attach a nanofilter over a substrate patterned with a spacer layer. Devices are either ozone cleaned for 15 min or plasma cleaned at 20 W for 20 s before assembly. The same cleaning procedure is repeated again before painting with PDMS to reduce device capacitance. The cavity between the two membranes is wetted by evacuating the device before immersion in ethanol. After immersion, the vacuum is slowly broken, pulling ethanol into the cavity. The device is immersed in water to replace the ethanol by diffusion and mounted in a custom 3D-printed flow cell.

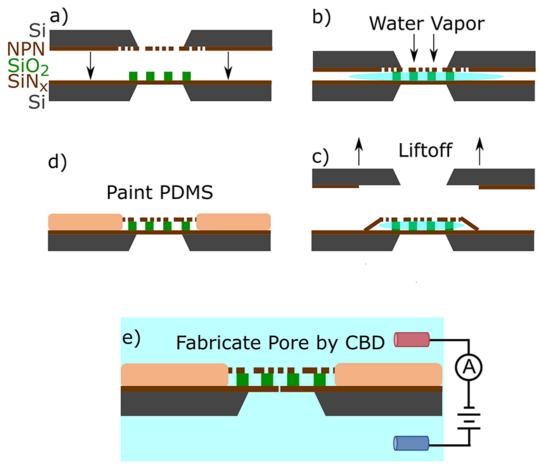

Figure 1. A schematic illustrating of the assembly of the entropic trap. (a) Two chips containing an intact 20 nm thick SiN_x sensing membrane decorated with an 800 nm SiO_2 spacer containing a hexagonal grid of 4.5 μm microwells is brought into close proximity with a NPN membrane. (b) Water vapor floods the cavity and provides a weak adhesion force between the two membranes. (c) The NPN support chip is lifted off, leaving behind the NPN layer capping the trapping cavities. (d) Polydimethylsiloxane (PDMS) is painted around dual membrane stack and over some of the interface to reduce device capacitance and permanently bond the two membranes. (e) A nanopore is formed in one of the cavities at random by using controlled breakdown.

The particular geometry used here consists of an 800 nm separation between a 50 nm thick nanofilter membrane (i.e., the nanofilter) and a 20 nm thick silicon nitride (SiN_x) membrane (i.e., the membrane which will containing the sensing pore), as depicted in Figure 2a. The two membranes are separated by a SiO_2 spacer containing a hexagonal grid of microwells with diameter of 4.5 μm, resulting in a 13 fL cavity. A nanopore is randomly fabricated[33] in one of the microwells by using controlled breakdown (CBD).[7,34] We refer to this single pore made by CBD as the sensing pore, since the electrical signal we measure experimentally is sensitive only to this pore. The average porosity of the nanofilter membranes is 19.1%, measured by dividing the total open pore area to the total membrane area, as measured by images such as that shown in Figure 2b. The average effective nanofilter pore diameter ranges from 24 to 31 nm, varying over the area of the nanofilter membrane, with a standard deviation of 9 nm, measured by fitting an ellipse with axis lengths a and b to each identified pore and reporting the effective radius as $r = \sqrt{ab}$. The approximate number density of pores is 312 pores/μm^2, estimated by directly counting pores identified in TEM images. Of particular interest to the performance of these devices as entropic traps for linear polymers is the major axis distribution of pores in the nanofilter, which is plotted in Figure 2c.

Because of the manufacturing process, the nanofilter is prone to variability in the pore layouts, which are effectively randomly distributed on the membrane. One of the more striking features in Figure 2b is clustering of pores, which can sometimes result in merged pores. Merged pores are usually much longer in one of their dimensions, forming a quasi-elliptic, rather than circular, cross section. Further work on the flow through these fringe geometries was performed by Madejski et al.[35]

It is clear from Figure 2c that the distribution of pore sizes when measured by major axis length is bimodal. The first peak in the distribution corresponds to standard nanopores present on the nanofilter. The second, much smaller peak represents pores that have partially merged together to make a single pore that is much longer in one of its dimensions, which we will demonstrate has important implications for the performance of the entropic trap.

Sensing Pore Fabrication. Nanopores are fabricated using CBD, described in detail in our previous work.[30,33,36] Nanopore fabrication is performed in 2 M KCl at pH 8 by using a gradual voltage increase up to 15 V. Some membranes took several hours longer to fabricate than expected given the membrane properties, most likely due to partial wetting of the cavity between the membranes.[7] After the pore is formed, KCl is replaced with 3.6 M LiCl[37] at pH 8, and the pore is grown to the desired pore size (6−15 nm) by applying 4 s square voltage pulses (4−5 V). Both salt solutions are buffered to pH 8 with 10 mM HEPES. Some pores were left immersed in salt solution to stabilize before DNA experiments, if the IV and noise properties were not optimal immediately following the growing stage.[30]

Simulation Setup. Simulations of the diffusive mode of operation were conducted to better understand the behavior of 1.2 kbp dsDNA. We used an effective multiscale approach to model the system. For the bulk of the device cavity, the DNA molecules were modeled as particles representing the center of mass (COM). The diffusion of these effective particles was simulated by using Brownian dynamics (BD). As the dynamics of the entire chain become important near the nanofilter, we conducted separate simulations where we modeled the DNA as a wormlike chain and used coarse-grained Langevin dynamics (CGLD)[38] to simulate its motion. The CGLD simulations were used to estimate the probability that a polymer located close to a filter pore will successfully cross the membrane rather than diffusing back into the bulk of the device. These success probabilities were used to couple the BD and the CGLD simulations via a special boundary condition for the nanofilter in the BD simulations. Further details for the simulations are presented in the Supporting Information section S1.

Data Acquisition and Analysis. DNA samples (NoLimits individual DNA fragments from Thermo Fisher Scientific) were mixed in 3.6 M LiCl pH 8 to desired DNA concentration (2−5 nM) for translocation experiments. DNA molecules are manipulated by using ±200 mV biases.

DOI: 10.1021/acsanm.9b00606
ACS Appl. Nano Mater. XXXX, XXX, XXX−XXX

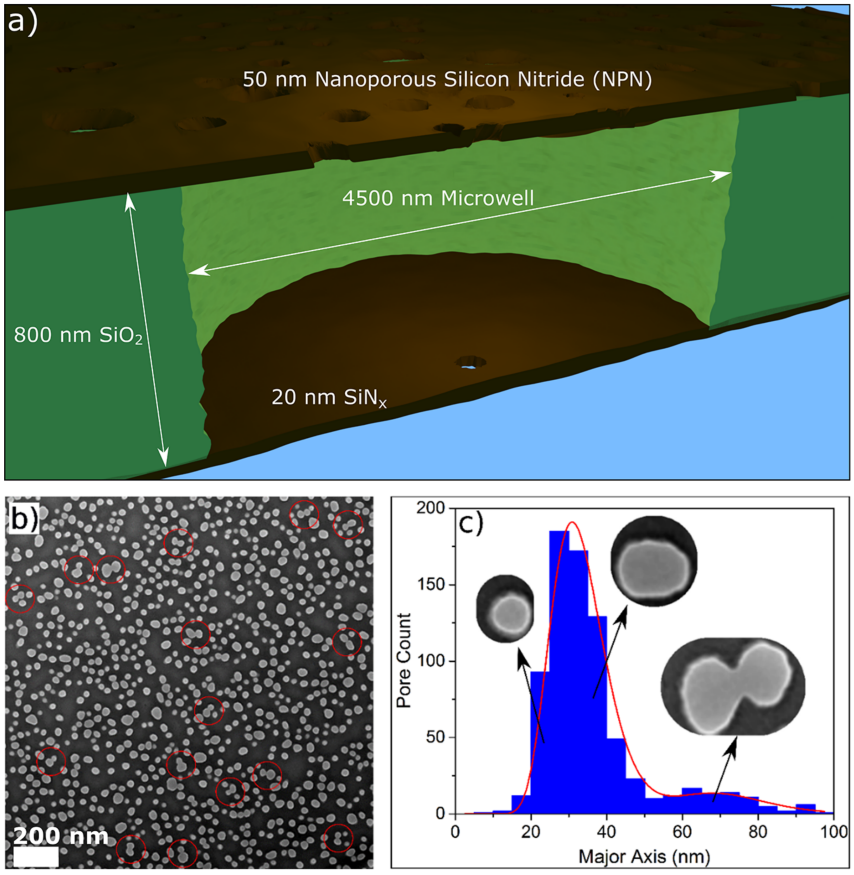

Figure 2. (a) Schematic of a cross section of a single microwell in the device geometry, not to scale. The 50 nm thick NPN nanofilter, containing pores with an average diameter of 31 ± 9 nm, is separated from a 20 nm thick SiN_x membrane by an 800 nm SiO_2 spacer containing an array of 4500 nm diameter wells, one of which contains the sensing pore. (b) SEM image of the nanofilter membrane, showing a random distribution of pores. The scale bar is 200 nm. Note that in several places, indicated with red circles, neighboring pores overlap, resulting in a single large oblong merged pore. (c) Distribution of pore sizes as measured by their major axis (not average diameter, which is plotted in the Supporting Information section S2). The data are well fit by two log-normal distributions. The corresponding representative pores in the insets are taken from (b).

Custom LabVIEW software, interfaced with a National Instruments DAQ card (USB-6353), is used to acquire data during DNA translocation experiments. This software was further used to automate the recapture experiments. The automation module was designed to change the applied voltage upon detecting a complete translocation event. A positive voltage (200 mV) is applied to capture a DNA molecule, with the sensing pore side of the device grounded. Upon detection of a translocation event the software terminates the applied voltage for the required time delay and then applies −200 mV to attempt to recapture the DNA molecule, waiting up to 5 min before declaring an event to be lost. The feedback loop for voltage changes was closed in software every millisecond, resulting in an effective response time of a few milliseconds. The Axopatch 200B is used to amplify the current signal by using a sampling frequency of 500 kHz or 1 MHz and hardware low-pass filtered at 100 kHz.

Analysis and fitting of DNA translocation events through the sensing pore are performed by using a custom implementation of the CUSUM algorithm,[39,40] which is freely available online (https://github.com/shadowk29/CUSUM). Origin is used for nonlinear fitting and data presentation.

■ RESULTS AND DISCUSSION

There are two modes of operation used with this device: *diffusive trapping*, in which no external force is applied to drive the escape of the polymer out of the cage, and *driven trapping*, in which the capture voltage is maintained for a given time while many molecules are loaded into the cavity before the field is reversed and recapture is attempted.

Diffusive Trapping. We first present results in the diffusive trapping mode. To compare kinetics of DNA passage into and out of the confining space between the membranes, we introduce double-stranded DNA (dsDNA) to the sensing pore side of the device, ranging from 1.2 to 10 kbp in length. In this configuration, a single DNA molecule is captured into the entropic cage through the sensing pore (loading step, Figure 3a), and the voltage bias is immediately (within ∼1 ms) turned off and maintained at zero for various delay times Δt_0 (diffusion step, Figure 3b). The voltage is then reversed to drive the DNA molecule back out through the sensing pore (recapture step, Figure 3c). Once the voltage bias is reversed to attempt to recapture, it is maintained until an event is detected or 5 min passes without a recapture event. For 10 kbp polymers, this wait time is increased to 10 min to account for the slower diffusive dynamics.

An example of a typical resulting current trace is given in Figure 3d. To fully understand the kinetics of DNA in the trap, we also performed simulations of diffusive escape of DNA through the nanofilter, which are detailed in the Experimental Section. The resulting experimental and simulation data are presented and compared in Figure 3e.

In the diffusive trapping mode, sufficiently large polymers remained trapped for all delay times tested. Figure 3e shows

DOI: 10.1021/acsanm.9b00606
ACS Appl. Nano Mater. XXXX, XXX, XXX−XXX

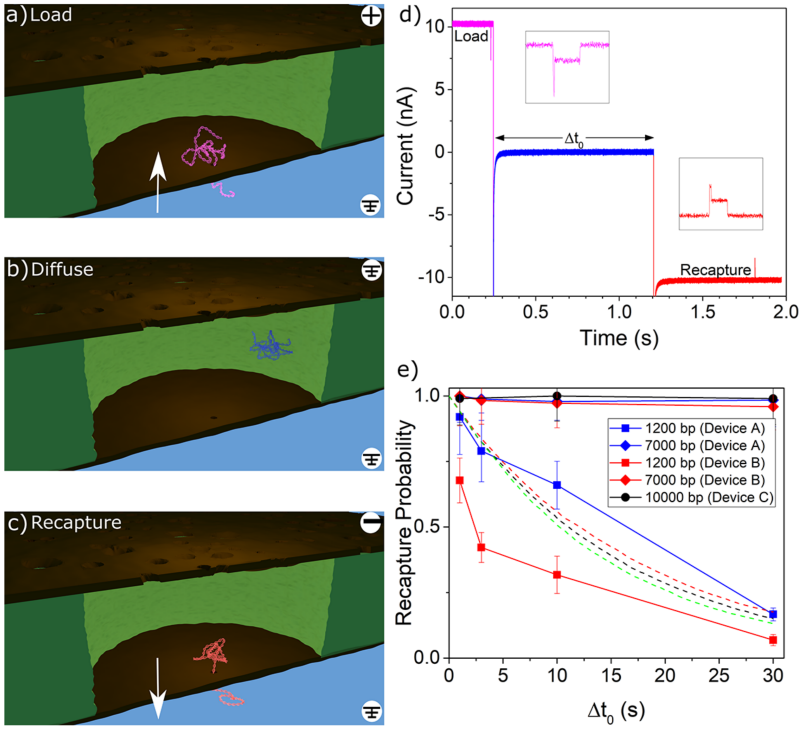

Figure 3. Diffusive trapping mode. (a) DNA is captured by the sensing pore and pulled upward into the cavity in between the two membranes. (b) In the diffusive trapping mode, immediately following capture, the field is turned off, and the captured DNA is allowed to freely diffuse around the cavity under no applied voltage. (c) The voltage is reversed, and the DNA, if still trapped in the cavity, is recaptured by the sensing pore. Renders are for conceptual illustration only; geometry and DNA are not to scale. (d) A representative current trace showing a single capture−recapture event in the diffusive trapping mode, with a 1 s delay. Additional events are shown in the Supporting Information section S3. (e) Experimental recapture probability trends for varying delay times in the diffusive trapping mode (solid lines). Three different devices (indicated by marker color) were used for these diffusive experiments. Squares correspond to 1.2 kbp, diamonds to 7 kbp, and circles to 10 kbp. The sensing pores had diameters of 9.5 nm (device A: 577 loading events for 1.2 kbp, 727 loading events for 7 kbp), 7.5 nm (device B: 430 loading events for 1.2 kbp, 426 loading events for 7 kbp), and 11.5 nm (device C: 305 loading events for 10 kbp). Dashed lines show simulation results for 1.2 kbp DNA in devices whose filters contained 40, 75, and 160 nanofilter pores with diameters of 90 nm (green), 80 nm (red), and 70 nm (black), respectively. Error bars are estimated by using simple Poisson statistics.

data for the recapture probabilities of 7 and 10 kbp dsDNA, with blob size of ∼150 and ∼180 nm, respectively. It essentially remains at 1 (i.e., always recapturing the trapped polymer) for all Δt_0 tested, up to 30 s. From our simulations we estimate the half-life for escape from the trap to be on the order of hours. This trapping efficiency is a remarkable feature of these nanofiltered nanopore devices, since a translocating polymer is otherwise lost to the bulk reservoir if the field is not inverted within milliseconds following its passage. Indeed, Gershow et al.[8] showed that the majority of 4 and 6 kbp molecules diffuse out of recapture range within just a few tens of milliseconds when no trapping force is present to keep them in the vicinity of the sensing pore, consistent with our own control experiments. The trapping efficiency achieved here is also improved compared to a previous attempt by Liu et al.[16] to fabricate entropic cages for DNA, for which the pore opening of the cavity provided a large escape route, such that it would always be possible for short polymers to escape via diffusion. This limited efficient trapping to long DNA strands (λ DNA, 48.3 kbp, $L_c \approx 16.4$ μm, $R_g \approx 400$ nm).

In contrast, in the nanofiltered nanopore device the radius of gyration of the polymer significantly exceeds the size of the nanopores in the nanoporous membrane, and thus the entropic cost of passage through the filter is non-negligible. DNA is therefore unlikely to escape by diffusion alone. Thus, sufficiently large polymers can remain trapped for quite a long time.

Our simulations show that the probability of a DNA strand crossing a filter pore becomes very small as the pore radius decreases. Figure 4c shows the success probability for a polymer corresponding to 1.2 kbp DNA as a function of filter pore diameter. For pores smaller than 120 nm the success probability follows a strong power law behavior (with an exponent of ∼4.45). For pore diameters below 60 nm, successful translocations were rare. Whereas most simulations in Figure 4c were repeated until 200 successful crossings were observed, simulations for the two smallest pore sizes were repeated until a prescribed number of failed events had occurred. After 10000 failed events, only four translocations were observed for a filter pore diameter of 50 nm and only two at 40 nm. Conversely, for large pore diameters exceeding 120 nm, the success probability begins to saturate as the polymer no longer experiences appreciable deformation in crossing the filter. Note that the saturation value, at ∼23%, is a consequence of our simulation methodology. The success probability is defined as the probability for a polymer located close to a filter pore to translocate before diffusing a significant distance away; this differs from the translocation probability as defined in other work.[41]

The simulation results suggest that only a small fraction of the filter pores contribute appreciably to the leakage of 1.2 kbp

DOI: 10.1021/acsanm.9b00606
ACS Appl. Nano Mater. XXXX, XXX, XXX−XXX

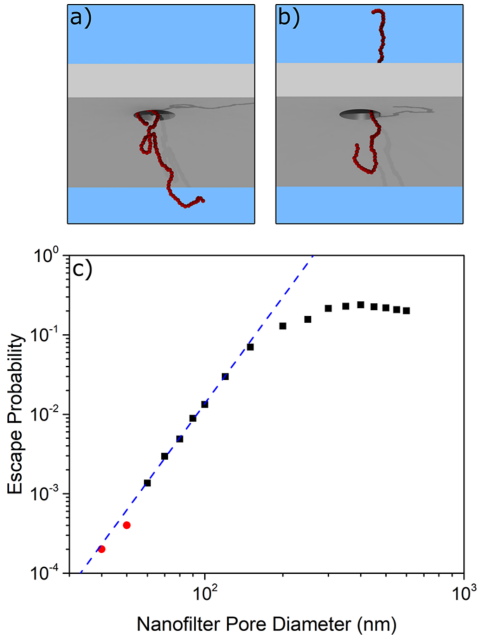

Figure 4. (a) A snapshot of a 1.2 kbp (with $R_g \sim 55$ nm) equivalent DNA polymer during a simulated escape attempt by diffusion through the nanofilter. (b) The same polymer at a later moment in time as it crosses the membrane. (c) The simulated probability that the polymer will successfully cross the membrane before diffusing away from the filter.

DNA observed in Figure 3e. The distribution of pore major axis lengths can be seen in Figure 2c. The largest peak in the distribution corresponds to single filter pores, and it is clear from the distribution that single filter pores rarely exceed a major axis length of 50 nm. As shown Figure 4c, simulations suggest that minimal escape is expected through these filter pores.

However, the pore size distribution in Figure 2c is bimodal, and there is a separate population of pores with much larger sizes. These are merged pores, and although they are relatively rare, they have a significant impact on the trapping efficiency. From Figure 2c the average pore size of the secondary population is around 80 nm, and as per Figure 4c, we expect leaking through these pores to be non-negligible for 1.2 kbp DNA. For the devices used in this work, ~10 ± 1% of nanofilter pores have a major axis length in the secondary population, and it is through these merged pores that we can explain the escape of the smaller polymer. This explanation also gives insight into the origin of the differences in trapping efficiency for the two different 1.2 kbp polymer experiments, which most likely arises from differences in the details of the nanofilter pore size distributions—especially the merged pores. This implies that the trapping efficiency of any particular device is dominated by the number and size of merged pores in the nanofilter pore size distribution for that device, a property that can be tuned at the manufacturing level by changing the porosity and average pore size.

To gain quantitative insight into the relationship between the leaking rate and the number of filter pores and their size, simulations were performed in which the number and size of the nanofilter nanopores were varied. The results are included as dashed lines in Figure 3e. The simulation data clearly show that a small number of large merged pores (e.g., 40 pores of diameter 90 nm) can give rise to the same escape probability as a larger number of smaller pores (e.g., 160 pores of diameter 70 nm). In addition, good agreement with experimental results was found for these different combinations, validating this physical picture. There are some discrepancies in the shape of the curves, but these most likely arise from the assumptions of constant nanofilter pore size and uniform shape.

Whereas over 80% of the 1.2 kbp DNA strands escaped from the device in 20−30 s, the larger molecules exhibited virtually no leakage over the same time scale. Simulations (included in the Supporting Information section S1) indicate that for fixed filter pore sizes the overall escape time from the device grows very rapidly with chain length. From these simulations we estimate that the half-life for 7 kbp DNA to escape from the device exceeds half an hour, and that for 10 kbp DNA is on the order of hours.

Driven Trapping. In the driven trapping mode of operation, the order of events is the same, but we maintain the 200 mV capture voltage even as molecules are captured, driving new molecules through the sensing pore and into the gap between membranes while previously translocated ones are still in the cage. The experimental sequence is depicted schematically in Figure 5a−c. In this mode, previously trapped molecules have the ability to escape through the nanofilter under the weak driving force present there (~10 μV, estimated by considering the relative resistances of NPN material over a single microwell as compared to the sensing pore resistance). While this force is not enough to significantly change the escape probability during any one attempt, the additional driving force does increase the rate at which escape attempts are made. Figure 5d shows a time series of the nanopore current just before and just after the voltage change for a particular driven trapping experiment, showing multiple recapture events as soon as the voltage polarity is flipped. After a loading time Δt_1, the voltage is reversed, and any molecules still in the gap are recaptured and counted. Typically, a few tens to a few hundred events were recaptured before the cavity was depleted, depending on the loading duration. The recapturing voltage is maintained until no event is detected for 5 min, or 10 min in the case of polymers 10 kbp or longer.

During driven trapping experiments, we usually observed nonzero recapture probabilities for various loading durations Δt_1, as shown in Figure 5e. Note that the recapture probability defined in the driven trapping case is conceptually different from the diffusive case. While it is still calculated as the ratio of molecules entering the cavity to molecules leaving it, because DNA molecules that enter early in the capture step have more time to attempt escape, this quantity no longer represents the probability that any given molecule remains trapped. We find that the recapture probability decreases as the loading duration increases, eventually leveling off at long delays as an equilibrium is established between the rate of capture by the sensing pore and the rate of escape through the nanofilter. The exact value at which this equilibrium is reached varies significantly between devices, being dependent on both the sensing pore size and the details of the nanofilter pore distribution, in terms of both physical size and spatial distribution in relation to the sensing pore. In comparison, the control experiments (black inverted triangles), consisting of devices with a standard pore without a nanofilter, yielded virtually zero recapture probability, since the electric field quickly pushes DNA out of the capture region and into free solution in the absence of the nanofilter.[8] While it is clear that

DOI: 10.1021/acsanm.9b00606
ACS Appl. Nano Mater. XXXX, XXX, XXX−XXX

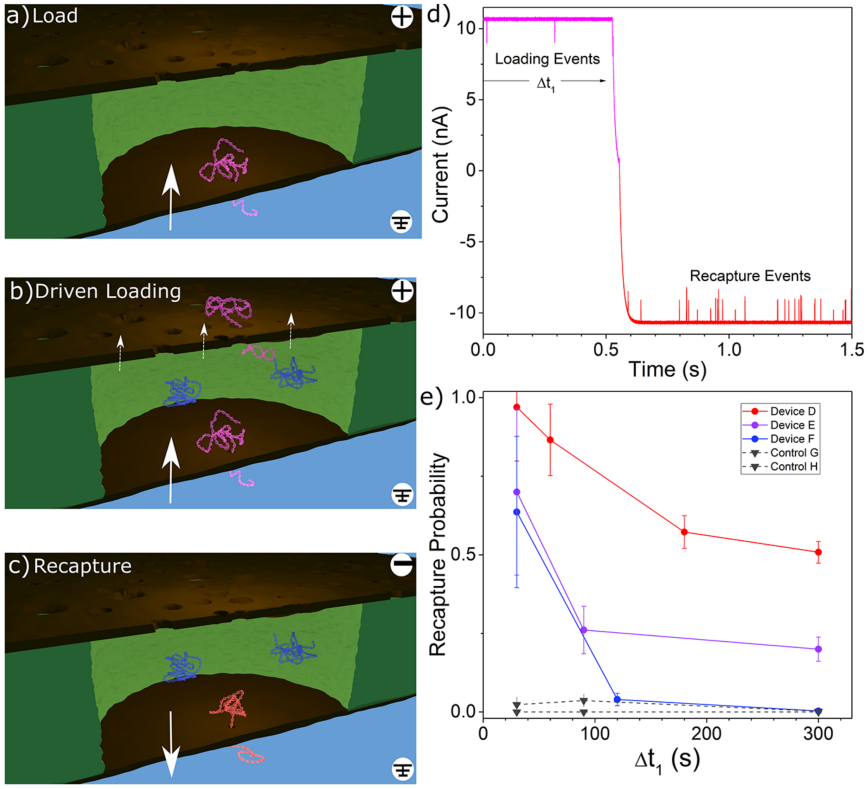

Figure 5. (a) DNA is captured by the sensing pore and pulled into the cavity in between the two membranes. (b) In the "driven trapping" mode, other DNA molecules can continue to be captured into the cavity though the sensing pore and can also escape through the nanofilter under the influence an applied voltage. (c) The voltage is reversed and any DNA trapped in the cavity is recaptured by the sensing pore. Renders are for conceptual illustration only; geometry and DNA are not to scale. (d) A representative current trace showing the transitional region of a driven trapping experiment for an applied voltage of ±200 mV for device D. (e) Recapture probability for increasing loading durations in the driven trapping configuration. The 7 kbp dsDNA was used for all driven trapping experiments. Three nanofiltered nanopores (circles) and two standard control nanopores (inverted triangles) were used. In alphabetical order, sensing pores had diameters of 10.0 nm (736 loading events), 7.8 nm (90 loading events), 8.1 nm (410 loading events), 7.9 nm (790 loading events), and 8.6 nm (577 loading events). Error bars are estimated by using simple Poisson statistics.

DNA is readily able to traverse the nanofilter as long as a bias is applied, the fact that there is a significant number of DNA recaptured suggests that the presence of the nanofilter presents a barrier which slows DNA in transit before escape, similar in principle to reptation through a gel medium.

For the three nanofiltered nanopore devices used in Figure 5, we also compared capture rates in the three possible translocation configurations: loading through the sensing pore (Figure 5a,b), recapture from the entropic cage by the sensing pore (Figure 5c), and capture through the nanofilter (as shown in previous work[7]).

Because of the confining geometry of the entropic cage, molecules in the gap take relatively little time to find the sensing pore once the recapture voltage is established. If a large number of molecules are trapped in the cage, one would expect this to manifest itself as a high capture rate at the very beginning of the recapture process. We observed significant variation between the behaviors of different devices in the driven trapping mode. Figure 6 illustrates the two extremes of this behavior range. In Figure 6a, we see that in device D the initial capture rate in the recapture step is very high compared to both other translocation modes (also illustrated in Figure 5d), indicating that this device is a strong entropic trap which locally increases the concentration of trapped dsDNA in the gap as compared to the bulk. We also observe a very low capture rate through the nanofilter for this device, consistent with the idea that the nanofilter presents a strong entropic barrier to translocation in this case. At the other extreme, device F (Figure 6b) has essentially the same capture rate through the nanofilter as it does through the sensing pore during the loading step and shows hardly any recapture, consistent with the idea that the nanofilter is not a strong entropic barrier in this device. Device E falls in between these two extremes.

A low amplification of the recapture rate as compared to the loading rate indicates a device with inefficient trapping properties, with a nanofilter that presents only a weak barrier to escape the cage. Devices that are poor traps (low recapture rate) have a rate of capture through the nanofilter comparable to the loading rate through the sensing pore, while devices with initially higher recapture rate as compared to the loading rate are indicative of a strongly trapping device and are associated with low rates of capture through the nanofilter. These observations further highlight and support our previous observations that the variation between devices must come from the inherent variability in the local properties of the nanofilter pore distribution for any particular device.[7]

Translocation Kinetics. We finally compare the translocation kinetics of these three modes using 1.2, 7, and 10 kbp dsDNA. Figure 7 shows passage time histograms for all three modes of capture with these lengths of dsDNA. Consistent with our previous work,[7] the passage time distributions are well

DOI: 10.1021/acsanm.9b00606
ACS Appl. Nano Mater. XXXX, XXX, XXX−XXX

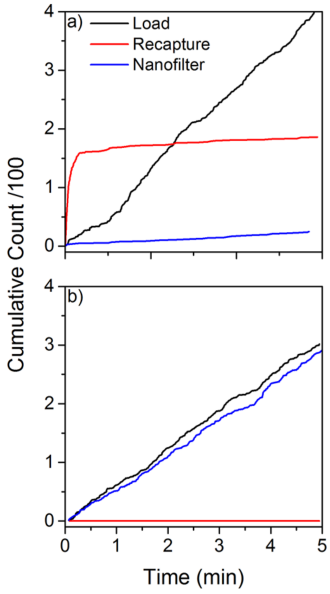

Figure 6. Cumulative event counts in the three translocation modes (load/back: capture by the sensing pore into the cavity; recapture/red: capture by the sensing pore from the cavity; nanofilter/blue: capture by the sensing pore through the nanofilter) for two devices during 5 min loading experiments in the driven trapping mode at 200 mV, showing the extremes of the possible trapping behaviors with 7 kbp dsDNA. (a) Cumulative event counts for device D, which is a very efficient trap. (b) Cumulative event counts for device F, which is not an efficient trap.

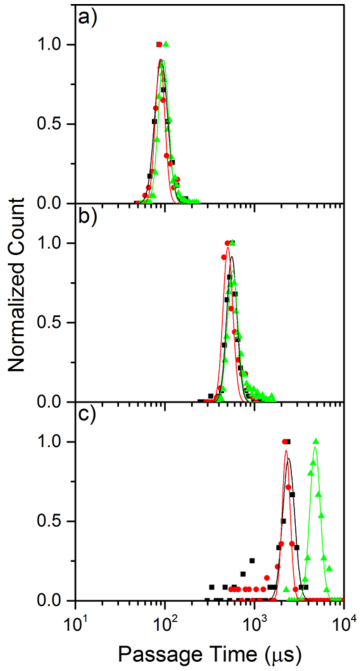

Figure 7. Passage times for loading (black squares), recapture (red circles), and nanofilter capture (green triangles) experiments. (a) Histograms of passage times of the three capture modes for 1.2 kbp dsDNA capture by a 6.9 nm diameter sensing pore (240 loading events, 89 recapture events, and 4549 nanofilter events). (b) Corresponding histograms of passage times for 7 kbp dsDNA using the same pore as (a) (139 loading events, 139 recapture events, and 1276 nanofilter events). (c) Corresponding histograms of passage times for 10 kbp dsDNA using a 7.2 nm diameter sensing pore (90 loading events, 88 recapture events, and 78 nanofilter events). Only passage times for unfolded, single-level translocation events are included. All experiments are performed in 3.6 M LiCl pH 8 at 200 mV.

characterized by a log-normal distribution for the unfolded DNA events. As can be seen in Figure 7a,b, using 1.2 and 7 kbp dsDNA, the passage time histograms are indistinguishable for all three possible translocation modes, having a mean and standard deviation of 93 ± 17 μs and 547 ± 62 μs, respectively. For the 10 kbp molecules presented in Figure 7c, however, passage through the nanofilter first results in much longer passage times than the other modes, yielding translocation times of 4770 ± 640 μs for nanofilter capture as compared to 2370 ± 360 μs for passage through the sensing pore alone in either direction.

While one might expect that confinement of dsDNA in the cage should lead to different passage kinetics depending on the direction of passage,[5] the degree of confinement achieved here was most likely not sufficient to observe this effect. Because the radii of gyration of all polymers used (55, 151, and 181 nm) were smaller than the gap height (800 nm), this is probably not surprising. The only significant difference in translocation kinetics was observed for capture through the nanofilter for the longest polymers, 10 kbp dsDNA, which is likely due to increased interaction between the polymer and the nanofilter than a result of confinement effects.[7]

Of particular note is that the large gap heights between the membranes used in this work, which permit passage of much longer polymers than previously reported,[7] extending the range of polymers lengths that can be reliably captured through the nanofilter without clogging. However, because of the additional relaxation of the polymer as it traverses the increased gap height compared to our previous work, the improvement to passage time distribution width is small.

■ CONCLUSIONS

We have presented the application of NPN as a nanofilter within molecular distances from a sensing nanopore, forming a nanofiltered nanopore device as a means to confine and entropically trap single linear dsDNA molecules in a femtoliter cage for extended periods of time. With this structure, we can study the kinetics of DNA translocation in the presence of an entropic barrier to escape from a confining cavity. Through both experiment and simulation we have shown that while the efficiency of NPN as a trapping layer for short polymers is dependent on the details of the local nanofilter pore size distribution, it can be used to trap linear polymers for experimentally relevant time scales. We have also demonstrated that devices with a larger gap height can reliably be used to study longer polymers than previously reported without clogging the sensing pore.

The understanding that the trapping efficiency of the nanodevice is dictated by the outliers in the nanofilter pore size distribution will be of vital importance in guiding the design of similar devices in the future. As shown in our previous work, atomic layer deposition can be used to shrink pores in the nanofilter and separate merged pores, allowing confinement of even smaller polymers than those presented here. Using the NPN membrane as a capping layer for the cage allows for free flow of ions, small biomolecules, and biochemical reagents into the cage[32] while providing an

DOI: 10.1021/acsanm.9b00606
ACS Appl. Nano Mater. XXXX, XXX, XXX−XXX

entropic force to indefinitely confine DNA. The device presented here improves dramatically on previous attempts to trap[16] and recapture[8] polymers, decreasing the pore diameter of escape route by a factor of 10 while also decreasing the electrical resistance of the capping layer, improving the trapping efficiency.

■ ASSOCIATED CONTENT

Supporting Information

The Supporting Information is available free of charge on the ACS Publications website at DOI: 10.1021/acsanm.9b00606.

Section S1: simulation setup; section S2: effective pore diameter distribution; section S3: additional event traces (PDF)

■ AUTHOR INFORMATION

Corresponding Authors

*(V.T.-C.) E-mail tcossa@uOttawa.ca.
*(H.d.H.) E-mail Hendrick.deHaan@uoit.ca.

ORCID

Vincent Tabard-Cossa: 0000-0003-4375-717X

Author Contributions

M.H.L., K.B., and K.K. contributed equally to this work. K.B. assembled the devices. M.H.L. performed the experiments. K.B. and M.H.L. analyzed the experiments. K.K., M.M., and G.R.M. analyzed the pore distributions. K.B. and V.T.C. designed the experimental study. K.K., M.M., and H.d.H. performed and analyzed the simulations. H.d.H. designed the simulation study. K.B., G.R.M., V.T.C., and J.L.M. designed the experimental protocols. M.H.L. and K.B. wrote the first draft. All authors edited the final version of the manuscript.

Notes

The authors declare the following competing financial interest(s): K.B., G.R.M., J.L.M., and V.T.C. declare competing financial interest in the form of a patent on the nanofiltered nanopore device. J.L.M. is a cofounder of SiMPore Inc. All other authors declare no competing financial interest.

■ ACKNOWLEDGMENTS

The authors acknowledge the R21 NIH grant R21EB024120 to V.T.C. and J.L.M. for financial support, the Natural Sciences and Engineering Research Council of Canada (NSERC) grant CRDPJ 530554-18 to V.T.C. and H.d.H., and Discovery Grant 2014-06091 to H.d.H. K.B. acknowledges the financial support of the Vanier Canadian Graduate Scholarship program. V.T.C. thanks the Province of Ontario for an Early Researcher Award. The authors acknowledge SiMPore Inc. for their expertise in designing the nanofiltered nanopore devices.

■ REFERENCES

(1) Fologea, D.; Gershow, M.; Ledden, B.; McNabb, D. S.; Golovchenko, J. A.; Li, J. Detecting Single Stranded DNA with a Solid State Nanopore. *Nano Lett.* **2005**, *5* (10), 1905−1909.

(2) Derrington, I. M.; Butler, T. Z.; Collins, M. D.; Manrao, E.; Pavlenok, M.; Niederweis, M.; Gundlach, J. H. Nanopore DNA Sequencing with MspA. *Proc. Natl. Acad. Sci. U. S. A.* **2010**, *107* (37), 16060−16065.

(3) Clarke, J.; Wu, H.-C.; Jayasinghe, L.; Patel, A.; Reid, S.; Bayley, H. Continuous Base Identification for Single-Molecule Nanopore DNA Sequencing. *Nat. Nanotechnol.* **2009**, *4* (4), 265−270.

(4) Mathé, J.; Visram, H.; Viasnoff, V.; Rabin, Y.; Meller, A. Nanopore Unzipping of Individual DNA Hairpin Molecules. *Biophys. J.* **2004**, *87* (5), 3205−3212.

(5) Bell, N. A. W.; Chen, K.; Ghosal, S.; Ricci, M.; Keyser, U. F. Asymmetric Dynamics of DNA Entering and Exiting a Strongly Confining Nanopore. *Nat. Commun.* **2017**, *8* (1), 380.

(6) Oukhaled, G.; Mathé, J.; Biance, a.-L.; Bacri, L.; Betton, J.-M.; Lairez, D.; Pelta, J.; Auvray, L. Unfolding of Proteins and Long Transient Conformations Detected by Single Nanopore Recording. *Phys. Rev. Lett.* **2007**, *98* (15), 98−101.

(7) Briggs, K.; Madejski, G.; Magill, M.; Kastritis, K.; De Haan, H. W. H. W.; McGrath, J. L. J. L.; Tabard-Cossa, V. DNA Translocations through Nanopores under Nanoscale Preconfinement. *Nano Lett.* **2018**, *18* (2), 660−668.

(8) Gershow, M.; Golovchenko, J. A. Recapturing and Trapping Single Molecules with a Solid-State Nanopore. *Nat. Nanotechnol.* **2007**, *2* (12), 775−779.

(9) Sean, D.; de Haan, H. W.; Slater, G. W. Translocation of a Polymer through a Nanopore Starting from a Confining Nanotube. *Electrophoresis* **2015**, *36* (5), 682−691.

(10) Peters, R. Functionalization of a Nanopore: The Nuclear Pore Complex Paradigm. *Biochim. Biophys. Acta - Mol. Cell Res.* **2009**, *1793* (10), 1533−1539.

(11) Nies, P.; Van; Kowalczyk, S. W.; Kapinos, L.; Blosser, T. R.; Lim, R. Y. H.; Dekker, C.; Magalhães, T.; van Nies, P.; Lim, R. Y. H.; Dekker, C. Single-Molecule Transport across an Individual Biomimetic Nuclear Pore Complex. *Nat. Nanotechnol.* **2011**, *6* (7), 433−438.

(12) Tamura, K.; Hara-Nishimura, I. The Molecular Architecture of the Plant Nuclear Pore Complex. *J. Exp. Bot.* **2013**, *64* (4), 823−832.

(13) Stewart, M. Molecular Mechanism of the Nuclear Protein Import Cycle. *Nat. Rev. Mol. Cell Biol.* **2007**, *8* (3), 195−208.

(14) Pedone, D.; Langecker, M.; Münzer, A. M.; Wei, R.; Nagel, R. D.; Rant, U. Fabrication and Electrical Characterization of a Pore−Cavity−Pore Device. *J. Phys.: Condens. Matter* **2010**, *22* (45), 454115.

(15) Langecker, M.; Pedone, D.; Simmel, F. C.; Rant, U. Electrophoretic Time-of-Flight Measurements of Single DNA Molecules with Two Stacked Nanopores. *Nano Lett.* **2011**, *11* (11), 5002−5007.

(16) Liu, X.; Mihovilovic Skanata, M.; Stein, D. Entropic Cages for Trapping DNA near a Nanopore. *Nat. Commun.* **2015**, *6*, 6222.

(17) Kick, B.; Praetorius, F.; Dietz, H.; Weuster-Botz, D. Efficient Production of Single-Stranded Phage DNA as Scaffolds for DNA Origami. *Nano Lett.* **2015**, *15* (7), 4672−4676.

(18) Wang, P.; Meyer, T. A.; Pan, V.; Dutta, P. K.; Ke, Y. The Beauty and Utility of DNA Origami. *Chem.* **2017**, *2* (3), 359−382.

(19) Said, H.; Schüller, V. J.; Eber, F. J.; Wege, C.; Liedl, T.; Richert, C. M1.3 - A Small Scaffold for DNA Origami. *Nanoscale* **2013**, *5* (1), 284−290.

(20) Plesa, C.; van Loo, N.; Ketterer, P.; Dietz, H.; Dekker, C. Velocity of DNA during Translocation through a Solid State Nanopore. *Nano Lett.* **2015**, *15* (1), 732−737.

(21) Kong, J.; Bell, N. A. W.; Keyser, U. F. Quantifying Nanomolar Protein Concentrations Using Designed DNA Carriers and Solid-State Nanopores. *Nano Lett.* **2016**, *16* (6), 3557−3562.

(22) Kong, J.; Zhu, J.; Keyser, U. F. Single Molecule Based SNP Detection Using Designed DNA Carriers and Solid-State Nanopores. *Chem. Commun.* **2017**, *53* (2), 436−439.

(23) Bell, N. A. W.; Keyser, U. F. Specific Protein Detection Using Designed DNA Carriers and Nanopores. *J. Am. Chem. Soc.* **2015**, *137* (5), 2035−2041.

(24) Bell, N. A. W.; Keyser, U. F. Digitally Encoded DNA Nanostructures for Multiplexed, Single-Molecule Protein Sensing with Nanopores. *Nat. Nanotechnol.* **2016**, *11* (7), 645−651.

(25) Belkin, M.; Chao, S.-H.; Jonsson, M. P.; Dekker, C.; Aksimentiev, A. Plasmonic Nanopores for Trapping, Controlling Displacement, and Sequencing of DNA. *ACS Nano* **2015**, *9*, 10598.

DOI: 10.1021/acsanm.9b00606
ACS Appl. Nano Mater. XXXX, XXX, XXX−XXX

(26) Kotnala, A.; Gordon, R. Quantification of High-Efficiency Trapping of Nanoparticles in a Double Nanohole Optical Tweezer. *Nano Lett.* **2014**, *14* (2), 853−856.
(27) Pud, S.; Chao, S.-H.; Belkin, M.; Verschueren, D.; Huijben, T.; van Engelenburg, C.; Dekker, C.; Aksimentiev, A. Mechanical Trapping of DNA in a Double-Nanopore System. *Nano Lett.* **2016**, *16* (12), 8021−8028.
(28) Liu, X.; Zhang, Y.; Nagel, R.; Reisner, W.; Dunbar, W. B. Controlling DNA Tug-of-War in a Dual Nanopore Device. arXiv 2018, No. 1811.11105v1, 1−33.
(29) Mirsaidov, U.; Comer, J.; Dimitrov, V.; Aksimentiev, A.; Timp, G. Slowing the Translocation of Double-Stranded DNA Using a Nanopore Smaller than the Double Helix. *Nanotechnology* **2010**, *21* (39), 395501.
(30) Briggs, K.; Kwok, H.; Tabard-Cossa, V. Automated Fabrication of 2-Nm Solid-State Nanopores for Nucleic Acid Analysis. *Small* **2014**, *10* (10), 2077−2086.
(31) Freedman, K. J.; Otto, L. M.; Ivanov, A. P.; Barik, A.; Oh, S.-H.; Edel, J. B. Nanopore Sensing at Ultra-Low Concentrations Using Single-Molecule Dielectrophoretic Trapping. *Nat. Commun.* **2016**, *7*, 10217.
(32) DesOrmeaux, J. P. S.; Winans, J. D.; Wayson, S. E.; Gaborski, T. R.; Khire, T. S.; Striemer, C. C.; McGrath, J. L. Nanoporous Silicon Nitride Membranes Fabricated from Porous Nanocrystalline Silicon Templates. *Nanoscale* **2014**, *6* (18), 10798−10805.
(33) Briggs, K.; Charron, M.; Kwok, H.; Le, T.; Chahal, S.; Bustamante, J.; Waugh, M.; Tabard-Cossa, V. Kinetics of Nanopore Fabrication during Controlled Breakdown of Dielectric Membranes in Solution. *Nanotechnology* **2015**, *26* (8), 084004.
(34) Kwok, H.; Briggs, K.; Tabard-Cossa, V. Nanopore Fabrication by Controlled Dielectric Breakdown. *PLoS One* **2014**, *9* (3), e92880.
(35) Madejski, G.; Lucas, K.; Pascut, F.; Webb, K.; McGrath, J. TEM Tomography of Pores with Application to Computational Nanoscale Flows in Nanoporous Silicon Nitride (NPN). *Membranes (Basel)* **2018**, *8* (2), 26.
(36) Kwok, H.; Waugh, M.; Bustamante, J. J.; Briggs, K.; Tabard-Cossa, V. Long Passage Times of Short SsDNA Molecules through Metallized Nanopores Fabricated by Controlled Breakdown. *Adv. Funct. Mater.* **2014**, *24* (48), 7745−7753.
(37) Kowalczyk, S. W.; Wells, D. B.; Aksimentiev, A.; Dekker, C. Slowing down DNA Translocation through a Nanopore in Lithium Chloride. *Nano Lett.* **2012**, *12* (2), 1038−1044.
(38) Slater, G. W.; Holm, C.; Chubynsky, M. V.; de Haan, H. W.; Dube, A.; Grass, K.; Hickey, O. A.; Kingsburry, C.; Sean, D.; Shendruk, T. N.; Zhan, L. Modeling the Separation of Macromolecules: A Review of Current Computer Simulation Methods. *Electrophoresis* **2009**, *30* (5), 792−818.
(39) Forstater, J. H.; Briggs, K.; Robertson, J. W. F.; Ettedgui, J.; Marie-Rose, O.; Vaz, C.; Kasianowicz, J. J.; Tabard-Cossa, V.; Balijepalli, A. MOSAIC: A Modular Single-Molecule Analysis Interface for Decoding Multistate Nanopore Data. *Anal. Chem.* **2016**, *88* (23), 11900.
(40) Raillon, C.; Granjon, P.; Graf, M.; Steinbock, L. J.; Radenovic, A. Fast and Automatic Processing of Multi-Level Events in Nanopore Translocation Experiments. *Nanoscale* **2012**, *4* (16), 4916−4924.
(41) Muthukumar, M. *Polymer Translocation*; CRC Press: 2011.

DOI: 10.1021/acsanm.9b00606
ACS Appl. Nano Mater. XXXX, XXX, XXX−XXX

Chapter 5

Conclusions

Nanopore translocation is an ever growing field with many exciting open questions. This article-based thesis studies some non-standard problems in the field. It does so in two ways; First, the studies are conducted with semiflexible polymers, which are not as well understood as freely jointed chains but are just as important due to the desire to understand and manipulate double stranded DNA. Second, the articles both directly and indirectly investigate the effect of the often omitted capture process in the translocation process.

However, there are still unanswered questions and there can be many extensions to these studies. In particular, insight gained from our experimental collaboration has lead to many interesting ideas that are currently the subject of further research. Given the nature of the thesis the conclusion will be separated in three sections, each summarising the key results from each article.

5.1 Semiflexible Polymer Translocation with Capture

Our study of translocation in Chapter 2 deals with the importance of the capture process on the conformations of semiflexible polymers, as well as the impact of pore diameter on the resulting dynamics. The results demostrate that the capture process has a noticeable effect in the narrow pore limit, and increasing pore size strongly impacts the translocation time distributions. We devise criteria that allow us to classify the conformational properties of the polymers at characteristic pore sizes. At small pore sizes we find that the majority of translocation events have coiled conformations and spend a lot of time in the vicinity of the pore before translocating. Given how small the pore is, only a free end can initiate translocation making the energetic cost rather high. In spite of this, we find a smaller population of polymers with stretched conformations that find the pore and initiate translocation much faster. These conformations are the result of the capture process. We classify the criteria for either case. At intermediate pore sizes we observe the same coiled conformations as before, but now the chains can sometimes overcome the bending energy needed to fold through the pore during their long waiting time. The stretched conformations are still present but are no longer a small subset of the distribution, indicating that as pore size increases the effects of capture becomes more pronounced. At large pore sizes, we find that the stretched conformations become the dominant population in the distribution. This is counterintuitive as one might expect folded conformations to be dominant due to the ease of bending through larger pores. We find that the coiled conformations are no longer present as polymers find the nanopore rather quickly and wait very little time to initiate translocation. The observations we make indicate that the capture process significantly affects the translocation dynamics of

semiflexible polymers.

5.2 Standard Translocation in the Nanofiltered Nanopore Device

Chapter 3 studies the physics of translocation for semiflexible polymers in the Nanofiltered nanopore device. We use simulations to gain insight beyond the limits of experimental resolution. From experiments we observe a transition in the relative error of the translocation time as a function of polymer length. However, the origin of this transition is unclear from experiments alone. Our simulations results show that interactions between the chains and the nanofilter are key. We show that for short polymers, the filter does not impede their dynamics resulting in the chains freely diffusing prior to the onset of translocation. At chain lengths longer than the height of the cavity we show that the filter impedes the motion of the polymer as one end can thread through the sensing pore while the other end is still translocating through the filter. At intermediate chain lengths that are shorter than the height of the cavity but longer than the shortest polymers, the chain can fully enter the cavity before initiating translocation. However, due to the filter, the conformations of these chains are consistently elongated with little variation resulting in a low relative error in the translocation. In other words the minimum in the coefficient of variation occurs at the transition between rod-like polymers and chains longer than the cavity height.

5.3 The Nanofiltered Nanopore Device as an Entropic Cage

In Chapter 4 we explore the potential of the nanofiltered nanopore device as an entropic trap for dsDNA. This version of the device has much smaller filter pores than before and boasts a larger cavity such that it can trap larger molecules. Experimental results show that the device is a good trap for long DNA strands (up to 10 kbp). However, chains of medium length (1.2 kbp) are able to escape when, given the new filter pore sizes, they should remain trapped. Using an effective multiscale simulation approach we gain insight on why this behaviour was observed. Through analysis of TEM images of the filter membrane we find that there is a subset of large, merged pores on the filter. The presence of these pores is a result of the manufacturing process for the nanofilter. Simulations at different filter pore sizes show that it is these merged pores that dominate the dynamics of the device while the smaller pores are mostly negligible. The merged pores can be large enough such that 1.2 kbp chain lengths can escape through via diffusion at the trapping time used in the experiment. Additionally, we investigate the trapping efficiency of the device at longer chains, past the experimental trapping time and find that the device is a good entropic cage. Furthermore, given that the filter manufacturing can be controlled, the properties of the trap may be tuned for specific applications.

Bibliography

[1] Joshua A Anderson, Chris D Lorenz, and Alex Travesset. General purpose molecular dynamics simulations fully implemented on graphics processing units. *Journal of Computational Physics*, 227(10):5342–5359, 2008.

[2] George B Arfken and Hans J Weber. Mathematical methods for physicists, 1999.

[3] Aniket Bhattacharya. Translocation dynamics of a semiflexible chain under a bias: Comparison with tension propagation theory. *Polymer Science Series C*, 55(1):60–69, 2013.

[4] Xin Bian, Changho Kim, and George Em Karniadakis. 111 years of brownian motion. *Soft Matter*, 12(30):6331–6346, 2016.

[5] Kyle Briggs, Gregory Madejski, Martin Magill, Konstantinos Kastritis, Hendrick W de Haan, James L McGrath, and Vincent Tabard-Cossa. Dna translocations through nanopores under nanoscale preconfinement. *Nano letters*, 18(2): 660–668, 2017.

[6] Jeffrey Chuang, Yacov Kantor, and Mehran Kardar. Anomalous dynamics of translocation. *Physical Review E*, 65(1):011802, 2001.

[7] William Coffey and Yu P Kalmykov. *The Langevin equation: with applications to*

stochastic problems in physics, chemistry and electrical engineering, volume 27. World Scientific, 2012.

[8] Pierre-Gilles De Gennes. *Scaling concepts in polymer physics*. Cornell university press, 1979.

[9] Hendrick W de Haan and Gary W Slater. Using an incremental mean first passage approach to explore the viscosity dependent dynamics of the unbiased translocation of a polymer through a nanopore. *The Journal of chemical physics*, 136(20):204902, 2012.

[10] Hendrick W. de Haan, David Sean, and Gary W. Slater. Using a péclet number for the translocation of a polymer through a nanopore to tune coarse-grained simulations to experimental conditions. *Phys. Rev. E*, 91:022601, Feb 2015. doi: 10.1103/PhysRevE.91.022601. URL `https://link.aps.org/doi/10.1103/PhysRevE.91.022601`.

[11] Cees Dekker. Solid-state nanopores. *Nature nanotechnology*, 2(4):209, 2007.

[12] Masao Doi and Samuel Frederick Edwards. *The theory of polymer dynamics*, volume 73. oxford university press, 1988.

[13] Farnoush Farahpour, Azadeh Maleknejad, Fathollah Varnik, and Mohammad Reza Ejtehadi. Chain deformation in translocation phenomena. *Soft Matter*, 9(9):2750–2759, 2013.

[14] Paul J Flory. *Principles of polymer chemistry*. Cornell University Press, 1953.

[15] Gary S Grest and Kurt Kremer. Molecular dynamics simulation for polymers in the presence of a heat bath. *Physical Review A*, 33(5):3628, 1986.

[16] Alexander Y Grosberg and Yitzhak Rabin. Dna capture into a nanopore: interplay of diffusion and electrohydrodynamics. *The Journal of chemical physics*, 133(16):10B617, 2010.

[17] Li-Qun Gu, Orit Braha, Sean Conlan, Stephen Cheley, and Hagan Bayley. Stochastic sensing of organic analytes by a pore-forming protein containing a molecular adapter. *Nature*, 398(6729):686, 1999.

[18] Timo Ikonen, Aniket Bhattacharya, Tapio Ala-Nissila, and Wokyung Sung. Unifying model of driven polymer translocation. *Physical Review E*, 85(5):051803, 2012.

[19] John J Kasianowicz, Eric Brandin, Daniel Branton, and David W Deamer. Characterization of individual polynucleotide molecules using a membrane channel. *Proceedings of the National Academy of Sciences*, 93(24):13770–13773, 1996.

[20] Lev Davidovich Landau and Evgenii Mikhailovich Lifshitz. *Course of theoretical physics - The theory of elasticity*. Elsevier, 2013.

[21] Don S. Lemons and Anthony Gythiel. Paul langevin's 1908 paper "on the theory of brownian motion" ["sur la théorie du mouvement brownien," c. r. acad. sci. (paris) 146, 530–533 (1908)]. *American Journal of Physics*, 65(11):1079–1081, 1997. doi: 10.1119/1.18725. URL `https://doi.org/10.1119/1.18725`.

[22] Kate R Lieberman, Gerald M Cherf, Michael J Doody, Felix Olasagasti, Yvette Kolodji, and Mark Akeson. Processive replication of single dna molecules in a nanopore catalyzed by phi29 dna polymerase. *Journal of the American Chemical Society*, 132(50):17961–17972, 2010.

[23] Martin Magill, Ed Waller, and Hendrick W de Haan. A sequential nanopore-

channel device for polymer separation. *The Journal of Chemical Physics*, 149 (17):174903, 2018.

[24] Erin Murphy. Forensic dna typing. *Annual Review of Criminology*, 1(1):497–515, 2018. doi: 10.1146/annurev-criminol-032317-092127.

[25] Murugappan Muthukumar. Polymer translocation through a hole. *The Journal of Chemical Physics*, 111(22):10371–10374, 1999.

[26] Murugappan Muthukumar. *Polymer translocation*. CRC Press, 2016.

[27] Vladimir V Palyulin, Tapio Ala-Nissila, and Ralf Metzler. Polymer translocation: the first two decades and the recent diversification. *Soft matter*, 10(45):9016–9037, 2014.

[28] Camille Raillon, Pierre Granjon, Michael Graf, Lorenz Steinbock, and Aleksandra Radenovic. Fast and automatic processing of multi-level events in nanopore translocation experiments. *Nanoscale*, 4:4916–24, 07 2012. doi: 10.1039/c2nr30951c.

[29] Takahiro Sakaue. Nonequilibrium dynamics of polymer translocation and straightening. *Physical Review E*, 76(2):021803, 2007.

[30] Jalal Sarabadani, Timo Ikonen, Harri Mökkönen, Tapio Ala-Nissila, Spencer Carson, and Meni Wanunu. Driven translocation of a semi-flexible polymer through a nanopore. *Scientific Reports*, 7(1):7423, 2017.

[31] Gary W Slater, Claude Desruisseaux, Sylvain J Hubert, Jean-François Mercier, Josée Labrie, Justin Boileau, Frédéric Tessier, and Marc P Pépin. Theory of dna electrophoresis: A look at some current challenges. *ELECTROPHORESIS: An International Journal*, 21(18):3873–3887, 2000.

[32] Gary W Slater, Christian Holm, Mykyta V Chubynsky, Hendrick W de Haan, Antoine Dubé, Kai Grass, Owen A Hickey, Christine Kingsburry, David Sean, Tyler N Shendruk, et al. Modeling the separation of macromolecules: a review of current computer simulation methods. *Electrophoresis*, 30(5):792–818, 2009.

[33] Arnold J Storm, Cornelis Storm, Jianghua Chen, Henny Zandbergen, Jean-Francois Joanny, and Cees Dekker. Fast dna translocation through a solid-state nanopore. *Nano letters*, 5(7):1193–1197, 2005.

[34] Christopher C Striemer, Thomas R Gaborski, James L McGrath, and Philippe M Fauchet. Charge-and size-based separation of macromolecules using ultrathin silicon membranes. *Nature*, 445(7129):749, 2007.

[35] Pauli M Suhonen and Riku P Linna. Dynamics of driven translocation of semi-flexible polymers. *Physical Review E*, 97(6):062413, 2018.

[36] W Sung and PJ Park. Polymer translocation through a pore in a membrane. *Physical review letters*, 77(4):783, 1996.

[37] Arlene A Teraoka and Iwao Teraoka. *Polymer solutions: an introduction to physical properties*. John Wiley & Sons, 2002.

[38] Carlo Vanderzande. *Lattice models of polymers*, volume 11. Cambridge University Press, 1998.

[39] Wenonah Vercoutere, Stephen Winters-Hilt, Hugh Olsen, David Deamer, David Haussler, and Mark Akeson. Rapid discrimination among individual dna hairpin molecules at single-nucleotide resolution using an ion channel. *Nature biotechnology*, 19(3):248, 2001.

[40] Loup Verlet. Computer" experiments" on classical fluids. i. thermodynamical properties of lennard-jones molecules. *Physical review*, 159(1):98, 1967.

[41] Sarah C Vollmer and Hendrick W de Haan. Translocation is a nonequilibrium process at all stages: Simulating the capture and translocation of a polymer by a nanopore. *The Journal of chemical physics*, 145(15):154902, 2016.

[42] Meni Wanunu. Nanopores: A journey towards dna sequencing. *Physics of life reviews*, 9(2):125–158, 2012.

[43] Fan Wu, Yu Fu, Xiao Yang, Li-Zhen Sun, and Meng-Bo Luo. Driven translocation of semiflexible polyelectrolyte through a nanopore. *Journal of Polymer Science Part B: Polymer Physics*, 2019.

Appendices

Appendix A

Supporting Information for Chapter 3

Supplementary Information: DNA Translocations Through Nanopores Under Nanoscale Pre-Confinement

Kyle Briggs[†]*, Gregory Madejski*[‡]*, Martin Magill*[§]*, Konstantinos Kastritis*[§]*, Hendrick W. de Haan*[§]*, James L. McGrath*[‡]*, and Vincent Tabard-Cossa*[*†]

[†] Department of Physics, University of Ottawa, Ottawa, ON, Canada

[‡] Department of Biomedical Engineering, University of Rochester, Rochester, NY, USA

[§] Faculty of Science, University of Ontario Institute of Technology, Oshawa, ON, Canada

*Corresponding Author: tcossa@uOttawa.ca, 613-562-5800 x6964

Supplementary Section S1: Physical Properties of Nanofilters

SEM and TEM imaging of sample sections of nanoporous nitride (NPN) material from the wafer used for this project reveal that not all of the visible features are through-holes (Supplementary Figure S1). While porosity is calculated to be as high as 20% if all features are taken into account (Supplementary Figure S1a), TEM imaging of the pores reveals a porosity of 5% for this particular batch of NPN when considering only through-holes (Supplementary Figure S1b-c).

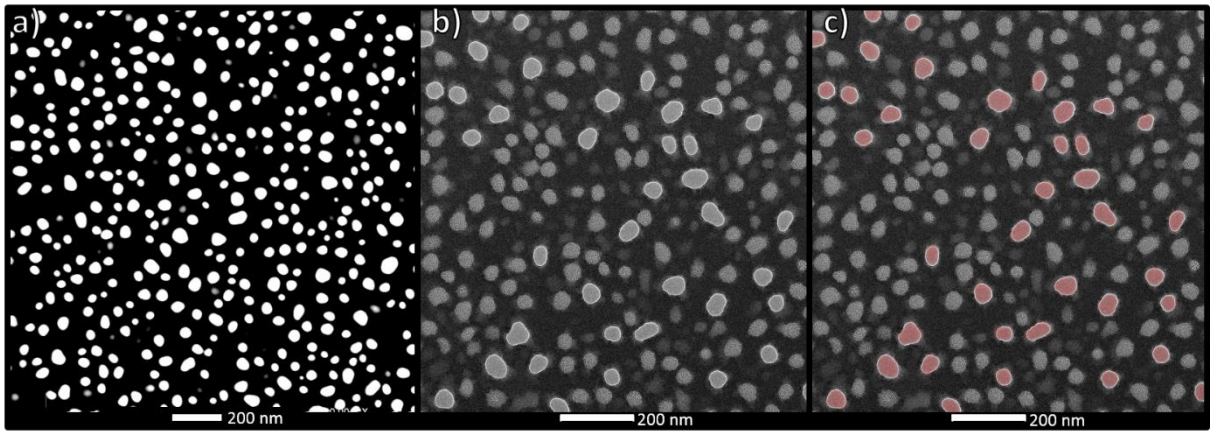

Supplementary Figure S1: a) STEM micrograph of NPN with high contrast, showing an apparent 20% porosity. b) Closer and lower contrast view of a TEM image of 5% porous NPN, showing partially opened nanopores. c) The same image as b), with false color. Only nanopores highlighted in red contribute to the porosity of the wafer.

Transferring the nanofilter structure using water vapor is a dynamic process, as the nanofilter rips and sticks to a target substrate. Applied here, this method provides a simple and effective way to fabricate a nanocavity while still allowing fluidic access to the interior space (Supplementary Video S1). Conformal contact is achieved due to the inherent flexibility of such a thin material, since the bending resistance for membranes scales with the third power of membrane thickness. Despite this flexibility, once the nanofilter is wetted and in close contact with the substrate, it is very resistant to meniscus stresses, surviving fluid shear stress from wetting and rewetting (Supplementary Video S2). However, if the membrane is not in close contact, the membrane can be torn apart on a meniscus of liquid (Supplementary Video S3).

If the nanofilter is unevenly wetted, wrinkles can form and the gap between the nanofilter and the sensing pore can vary. In order to avoid this defect, and to ensure that dsDNA cannot shunt the nanofilter by going around the edges, we seal the nanofilter in place by painting PDMS by hand around the silicon nitride membrane of the single sensing pore, an example of which is shown in Supplementary Figure S2.

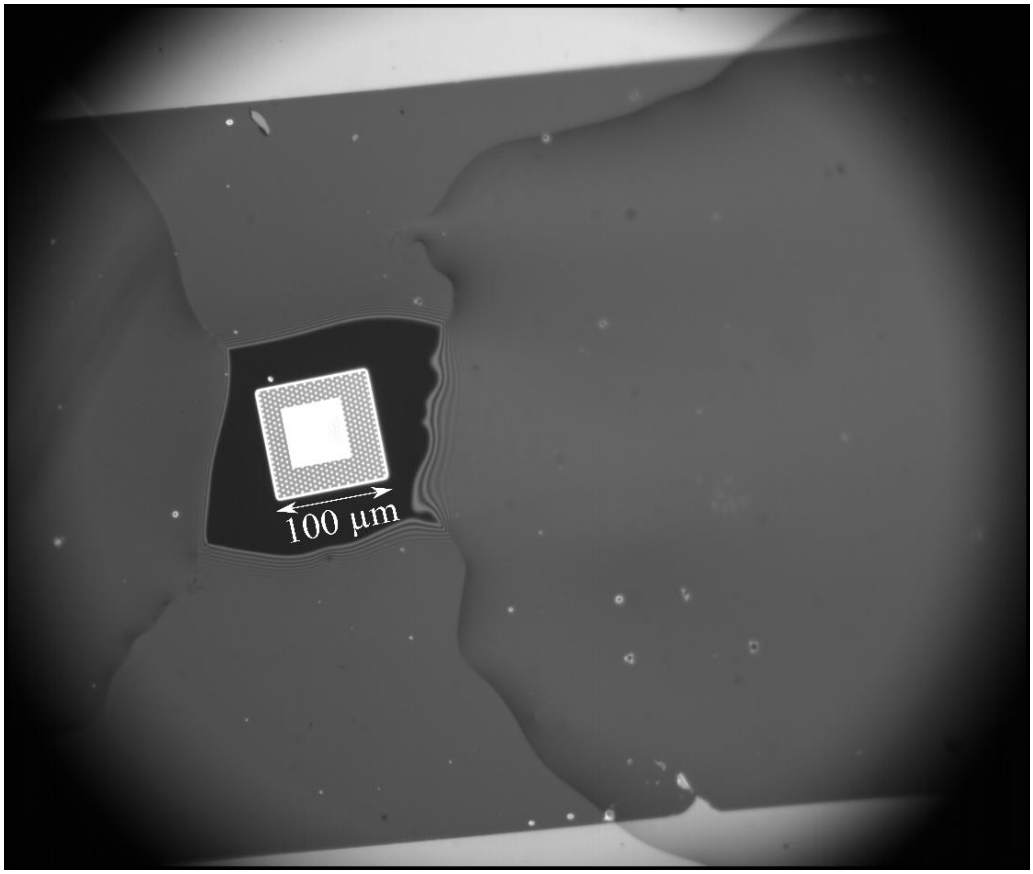

Supplementary Figure S2: PDMS is painted over the nanofilter. The central white rectangle is the free-standing silicon nitride membrane which will contain the sensing pore. The concentric square is the silicon dioxide spacer, containing a hexagonal grid of 1µm microwells. The irregular black area defines the area, which is not covered by PDMS. The large dark grey rectangle comprising most of the figure is the nanofilter membrane.

Even though only a single sensing pore is fabricated and consequently only a single microwell is active in each device, multiple microwells are necessary for several reasons. As discussed above, NPN is an extremely flexible material, able to mould itself around microscopic contours. Using 1 µm diameter microwells ensures that the maximal bending displacement of the nanofilter within a given microwell is insufficient to contact the sensing membrane, maintaining the cavity. Second, the CBD technique is sensitive to exposed area, taking a longer time to fabricate pores on small membrane areas[1]. Using a large number of microwells ensures a sufficiently large active membrane area that nanopore fabrication is limited to a few minutes.

Finally, the use of multiple microwells ensures that at least one will be wetted easily, though in practice wetting is near 100%.

The electrical resistance of the nanofilter can be calculated simply by assuming each pore is a parallel resistor using equation 3 from Kowalczyk *et al.* [2], giving approximately 100 kΩ per oxide microwell. During CBD fabrication, the current through the entire system is on the order of 10-100 nA. Assuming that current is divided evenly among the microwells, this results in an electrical current per microwell on the order of ~0.1-1 nA, and a corresponding voltage drop across the nanofilter of only ~1-10 mV, far too little to have any effect on the nanofilter pore size distribution.

After pore fabrication, the nanofilter remains electrically invisible. A typical sensing pore used in this study is between 3-14 nm in diameter, corresponding to a resistance in 3.6M LiCl of 10-100 MΩ. With a voltage bias of ΔV = 200 mV applied across the entire system, the voltage drop across the nanofilter is 10^{-3}-$10^{-2}\Delta V$, and has negligible effect on the electrical response of the single sensing pore. The sensing pore can even be conditioned at moderate to high voltages to increase its size or tune noise characteristics[3] without impacting the pore size distribution of the nanofilter.

Typical I-V responses and PSDs for pores with and without the nanofilter are shown in Supplementary Figure S3, demonstrating that the nanofilter has an insignificant effect on the electrical properties of the sensing pore. The root-mean-square (RMS) noise at 900 kHz bandwidth ranges from 140-220 pA.

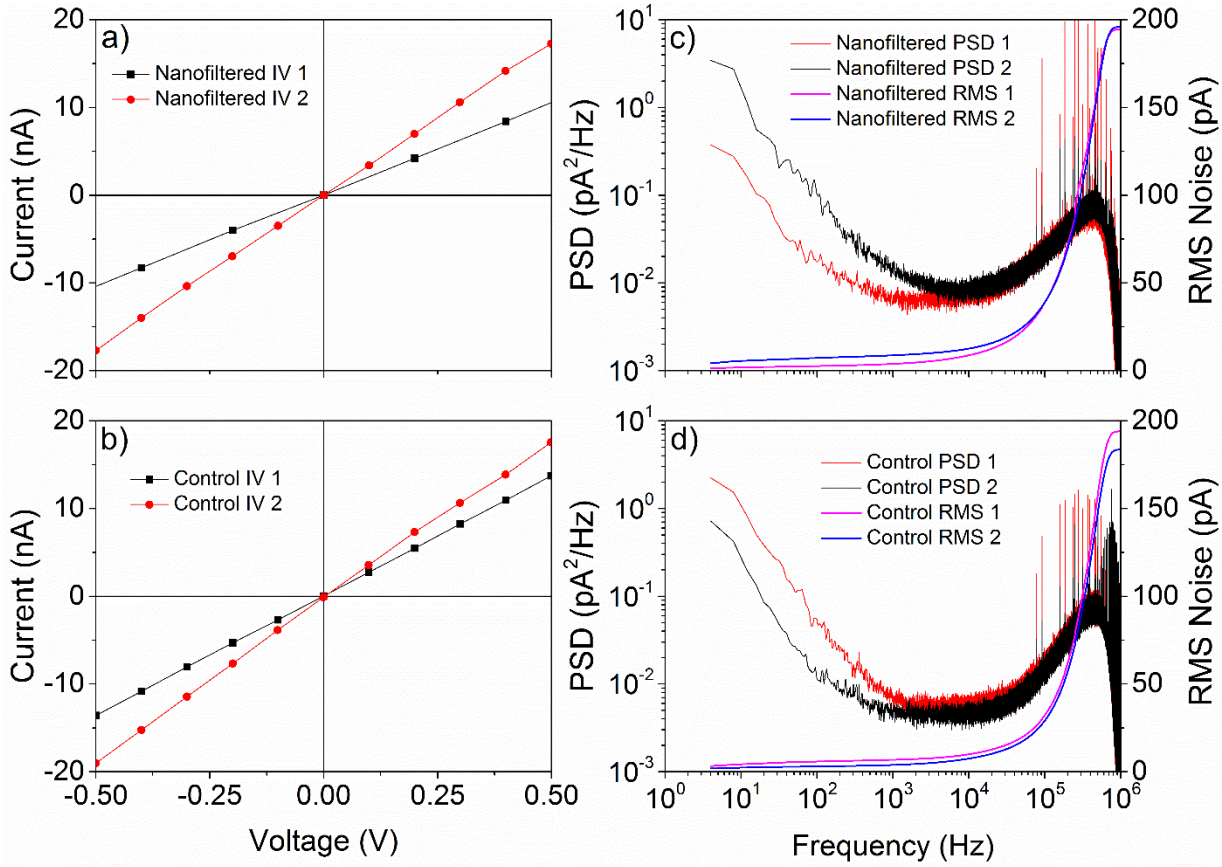

Supplementary Figure S3: a,b) I-V response of nanofiltered (a) and control (b) pores, showing linear behavior in both cases. c,d) power spectral densities and RMS noise profiles in nanofiltered (c) and control (d) pores. PSDs are digitally low-pass Bessel filtered at 900 kHz. The high-frequency spikes (92.5 kHz + harmonics) were later identified to be due to a malfunctioning graphics card, but their contribution to the total RMS current noise is marginal and thus does not interfere with sensing.

Supplementary Section S2: Simulation Setup

Coarse-grained Langevin dynamics (LD) simulations were used to explore the physical mechanisms underlying the behavior witnessed in experiment. The ESPResSo molecular dynamics software package was used for this purpose[4]. The DNA molecules were modelled as linear polymers composed of N identical spherical monomers. Adjacent monomers along the chain were joined using the finitely-extensible nonlinear elastic (FENE) potential,

$$U_{FENE}(r) = -\frac{k_{FENE}}{2} r_{max}^2 \ln\left(1 - \frac{r^2}{r_{max}^2}\right), \quad (1)$$

where k_{FENE} and r_{max} are constants representing the stiffness of the bond and the maximum possible extension of the bond, respectively, and r is the center-to-center distance between the monomers[5]. Excluded volume interactions between monomers were modelled using the Weeks-Chandler-Andersen (WCA) potential, given by

$$U_{WCA}(r) = \begin{cases} 4\varepsilon\left[\left(\frac{\sigma}{r}\right)^{12} - \left(\frac{\sigma}{r}\right)^{6}\right] + \varepsilon & r \le 2^{\frac{1}{6}}\sigma \\ 0 & r > 2^{\frac{1}{6}}\sigma \end{cases}, \quad (2)$$

where ε and σ are the energy and length scales of the interaction, respectively[5]. The FENE parameters were chosen in terms of the WCA parameters to be

$$k_{FENE} = 30\frac{\varepsilon}{\sigma^2}, \qquad r_{max} = 1.5\sigma, \quad (3)$$

in line with the seminal work by Kremer and Grest that demonstrated the robust numerical stability of this configuration[6]. The energy scale of the WCA potential was set equal to $\varepsilon = k_B T$, the thermal energy of the system set in the LD thermostat. All other energies were normalized to this value, and as such $k_B T$ was set to a numerical value of 1.0. With these choices of parameters, the average equilibrium bond length between adjacent monomers was roughly $b = 0.97\sigma$, so σ will be considered the effective monomer size. The friction coefficient γ of the LD thermostat was also set to 1.0 (except during equilibration, as discussed below).

In addition to the FENE and WCA pairwise interactions, a three-body angular potential was used to model polymer stiffness. This potential was chosen simply to be harmonic in the angle θ formed by any three consecutive monomers along the chain:

$$U_{angle}(\theta) = \left(\frac{k_{angle}}{2}\right)\theta^2 . \quad (4)$$

Using this angular potential and the FENE and WCA potentials as specified above, the persistence length L_p of the simulated polymer satisfies

$$L_p \approx k_{angle} . \quad (5)$$

The remaining free parameters of the potentials were chosen to establish a correspondence between the polymer in simulation and the DNA chains in experiment. The steric width of DNA is roughly 2.4 nm[7], but its effective width can be somewhat larger than this[7–10], depending on electrolytic conditions. For this reason, and for computational tractability, σ = 5 nm was chosen. The remaining length scales of the system were derived from this choice, so σ was set to a numerical value of 1. In particular, the persistence length of DNA is roughly 30 nm under relevant conditions[8,9], and so the simulated polymer should satisfy $L_p = 6\sigma$. Using Supplementary Equation 5, this was implemented by setting the numerical value of k_{angle} = 6.0.

The geometry of the system was implemented in ESPResSo using pore constraint objects. These are planar boundaries of finite thickness through which a cylinder is removed. The same WCA interaction used to represent excluded volume interactions between monomers was defined between the monomers and these boundaries. For monomer-constraint interactions, the distance r was computed from the center of the monomer to the nearest point on the boundary. When the center of the monomer is a distance σ from the boundary, its interaction energy is equal to k_BT. This distance from the boundary determines the effective dimensions of the pore. The effective dimensions are mapped to the measured experimental lengths of the device using σ = 5 nm.

One pore constraint was used to define the sensing pore, which was given effective dimensions of $d_{eff} = 2.6\sigma$ and $t_{eff} = 4\sigma$, where d_{eff} is the effective radius of the pore and t_{eff} is its effective length. These parameters correspond to a sensing pore that is 13 nm in diameter and 20

nm in length. The sensing pore was placed in the center of the microwell. Although this was not necessarily the case in experiment, it was considered a natural first approximation.

By default, the pore constraints in ESPResSo only contain a single pore in each plane. As such, only a single pore of the nanofilter was represented, with $d_{eff} = 2.6\sigma$ and $t_{eff} = 10\sigma$. The postulated events wherein a single chain threads through two pores in the nanofilter simultaneously cannot be represented in these simulations. Future work will utilize modified pore constraints capable of capturing this phenomenon. Note that d_{eff} for the pore in the nanofilter was set to 2.6σ = 13 nm, which is much smaller than the pore sizes seen in experiment. This choice was used to enforce single-file passage of the polymer through the nanofilter. In closer agreement with experimental values, the electric field in the pore of the nanofilter was set according to the correct filter porosity, and the field above the nanofilter pore was set as if the pore had a radius of 5.0 sigma = 25 nm, in closer agreement with experimental values. The location of the pore in the nanofilter was set to 30σ off-axis from the sensing pore. Finally, the walls of the microwell were also represented by a pore constraint, with $d_{eff} = 200\sigma$ and $t_{eff} = 40\sigma$.

The final component of the simulation model is the electric field. In the experiments, a voltage drop of 200 mV was fixed from far above the nanofilter to far below the sensing pore. For the simulations, the electric field was solved in a piecewise fashion. Analytic forms were used on the cis side of the nanofilter and inside the pore in the nanofilter. In the gap between the two membranes, the field was solved numerically. The field on the trans side of the sensing pore was neglected.

The numerical solution to the field inside the device was obtained using a second-order finite difference method to find the electric potential. The electric potential was assumed to satisfy Laplace's equation. The system was represented in cylindrical coordinates, with the $\rho = 0$

axis placed in the middle of the sensing pore and parallel to its axis. Homogeneous Neumann boundary conditions were applied orthogonal to the effective dimensions of the pore constraints inside the sensing pore, on the surface of the sensing pore membrane, and at the walls of the inter-membrane gap. These represent insulating boundaries. The trans opening of the sensing pore was modelled as a Dirichlet boundary condition, representing a surface of constant electric potential. This is a good approximation, since the electric field must be approximately axial inside the sensing pore. Finally, the inner boundary of the nanofilter was approximated by a Dirichlet boundary condition. This approximation was made in light of the low electrical resistivity presented by the nanofilter in comparison to the sensing pore, and since the exact locations of the pores in the nanofilter in the membrane vary from device to device.

As a result of these choices for boundary conditions, the system for the electric potential is cylindrically symmetric. Laplace's equation was solved in (ρ,z) without angular dependence. The solver was implemented in C using LAPACK[11]. The solution for the electric potential energy per monomer is shown in Supplementary Figure S4, expressed in units of $k_B T$.

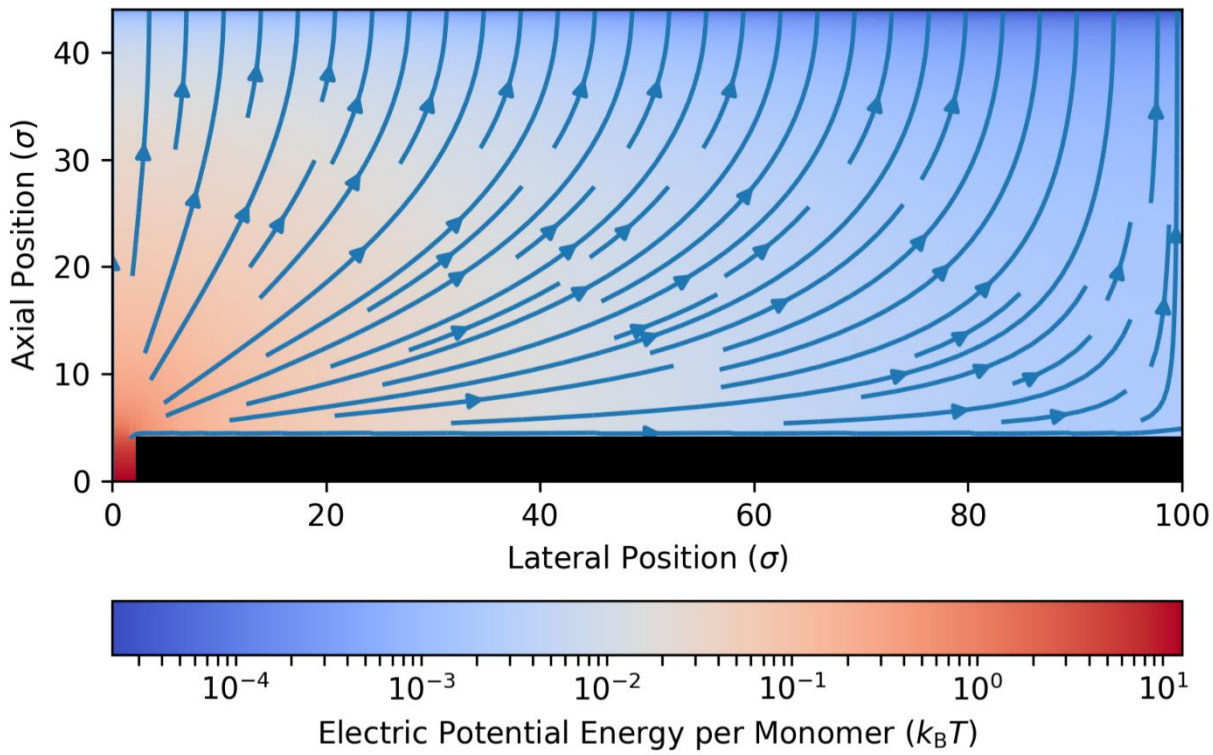

Supplementary Figure S4: Numerical solution for the electric potential between the two membranes. The bottom of the nanofilter corresponds with the top of the figure. The electric potential is expressed in simulations in terms of the electric potential energy of a monomer at a given position in the system.

The numerical field was only defined up to the inner boundary of the nanofilter. Inside the pore in the nanofilter the electric field was modelled as purely axial. The magnitude of this electric field was chosen by conservation of electric flux, as follows. The total axial electric flux of the system passes through the sensing pore, and the field is essentially axial therein. If the flux through the sensing pore and a given pore in the nanofilter are Φ_{sp} and Φ_{fp}, respectively, and there are N_{fp} pores in the active portion of the nanofilter, then the relation

$$N_{fp}\,\Phi_{fp} = \Phi_{sp} \tag{6}$$

must hold. Since the field is purely axial in the pores, this is equivalent to

$$N_{fp} E_{fp} \pi r_{fp}^2 = E_{sp} \pi r_{sp}^2 \,. \tag{7}$$

Solving this for E_{fp} yields

$$E_{fp} = \left(\frac{1}{N_{fp}}\right)\left(\frac{r_{sp}}{r_{fp}}\right)^2 E_{sp} . \quad (8)$$

The number of pores in the nanofilter was obtained from the porosity ϕ to be

$$N_{fp} = \left(\pi R_{gap}^2\right)\frac{\phi}{\pi r_{fp}^2}, \quad (9)$$

so that the field in the nanofilter pores can be expressed as

$$E_{fp} = \left(\frac{1}{\phi}\right)\left(\frac{r_{sp}}{R_{gap}}\right)^2 E_{sp} . \quad (10)$$

Above the nanofilter, the electric field was modelled by the sum of two terms. Near each pore in the nanofilter, the field should be well-represented by the analytic solution

$$E_{analytic} = \frac{\hat{\mu}\, V_0}{\pi r_{pore}\cosh(\mu)\sqrt{\sinh^2(\mu)+\sin^2(\nu)}}, \quad (11)$$

obtained in oblate spheroid coordinates for a single nanopore[12], with $r_{pore} = 5.0\sigma$. Farther above the nanofilter, the fields from all nanofilter pores will cancel all but their axial components, so the field should converge to an axial profile. The field above the nanofilter was therefore modelled as

$$E_{cis} = E_{analytic} + E_{par} , \quad (12)$$

where E_{par} represents the (axial) field a distance comparable to R_{gap} above the nanofilter, and $E_{analytic}$ is of the form given above. The magnitude of E_{par} was chosen to be

$$E_{par} = \phi E_{fp} = \left(\frac{r_{sp}}{R_{gap}}\right)^2 E_{sp} , \quad (13)$$

which is the field magnitude obtained if the electric flux passing through the sensing pore is redistributed into a cylinder of radius R_{gap}. This is an approximation to the field profile that would be present at the nanofilter location if the nanofilter were not present. The magnitude of V_0 for $E_{analytic}$ was chosen such that E_{cis} is equal to E_{fp} at the cis side of the nanofilter membrane.

The preceding paragraphs have established the shape of the electric field profile for the system. However, its absolute magnitude remains unspecified. This was chosen by increasing the field magnitude until the distributions of folded events seen in simulations were comparable to those in experiments. The total voltage drop across the simulation system was set to $12.7 k_B T$. This was approximately 40% stronger than the weakest field strength that enabled folded events to occur at all.

The units of simulation time were mapped to units of experimental time by equating the respective drift velocities. The experimental drift velocity was taken to be

$$v_{exp} = \mu \left(\frac{V_{exp}}{L_{exp}} \right) \left[\frac{m}{s} \right], \tag{14}$$

where the units of meters and seconds are shown explicitly, where[13] $\mu = 0.6 \cdot 10^{-8}$ $m^2 V^{-1} s^{-1}$, V_{exp} = 200 mV, and L_{exp} is a characteristic length scale. Similarly, in simulation the drift velocity is

$$v_{sim} = \left(\frac{1}{\gamma} \right) \left(\frac{V_{sim}}{L_{sim}} \right) \left[\frac{\sigma}{\tau} \right], \tag{15}$$

where σ is the monomer size, τ is the simulation time unit, and the remaining quantities are expressed in terms of simulation units. Here γ is the friction coefficient, V_{sim} is the voltage drop across the system, and L_{sim} is the same characteristic length scale as L_{exp}. Equating v_{sim} to v_{exp} and solving for τ yields

$$\tau = \left(\frac{1}{\mu \gamma} \right) \left(\frac{V_{sim}}{V_{exp}} \right) \left(\frac{L_{exp}}{L_{sim}} \right) \left[\frac{\sigma}{m} \right] [s], \tag{16}$$

where L_{exp} and L_{sim} are the same characteristic length expressed in SI units and simulation units, respectively. Choosing this length to be equal to σ = 5 nm yields

$$\tau \approx 265\ ns. \tag{17}$$

The simulations themselves were conducted as follows. The initialization modelled the polymers as being at equilibrium when they were captured by the nanofilter, and imposed that chains must thread through the nanofilter in single file. The first 5% of monomers in a chain

(rounded up to the nearest monomer) were fixed in a straight line through the pore in the nanofilter while the rest of the chain was evolved under the LD equations with the friction coefficient γ reduced to 0.1 from the value of 1.0 used in the main simulations. After an equilibration period of 100Nτ, the fixed monomers were released and γ was returned to 1.0. Next, the polymer was allowed to evolve under the influence of the LD equations. If the polymer retracted entirely to the cis region above the nanofilter, the event was considered a failed threading attempt and the polymer was reset. Each simulation was terminated when the entire polymer was located in the trans region of the sensing pore. The entire process was repeated until 1000 successful translocations were recorded for several chain lengths N. An illustrative translocation event is shown in Supplementary Video 4, for a chain with N = 200.

To study the influence of polymer dynamics between the nanofilter and the sensing pore, simulations were performed wherein the chain was initialized with its first monomer fixed in the sensing pore. Equilibration proceeded as in the main simulations, and events that retracted from the sensing pore were reset.

Supplementary Section S3: Analysis of Passage Time Distributions

The distribution of unfolded passage times t is well characterized by a log-normal distribution, having the form

$$p(\ln t) = A \exp\left(-\frac{(\ln t - M)^2}{2s^2}\right), \tag{18}$$

where A, M, and s are variable parameters for the non-linear fit. This form is purely for mathematical convenience rather than being physically motivated. Other groups have used a simple first-passage time distribution model which produces good fits[14] but which was originally intended for use with featureless nanoparticles. More complex models exist which take into

account the polymer nature of the analyte as well as pore-analyte interactions[15], but these depend on parameters which are unavailable experimentally. Here, we use a simple form, which allows us to easily extract metrics of interest. In cases where long polymers lead to an extended tail of events which thread through two different nanofilter pores, only the log-normal part of the passage time distribution, representing unhindered translocations, is considered when calculating mean and standard deviation passage times.

The mean τ and standard deviation σ of the passage times are related to the fit parameters M and s by

$$\tau = \exp\left(M + \frac{1}{2}s^2\right) \tag{19}$$

and

$$\sigma = \exp\left(M + \frac{1}{2}s^2\right)\sqrt{\exp(s^2) - 1}\,. \tag{20}$$

The coefficient of variation is then

$$\frac{\sigma}{\tau} = \sqrt{\exp(s^2) - 1}\,. \tag{21}$$

The number of events detected by each device and for each length of dsDNA is presented in Supplementary Table S1. Only single-file, unfolded events are used for passage time distribution fitting.

In addition, the pore size is corrected for local deviations from a cylindrical pore shape following the method used in previous work[16]. Briefly, the effective membrane thickness L_{eff} is calculated from the conductance blockage ΔG of dsDNA in the pore assuming d_{DNA} = 2.2 nm, using

$$L_{eff} = \frac{\sigma\pi d_{DNA}^2}{4\Delta G}, \tag{22}$$

where σ is the conductivity of the electrolyte solution. The pore diameter *d* is then calculated using this effective thickness from the open-channel conductance *G* using[2]

$$d = \frac{G}{2\sigma}\left(1 + \sqrt{1 + \frac{16\sigma L_{eff}}{\pi G}}\right). \quad (23)$$

Since a number of these pores were unstable, both the size at the beginning and end of the experiment are given in Supplementary Table S1.

Supplementary Table S1: Event counts for every experiment that contributed data to the paper. Run time varied between experiments, so total event numbers do not necessarily reflect differences in capture rate. For a given device, the order in which DNA lengths were studied corresponds to the order of increasing pore size.

Pore	Type	DNA Length (bp)	Events	Unfolded Events	L_{eff} (nm)	d_i (nm)	d_f (nm)
K417	Nanofiltered	250	24,164	21,162	12.8	7.0	7.1
		1000	6,084	3,392	12.6	7.2	7.2
K423	Nanofiltered	1000	3,802	3,587	15.2	7.0	7.5
		2000	160	158	16.8	9.1	9.1
K434	Nanofiltered	100	9,483	9,483	12.1	8.5	9.0
		250	3,760	3,594	10.6	4.7	4.8
		500	10,362	8,603	11.4	5.5	5.6
		1000	23,691	12,780	12.7	6.7	6.7
		2000	25,686	12,675	13.0	7.3	7.3
		3000	16,040	6,265	13.0	8.0	8.1
K435	Nanofiltered	100	754	754	8.4	4.1	4.2
		250	15,781	15,259	8.9	4.5	4.5
		500	6,668	6,323	8.7	4.3	4.3
		1000	15,214	13,143	8.9	4.6	4.6
K439	Nanofiltered	750	3,885	3,169	15.5	7.6	8.0
		1200	6,550	2,786	17.2	9.4	9.9
		4000	1,181	315	17.4	9.9	10.7
K454	Nanofiltered	1000	5,565	3,003	12.6	6.1	7.3
K462	Nanofiltered	500	6,294	5,011	9.5	5.2	5.7
		1000	3,933	2,645	10.1	6.4	6.8
		1500	2,385	1,231	11.7	8.3	8.7
		Mix (500, 1000, 1500)	38,029	20,363	12.3	9.3	9.5
K465	Nanofiltered	500	13,748	9,219	13.1	10.1	10.4
		1000	5,802	2,880	12.8	9.4	9.6
		1500	4,932	2,010	11.9	7.7	8.5
		Mix (500, 1000, 1500)	13,409	8,261	12.3	6.1	6.9
K478	Nanofiltered*	2000	890	740	11.8	5.4	5.6
K443	Control	1500	3,170	1,842	11.4	7.0	7.1
K444	Control	250	38,256	32,851	13.7	12.4	12.6
		500	38,358	24,531	11.9	9.2	9.6
		1000	4,801	2,411	11.4	7.5	8.0
		2000	18,497	6,406	12.2	10.4	10.6
K445	Control	250	308,149	256,688	11.5	11.7	11.7
		500	141,302	91,819	11.5	11.4	11.4
		750	8,424	6,352	9.2	5.4	5.6
		1000	26,728	13,044	11.7	11.1	11.2
		1200	4,403	2,540	10.4	7.1	7.5
		1500	12,636	5,038	11.0	8.7	8.7
		3000	13,776	3,979	10.9	8.9	9.0
K446	Control	100	3,836	3,836	6.0	3.2	3.2
		500	18,729	14,950	9.0	5.8	6.3
		750	41,215	22,670	9.9	8.5	8.6
		1200	31,582	13,869	9.6	8.9	9.1

		3000	15,776	4,464	9.8	9.6	9.7
K447	Control	100	14,876	14,876	8.2	8.4	8.6
		250	222,942	152,133	8.9	7.7	8.1
		750	30,397	15,026	8.7	7.1	7.3
		1000	19,487	8,186	8.4	6.2	6.6
		4000	27,062	7,075	8.9	9.5	9.6
K466	Control	500	14,847	10,387	9.4	7.0	7.1
		1000	4,861	2,962	10.3	6.3	6.6
		1500	3,745	2,563	9.5	4.9	5.2
		Mix (500, 1000, 1500)	5,237	4,693	8.9	4.4	4.4
K467	Control	500	6,599	5,127	8.5	4.9	4.9
		1000	2,817	2,006	8.4	4.9	4.9
		1500	5,733	3,341	8.3	4.9	4.9
		Mix (500, 1000, 1500)	37,417	23,643	8.3	4.9	5.1

* Note that K478 used a different nanofilter membrane with higher porosity and smaller average pore size and consequently required higher voltage to translocate dsDNA. It was therefore not included in the passage time analysis.

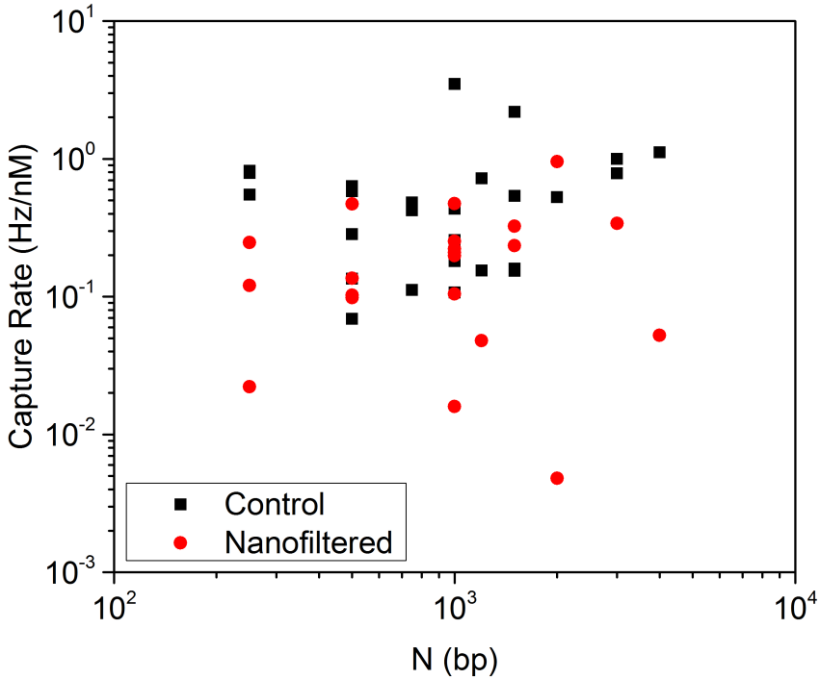

Supplementary Figure S5: Normalized capture rates for all experiments conducted in both control (black squares) and nanofiltered (red circles) pores.

The capture rates are largely unaffected by the presence of the nanofilter, as can be seen in Supplementary Figure S5. While it is to be expected that very long polymers might have reduced capture rates due to high entropic cost of passage through the nanofilter, this was not significantly observed for the lengths of DNA studied here.

Supplementary Section S4: Size Separation of dsDNA by Mean Passage Time

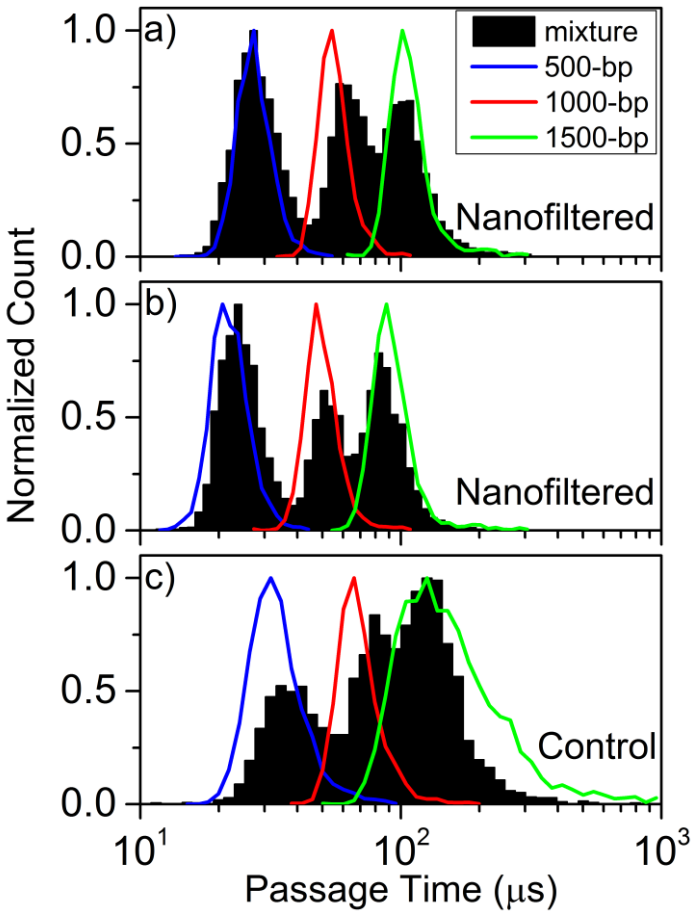

Supplementary Figure S6: a, b) Passage time distributions for single-file translocation events using equimolar mixtures of 500 bp, 1000 bp, and 1500 bp dsDNA strands with a nanofilter. The line plots in each case shows the distribution for each species alone on the same nanopore, while the black histogram gives the distribution of the mixture. c) The same data for the case of a pore without the nanofilter.

Regular solid-state nanopores are usually unable to distinguish populations of different dsDNA sizes with better than ~1000 bp[17] resolution, unless their diameter is very well controlled to precisely 3-nm so as to minimize any DNA self-interaction[14]. Here, the reduced standard deviation in passage times through nanofiltered pores can be leveraged to improve resolution without the need to precisely control the pore diameter. We investigate this effect by translocating equimolar mixtures of different DNA sizes in a single device. Supplementary Figure S6 shows the results of using equimolar mixtures of 500 bp, 1000 bp, and 1500 bp dsDNA. The passage time distributions clearly show all three well-separated peaks

(Supplementary Figures S6a and S6b). Since LiCl is known to broaden passage time distributions compared to KCl[18], the resolution can most likely be further improved by using a different electrolyte, albeit for a different range of polymer lengths. While some control pores can also reveal the presence of three peaks in passage time distribution (Supplementary Figure S6c), the nanofiltered pores have a tighter distribution and more reliable peak separation.

Supplementary Section S5: Slower Passage Time in Small Control Pores

As illustrated in Figure 4a of the main manuscript, the mean passage time through unfiltered pores fluctuates above that seen with filtered pores of the same size. This was attributed to two mechanisms: small unfiltered pores lead to coiled conformations at the onset of translocation, which are prone to self-interactions and interactions with the membrane; and large unfiltered pores have large capture radii, leading to elongated conformations at the onset. Supplementary Figure S7 provides additional evidence for these interpretations. It shows the mean passage times for filtered and unfiltered pores as a function of pore diameter for chain lengths of 250, 500, 750, 1000, and 1200 basepairs.

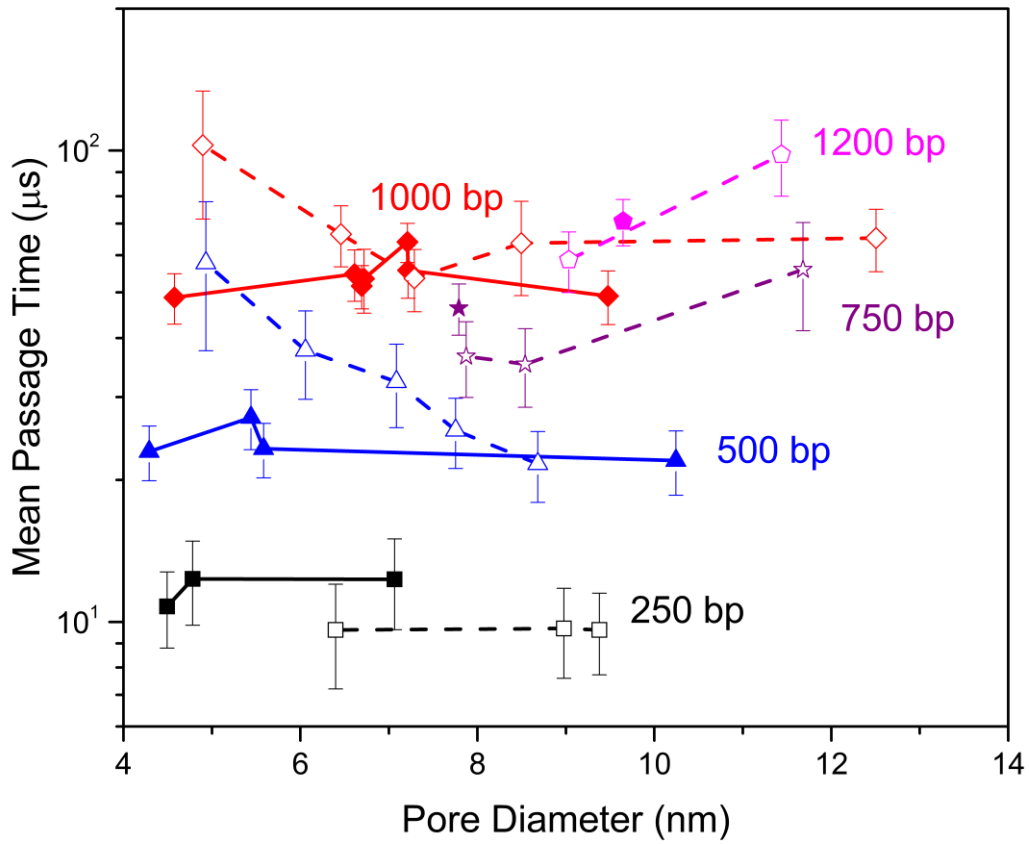

Supplementary Figure S7: Dependence of mean passage time on pore diameter for a selection of given DNA lengths.

The 250bp case demonstrates that these chains are too small for their translocation to be affected by the filter, which is consistent with Figure 4c in the main text. In the 500bp and 1000bp cases, the mean passage times increase for small pore diameters in the unfiltered pores but not the filtered pores. The increase occurs in a smooth fashion as pore diameter is reduced at fixed chain length, strongly suggesting that pore diameter is the driving factor causing the increase. Furthermore, the filtered pores consistently lack the increase, indicating that the filter reliably eliminates this phenomenon regardless of its origin.

Conversely, in the 750 and 1200 bp cases, the mean passage times increase with increasing pore diameter for unfiltered pores. This effect is not clearly visible in the 1000bp case, but this is likely due to statistical fluctuations. The trend is not visible among filtered pores, as

the dataset does not include sufficiently many large filtered pores to deduce a trend. However, those large filtered pores that are present have passage times consistent with the trends observed in the control pores.

Additionally, translocation is slower in larger pores, as expected due to polymer elongation. Thus, the largest of the control pores lead to slower translocation than the nanofiltered pores. It is important to note, however, that the dataset contains more large control pores than large nanofiltered pores, so it is unclear whether large nanofiltered pores would also exhibit slower translocation than smaller nanofiltered pores. However, it is clear from Figure 4 that the nanofilter reduces both variability within a given pore (Figure 4b) as well as variation between pores (Figure 4a).

Supplementary Section S6: Long Passage Time Events

In addition to the adsorbed events discussed in the main text, there are at least two additional plausible explanations for the very long events observed in some nanofiltered devices which we can rule out. First, simulations performed for a polymer corresponding to ~2200 bp (R_g ≈ 82 nm) indicate that the average translocation time is dependent on the elongation state of the polymer. Taking into account the gap height, for $N \gtrsim 1300$ bp there will be a significant population of molecules which still have part of their length on the cis side of the nanofilter when captured by the sensing pore, resulting in a highly elongated conformation with high fluid drag (Supplementary Figure S8a). This is in line with the experimental onset of the long tail of events. However, while our simulations show that increased drag for elongated events can

account for some increase in the translocation time, it is insufficient to explain the multiple orders of magnitude increase in passage times seen in the longest events.

Second, we note that for sufficiently long dsDNA, it is possible to thread through two pores in the nanofilter and for both arms of the polymer to come close to the sensing pore. In this case, not only is the polymer highly elongated, but there are competing pulling forces which further extend the passage time[19]. While these double-threaded events do occur, as shown Supplementary Figure S9, our simulations indicate that these competing forces are still insufficient to explain the long passage times in the tail of the distribution unless both ends of the polymer are actually captured by the sensing pore, and the events in the long tail spend most of their time in a single-occupation state which is incompatible with this picture.

Long polymers have a significant probability of double-threading through two different pores in the nanofilter before reaching the sensing pore, with a probability which is dependent on the polymer length and the average distance between neighboring nanofilter pores. Supplementary Figure S8 presents simulation results for the probability that the polymer will still have part of its length on the cis side of the nanofilter at the moment it is captured by the sensing pore, showing an onset of non-negligible probability for the presence of these tails around N=1300 bp.

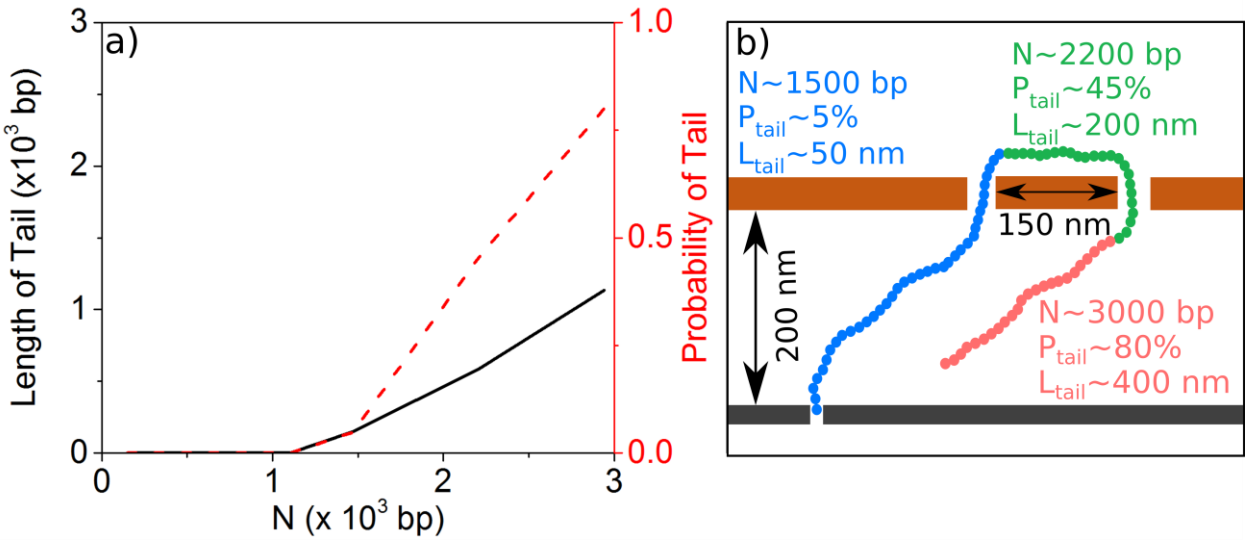

Supplementary Figure S8: a) Simulated probability and average length of a segment (tail) of DNA remaining on the cis side of the nanofilter at the moment of capture by the sensing pore, which could be captured by a second pore in the nanofilter. b) Schematic representation of the capture of DNA tails by a second pore in the nanofilter.

For molecules that are very long compared to the gap height, the sensing pore exhibits very consistent clogging modes consisting of two sequential blockage levels corresponding to one and two strands of dsDNA present in the sensing pore. This is most likely due to double threading of dsDNA through the sensing pore while straddling two pores in the nanofilter, as shown schematically in Supplementary Figures S8b and S9a. Reversing the voltage polarity can temporarily clear the clog, but it reappears after a short interval of normal baseline (Supplementary Figure S9b). Once this clogging mode occurs, even flushing out the flow cell with clean buffer is unable to remove it permanently, indicating that the offending dsDNA strand is most likely tangled in the nanofilter.

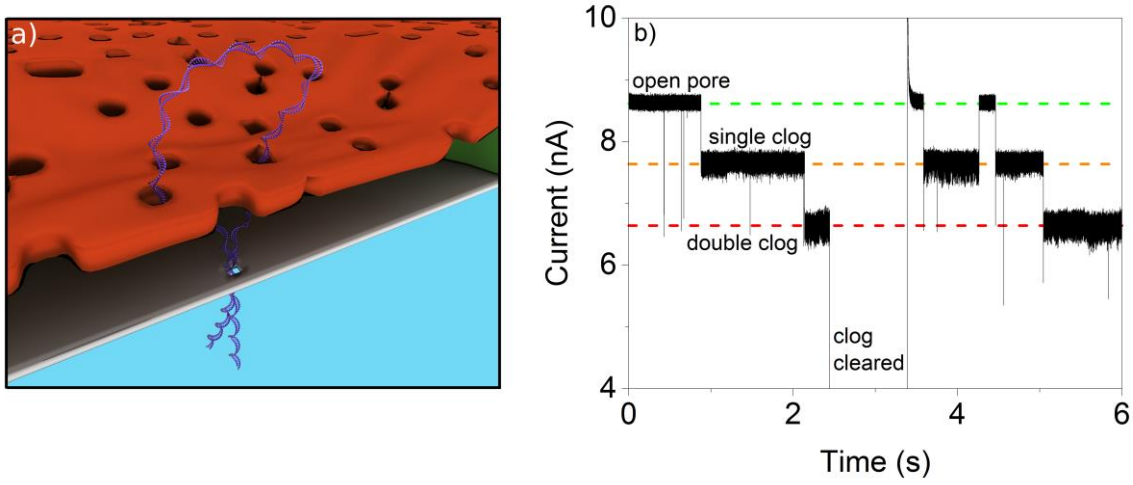

Supplementary Figure S9: a) Long molecules are prone to double-threading into the sensing pore while straddling two nanofilter pores. b) Current trace for 3000-bp dsDNA traversing the nanofiltered pore, showing persistent clogging modes corresponding to single- and double-threading through the sensing pore. The clog can be temporarily removed by reversing the applied voltage, but it always quickly returns. Data is low-pass Bessel filtered at 300 kHz and down-sampled to 600 kHz for display purposes.

If both ends of the DNA are fully captured by the sensing pore while the molecule is threaded through two different nanofilter pores, the force will be approximately equal on both strands, resulting in a permanent clog. Reversing the voltage can clear the ends of the strand from the sensing pore temporarily, but is unlikely to be able to remove the tangled strand from the nanofilter due to the low electrical force present at the nanofilter. Since both ends are already in the space between the nanofilter and the sensing membrane, they will find and clog the sensing pore quickly upon re-establishment of the voltage. Data can still be collected on pores clogged in this way by repeatedly switching the polarity of the voltage, though throughput suffers as a result. Alternatively, sensing pores <4nm could be used to prevent capture of two strands and circumvent this clogging mode.

As molecular length continues to increase, the passage time distribution for molecules long enough to sample this clogging mode eventually becomes dominated by multiply-threaded

molecules, and the log-normal portion of the distribution is lost, putting an upper bound on the length of DNA that can be reliably studied with this device for a given gap height.

Supplementary Section S7: Folding Distributions

We have noted that different nanofiltered pores show significantly different proportions of double-threaded events even for a given length of dsDNA. This is presented in Supplementary Figure S10, which shows the folding behavior of molecules passing control pores and nanofiltered pores as a function of both pore diameter and dsDNA length. One of the nanofiltered pores (red circles in Supplementary Figure S10c) completely suppressed folding even though both the pore and the dsDNA chains were large enough to support significant folding.

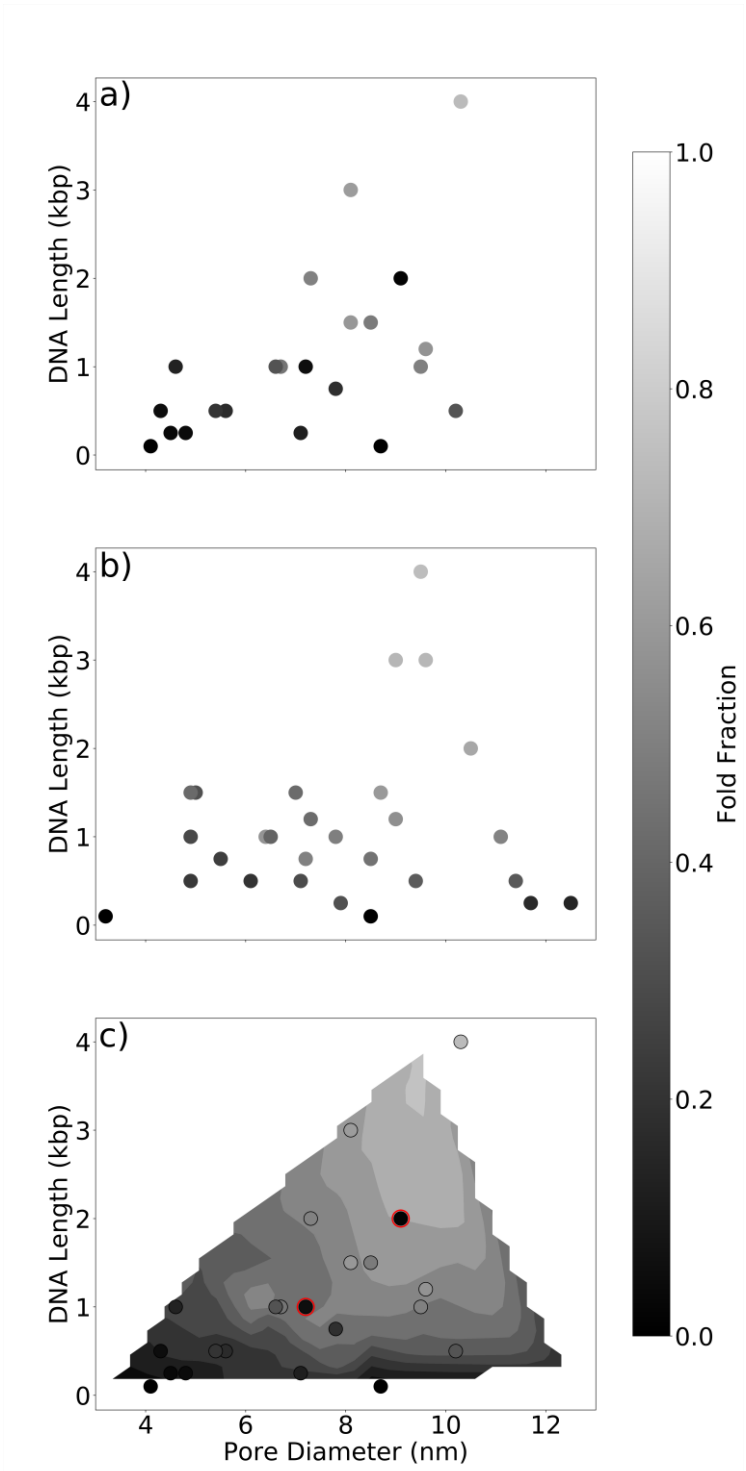

Supplementary Figure S10: a) Folding fraction for nanofiltered pores as a function of pore size and dsDNA length, showing that folding probability increases strongly with chain length and weakly with pore diameter. b) The same plot for control pores. c) Control pores are used to interpolate contours of constant folding fraction, and nanofiltered pores are overlaid as circular symbols. Two symbols, circled in red, stand out as being significantly different from the control case. K478 (see table 1) also showed folding suppression, but is excluded from this plot since data was acquired at a different voltage.

If we assume the nanofilter causes only a weak perturbation to the field and that the electric field $E(\rho,z)$ is cylindrically symmetric and decays as the second power of radial distance from the pore[20], the electric field on the nanofilter a lateral distance ρ from the sensing pore will be roughly

$$E(\rho, h) = \frac{E(0, h)}{1 + \left(\frac{\rho}{h}\right)^2}, \tag{24}$$

where h is the height of the nanocavity. Because passage through the nanofilter is an energy barrier process mediated by the tiny voltage drop present there, the probability of capture by a particular pore in the nanofilter will decrease rapidly with lateral distance from the sensing pore.

Assuming a weak electric field and an energy-barrier-limited passage of polymers through the nanofilter, the capture probability for a particular pore in the nanofilter should be roughly linear in the electric field, and the probability density for capture by a pore in the nanofilter at a lateral distance ρ from the sensing pore will then be proportional to $\rho E(\rho)$, which is strongly peaked near $\rho=h$. Most of the translocations through the sensing pore will therefore be due to passage through pores in the nanofilter which are near the sensing pore. For the nanofilter used in this work, the average number of active pores in the nanofilter (defined as pores within $\rho<h$ of the sensing pore) is 3.4±1.4, so variation in device behavior due to variation in the local porosity of the nanofilter can be quite significant.

In order to further study the effect of the local pore size distribution on the translocation kinetics, we reduced the size of the pores in the nanofilter by depositing hafnia by ALD (160 cycles) on the NPN material prior to membrane transfer. This had the effect of reducing the average pore size from 48±4 nm to 16±4 nm without significantly changing the number of pores per unit area. Supplementary Figure S11 shows TEM imaging of ALD-coated nanofilter pores from a low-porosity section of the wafer. The reduced pore size did not have a significant effect

on folding behavior, again pointing more toward the distance between active pores as the important controlling parameter in suppressing folding.

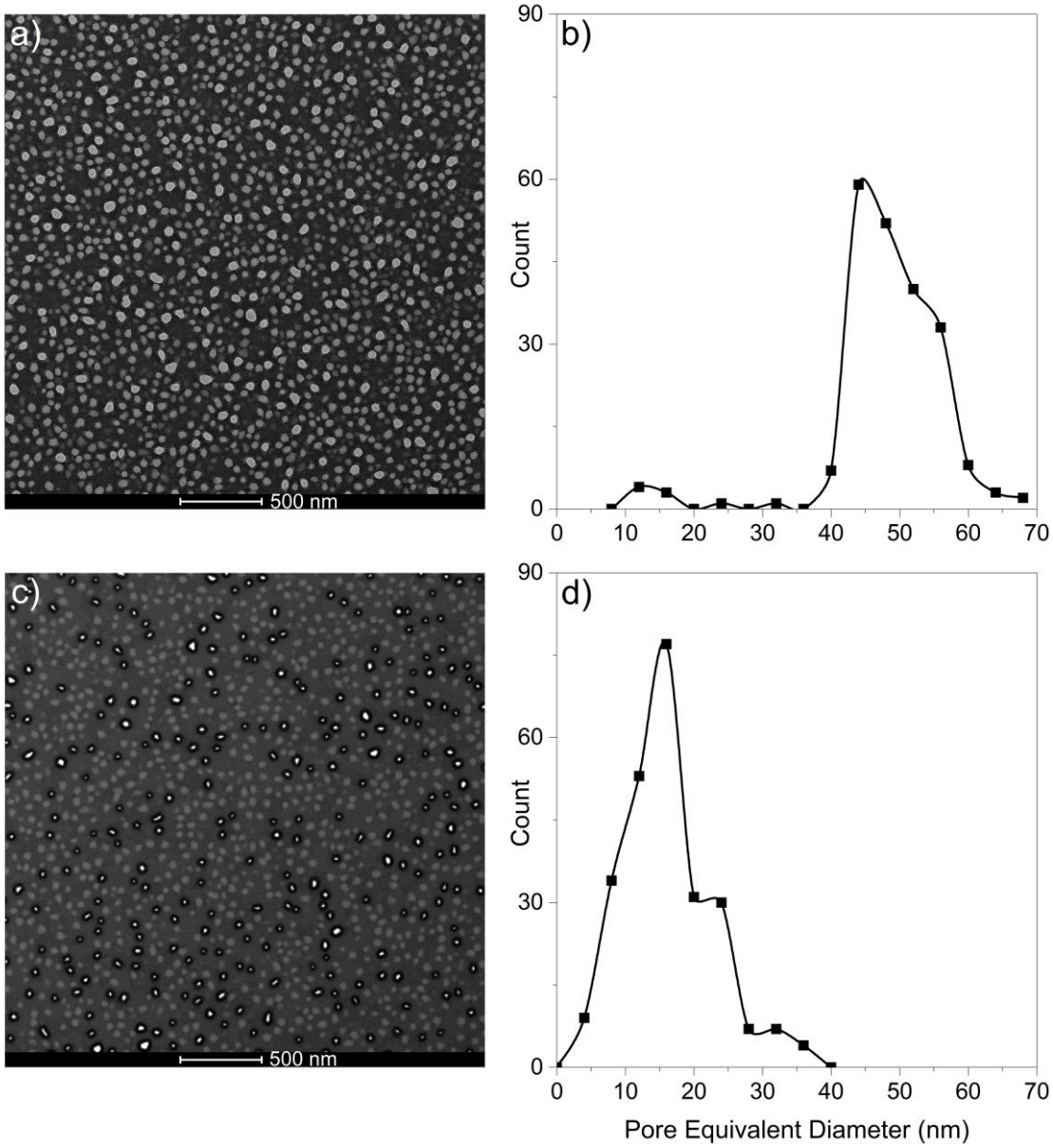

Supplementary Figure S11: ALD coated pore distribution. a) TEM images of NPN material before conformal ALD deposition b) Pore diameter histogram for through holes in the image in a). c) TEM image of a different section of the same NPN wafer after 160 cycles of ALD hafnia deposition. d) Histogram of ALD-coated pore diameters for the through holes, with significant reduction in the average pore diameter. Only through-holes receive a visible ALD coating (black outline).

Unsurprisingly, the smaller pore sizes present in the hafnia-coated nanofilter required a larger applied voltage before translocations were observed. While almost no translocations were

observed at an applied voltage of 200mV, the capture rate at 400mV of ALD-coated nanofiltered pores was comparable to the capture rate of uncoated nanofiltered pores at 200mV. This is simply a consequence of the fact that smaller pores on thicker NPN membranes present a higher energy barrier to translocation. This is especially significant since the reduction in average pore size and the increase in nanofilter membrane thickness would increase the total electrical resistance of the nanofilter, and therefore the voltage drop across it, for a given applied voltage. Since even the uncoated nanofilter already shows size-selectivity properties in the capture rate, we expect that even more dramatic filtering effects will be accessible to nanofiltered systems with significantly smaller average pore size.

Video Legend

Supplementary Video S1: Water vapor swells the nanofilter, which is tented over an array of 200 nm high, 2 μm diameter columns, leaving a ring cavity around each column. Newton's colors form as water vapor is breathed over top of the structure, and are eliminated as the water evaporates in room air.

Supplementary Video S2: Wet nanofilter stability. A wetted nanofilter (0.7 mm x 3 mm) is exposed to repeated menisci in a microfluidic channel.

Supplementary Video S3: A wrinkled nanofilter is torn on meniscus. As the meniscus passes over a wrinkled nanofilter, it is torn away from the substrate and redeposited.

Supplementary Video S4: An illustrative simulation of an $N = 200$ (~3000 bp) polymer translocating through the nanofilter and eventually being captured by the sensing pore.

Supplementary Video S5: An animated schematic description of the fabrication and operation of the complete nanofiltered nanopore device.

References

(1) Briggs, K.; Charron, M.; Kwok, H.; Le, T.; Chahal, S.; Bustamante, J.; Waugh, M.; Tabard-Cossa, V. *Nanotechnology* **2015**, *26*, 84004.

(2) Kowalczyk, S. W.; Grosberg, A. Y.; Rabin, Y.; Dekker, C. *Nanotechnology* **2011**, *22*, 315101.

(3) Beamish, E.; Kwok, H.; Tabard-Cossa, V.; Godin, M. *Nanotechnology* **2012**, *23*, 405301.

(4) Limbach, H. J.; Arnold, A.; Mann, B. A.; Holm, C. *Comp. Phys. Comm.* **2006**, *174*, 704–727.

(5) Slater, G. W.; Holm, C.; Chubynsky, M. V.; de Haan, H. W.; Dube, A.; Grass, K.; Hickey, O. A.; Kingsburry, C.; Sean, D.; Shendruk, T. N.; Zhan, L. *Electrophoresis* **2009**, *30*, 792–818.

(6) Grest, G. S.; Kremer, K. *Phys. Rev. A* **1986**, *33*, 3628–3631.

(7) Stigter, D. *Biopolymers* **1977**, *16*, 1435–1448.

(8) Sobel, E. S.; Harpst, J. A. *Biopolymers* **1991**, *31*, 1559–1564.

(9) Savelyev, A. *Phys. Chem. Chem. Phys.* **2012**, *14*, 2250–2254.

(10) Klotz, A. R.; Duong, L.; Mamaev, M.; De Haan, H. W.; Chen, J. Z. Y.; Reisner, W. W. *Macromolecules* **2015**, *48*, 5028–5033.

(11) Anderson, E.; Bai, Z.; Bischof, C.; Blackford, S.; Demmel, J.; Dongarra, J.; Du Croz, J.; Greenbaum, A.; Hammarling, S.; McKenney, A.; Sorensen, D. *LAPACK Users' Guide*, Third.; Society for Industrial and Applied Mathematics: Philadelphia, PA, 1999.

(12) Farahpour, F.; Maleknejad, A.; Varnik, F.; Ejtehadi, M. R. *Soft Matter* **2013**, *9*, 2750.

(13) Ross, P. D.; Scruggs, R. L. *Biopolymers* **1964**, *2*, 231–236.

(14) Carson, S.; Wilson, J.; Aksimentiev, A.; Wanunu, M. *Biophys. J.* **2014**, *107*, 2381–2393.

(15) Muthukumar, M.; Katkar, H. H. *Biophys. J.* **2015**, *108*, 17–19.

(16) Kwok, H.; Briggs, K.; Tabard-Cossa, V. *PLoS One* **2014**, *9*, e92880.

(17) Bell, N. A. W.; Muthukumar, M.; Keyser, U. F. *Phys. Rev. E* **2016**, *93*, 22401.

(18) Kowalczyk, S. W.; Wells, D. B.; Aksimentiev, A.; Dekker, C. *Nano Lett.* **2012**, *12*, 1038–1044.

(19) Pud, S.; Chao, S.-H.; Belkin, M.; Verschueren, D.; Huijben, T.; van Engelenburg, C.; Dekker, C.;

Aksimentiev, A. *Nano Lett.* **2016**, *16*, 8021–8028.

(20) Wanunu, M.; Morrison, W.; Rabin, Y.; Grosberg, A. Y.; Meller, A. *Nat. Nanotechnol.* **2010**, *5*, 160–165.

Appendix B

Supporting Information for Chapter 4

Supporting Information for

Entropic Trapping of DNA with a Nanofiltered Nanopore

Michelle H. Lam[†ǂ], Kyle Briggs[†ǂ], Konstantinos Kastritis[§ǂ], Martin Magill[§], Gregory R. Madejski[‡], James L. McGrath[‡], Hendrick W. de Haan*[§], and Vincent Tabard-Cossa*[†]

[†] Department of Physics, University of Ottawa, Ottawa, ON, Canada

[‡] Department of Biomedical Engineering, University of Rochester, Rochester, NY, USA

[§] Faculty of Science, University of Ontario Institute of Technology, Oshawa, ON, Canada

[ǂ] These authors contributed equally to this manuscript

*Corresponding Authors: Vincent Tabard-Cossa: tcossa@uOttawa.ca (experiment); Hendrick W. de Haan: Hendrick.deHaan@uoit.ca (simulation).

Table of Contents

Supporting Information Section S1: Simulation Setup

Simulations were used to study the motion of 1.2 kbp DNA in the diffusive mode of operation of the device. An effective multiscale approach was used. In the bulk of the cavity, the DNA was modelled by a single effective particle representing the center of mass of the polymer, and its diffusion was simulated using Brownian dynamics (BD). This model is justified where the dynamics occur on length scales much larger than the radius of gyration of the molecule. Near the filter, however, the dynamics of the entire polymer chain become important and a Brownian particle cannot faithfully model the polymer. In this region, the DNA was modelled as a wormlike chain, coarse-grained Langevin dynamics (CGLD) was used to simulate its motion. In the following sections we provide more detail on the simulations.

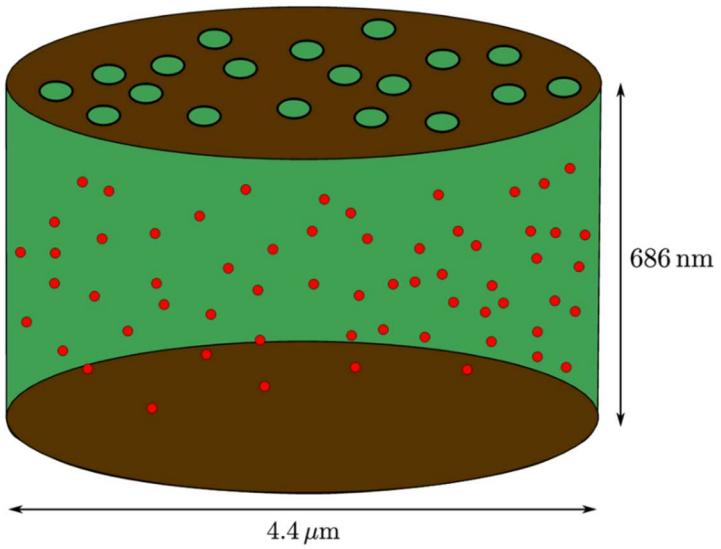

Figure S1: Schematic of the geometry used for the Brownian dynamics simulations. The effective dimensions for the gap height and cavity diameter are shown. The nominal dimensions for the cavity diameter and gap height were 4.5 μm and 800 nm respectively. The red dots represent the Brownian particles. To account for the fact that modelled polymers are treated as extended object, twice the radius of gyration, $2R_g$ ($R_g \approx 57$ nm), was subtracted from each of the dimensions resulting in a cavity diameter of 4.4 μm and a gap height of 686 nm.

Modelling the dynamics far from the filter

Polymer model

To carry out the simulation we used the HOOMD-blue molecular dynamics software package. Far from the filter we only considered the center of mass (COM) motion of the polymer. We modelled the COM as a single particle whose time evolution is given by Brownian dynamics (BD):

$$\dot{\vec{x}} = \sqrt{2D}\vec{\xi}(t), \tag{1}$$

where D is the diffusion coefficient and $\vec{\xi}(t)$ is a Gaussian random noise function. This model has a single free parameter, the diffusion coefficient. We expressed lengths in the BD simulations in units of nanometers (nm), and fixed the diffusion coefficient to be

$$D_{sim} = 1\frac{\mathrm{nm}^2}{\tau_{\mathrm{BD}}}, \tag{2}$$

where τ_{BD} is the simulation unit of time. Experimentally measured diffusion coefficients were used to determine the equivalent value of τ_{BD} in seconds. For a given experimental diffusion coefficient $D_{exp}(L_c)$ (which generally depends on the contour length, L_c), we set

$$1\frac{\mathrm{nm}^2}{\tau_{\mathrm{BD}}} = D_{sim} = D_{exp} = D_{exp}(L_c)\frac{\mathrm{nm}^2}{s}, \tag{3}$$

from which we determine

$$\tau_{\mathrm{BD}} = \frac{1}{D_{exp}(L_c)}s. \tag{4}$$

The numerical values of the diffusion coefficient were obtained from Petrov *et al*[1].

In order to probe the long times present in the experiment the time step was set to $\Delta t = 10\tau$. This choice of time step sets the mean jump size to be $\Delta x \approx 4$ nm, a value which is reasonable far from the filter as it is much smaller than even the smallest length in the device which stands at ≈ 700 nm (Figure S1).

Geometry

Figure S1 shows the geometry of the device assumed for the simulations described in this section. The nominal dimensions of the device were 4.5 μm and 800 nm for the cavity diameter and gap height respectively. To account for the fact that a polymer is an extended object we subtracted $2R_g$ ($R_g \approx 57$ nm) from each of the dimensions resulting in a cavity diameter of 4.4 μm and a gap height of 686 nm. The cavity walls were modelled as reflecting boundaries, with the trajectory of a particle that would cross the wall being reflected back into the cavity.

For the sensing pore membrane we assumed that the molecules cannot escape back into the loading well and thus modelled it as a reflecting boundary similar to the cavity walls. As such, the sensing pore itself was not explicitly incorporated in the boundary condition. However, the location of the sensing pore, which we assumed to be at the center of the membrane, dictated the initial condition for the particles in the simulation. The nanofilter membrane was treated as a special boundary condition described in the next subsection.

Interactions with the filter pores

As the dynamics near the filter are more complicated than simple diffusion in the bulk of the cavity, the results of the more detailed CGLD simulations were coupled to the BD simulations via a special boundary condition. The majority of the filter membrane was modelled as a reflecting

boundary with certain locations on its surface being absorbing windows, representing pores in an otherwise impermeable membrane. Upon interaction with an absorbing window a particle has a probability of escaping through the filter. The details of obtaining the probability of escape through a filter pore are discussed in the next section.

A randomly generated nanofilter was used in order to account for the inherent variability in the filter pore distribution. The absorbing windows were placed iteratively. Trial pore locations were drawn uniformly with the criteria that the window corresponding to any new pore has an edge-to-edge distance of at least 20 nm from any existing window. In addition, the center of all pores was required to be at least one pore radius away from the edge of the membrane. Pore locations that did not meet these criteria were discarded.

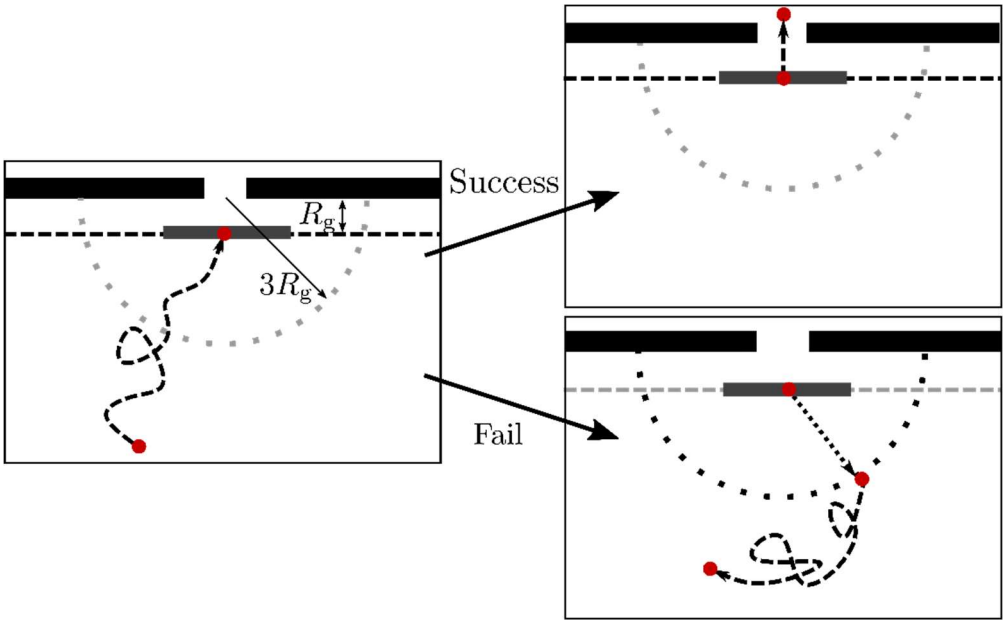

Figure S2: Schematic of the filter interaction for the Brownian particles. The grey rectangle represents a cross section of the disk of interaction for the pore. The black dashed line represents the excluded region of R_g from the pore. The black dotted line represents the rejection radius at $3R_g$.

Simulation procedure

We implicitly modelled the loading of the molecules into the cavity by initializing two thousand non-interacting particles into the cavity at a distance of R_g from the center of the sensing pore membrane. The simulations were run for 30 seconds according to the time mapping described in the previous subsection. For each filter pore size a total of ten different filter configurations were sampled.

As shown in Figure S2, a particle is determined to be near a filter pore in the boundary when it lies inside a disk with origin at the central axis of the pore and radius equal to two times the pore radius, displaced a distance R_g axially from the nanofilter pore. Upon interaction of a particle with a pore on the filter a random number is drawn, and if it less than the probability obtained from CGLD the particle successfully translocates. If not, it is returned to the bulk of the cavity by being placed at a random location on a hemisphere $3R_g$ radially away from the center of the nominal pore.

We modelled the recapture of molecules implicitly by assuming that all polymers remaining in the cavity at the end of the simulation would be successfully recaptured. The probability of recapture shown in Figure 3e of the main text was computed as

$$P_\tau(t) = 1 - \frac{N_{escaped}}{N_{initialized}} \tag{5}$$

Modelling the dynamics near the filter

Polymer model

As mentioned in the preceding section, near the nanofilter the DNA was modelled using a wormlike chain comprised of N identical monomers. To model the time evolution of the polymeric chain we used coarse-grained Langevin dynamics (CGLD)[2] in which monomers are taken to be spheres that experience Stokes drag and whose solvent interactions are implicit. The equation of motion for CGLD is

$$m\ddot{\vec{x}} = -\sum_i \nabla U_i(\vec{x}) - \zeta\dot{\vec{x}} + \sqrt{2\zeta k_B T}\vec{\xi}(t), \tag{6}$$

where ζ is the drag coefficient and $k_B T$ is the thermal energy. The fluctuation term $\vec{\xi}(t)$ is a random noise function that implicitly models thermal fluctuations in the solvent and satisfies

$$\langle\vec{\xi}(t)\rangle = 0, \tag{7}$$

$$\langle\xi_i(t)\xi_j(t')\rangle = \delta_{ij}\delta(t-t'). \tag{8}$$

The gradient term is the sum of all external forces. To evolve the equation in time we used the HOOMD-blue molecular dynamics package.[3,4]

Bonds between pairs of adjacent monomers were modelled using the finitely extensible non-linear elastic potential,

$$U_{FENE}(r) = -\frac{1}{2}kr_{max}^2 \ln\left(1 - \frac{r^2}{r_{max}^2}\right). \tag{9}$$

The constants k and r_{max} represent the stiffness and the maximum possible extension of the bond respectively, with r being the center to center distance between monomers. The excluded volume interaction between monomers was modelled using the Weeks-Chandler-Anderson (WCA) potential,

$$U_{WCA}(r) = \begin{cases} 4\varepsilon\left[\left(\frac{\sigma}{r}\right)^{12} - \left(\frac{\sigma}{r}\right)^{6}\right] + \varepsilon, & r < r_c \\ 0, & r \geq r_c \end{cases} \quad (10)$$

where ε is the interaction energy, σ the monomer diameter and $r_c = 2^{\frac{1}{6}}\sigma$ the cut-off distance.

To model the rigidity inherent to the DNA we used a three-body harmonic potential,

$$U_{angle}(\theta) = \frac{1}{2}k_{angle}\theta^2, \quad (11)$$

where k_{angle} is the stiffness of the spring and θ is the angle formed between three consecutive monomers along the chain.

The simulations used a self-consistent set of units with energy, mass, and distance as fundamental units. All other units were derived from these. The unit of energy was chosen to be the thermal energy k_BT with the units of length and mass chosen as the particle size σ and mass m respectively.

The units of time in this system are given by $\tau = \sigma\sqrt{\frac{m}{k_BT}}$. In accordance with Grest *et al*.,[5] the parameters of the FENE potential were chosen to be $k = 30\frac{k_BT}{\sigma^2}$ and $r_{max} = 1.5\sigma$. The persistence length of the polymer is $l_p \approx \frac{k_{angle}}{k_BT}\sigma$,[6] so that changing the stiffness of the angle bond changes the persistence length.

We set the correspondence between simulation lengths and experimental lengths by choosing the effective monomer diameter, σ, to equal 5 nm. The persistence length of the polymer in the simulations was set to match that of DNA in 4 M LiCl (30 nm, 6σ).[7,8] The drag coefficient ζ, although not a fundamental unit, was also set to unity.

Geometry

For these simulations we modelled a filter pore as a cylindrical hole with WCA interactions creating an effective pore in the membrane. Although the domain of the simulation is unbounded, a hemisphere of radius 3Rg centered at the mouth of the pore, as shown in Figure S2, prevented the center of mass from diffusing any further. We kept the effective thickness of the pore fixed at 10σ (50 nm) to match experiment and varied the radius in the range $4\sigma \leq r_p \leq 10\sigma$. A caveat of this approach is that the simulated pores have circular cross sections rather than the various different cross sections present in the nanofilter pore distribution. The pore diameters used in the simulations correspond to pore major axis lengths in the experiment.

Simulation procedure

In the diffusive mode of operation, no electric field is applied to the system, so DNA strands that escape during the trapping time do so via unbiased translocation. Such events occur rarely, even for polymers very close to the nanopore. As such, we considered the question: given a polymer that has diffused near a filter pore, what is the probability that it will translocate through that pore before diffusing a significant distance away?

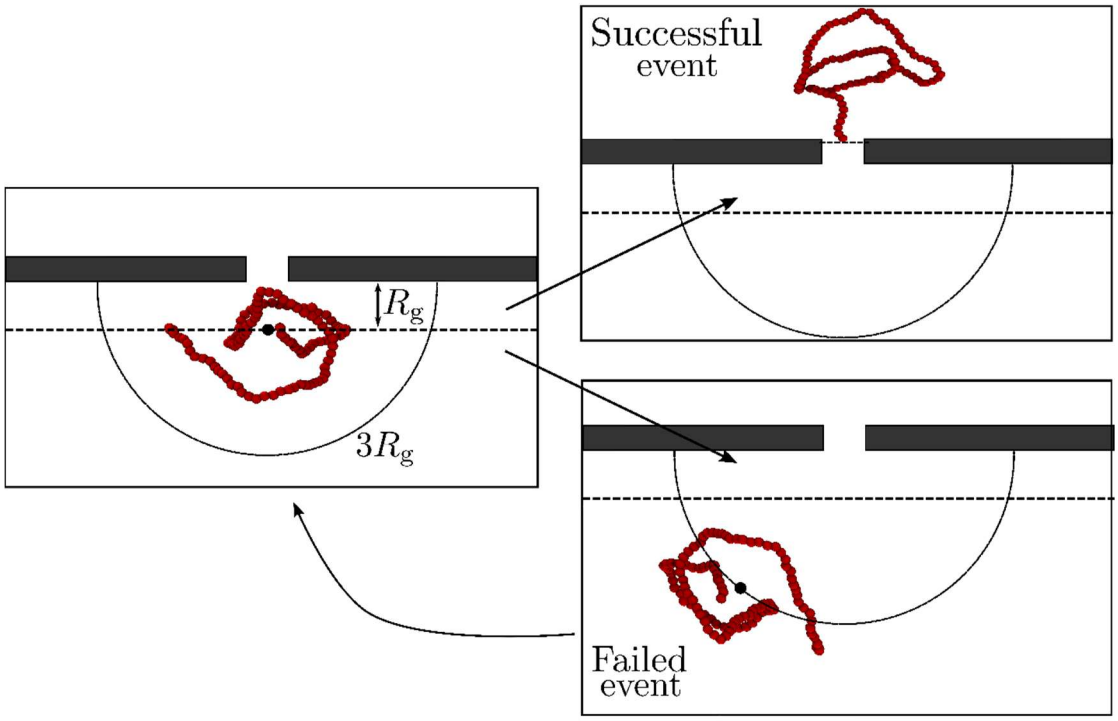

Figure S3: Schematic of the simulation geometry and procedure. The black dot represents the center of mass of the polymer. The black dashed line represents the initial distance from the pore membrane, and the black solid line represents the cutoff distance for the COM.

To compute these probabilities polymers were initialized with their center of mass on a disk that is R_g away axially from the mouth of the pore. The polymer either successfully translocates, classifying the event as a success, or diffuses away. An event was considered to have failed when the center of mass of the chain diffused further than $3R_g$ radially from the mouth of the pore.

At initialization the polymers should have equilibrium conformations, as prior to approaching the filter there is ample time to fully equilibrate. In the simulations the equilibration of a chain takes a considerable amount of computational time. Given that we expect a lot of failed events, equilibrating the chain in the same simulation as the translocation events would quickly

render the problem computationally infeasible. As such, we generated a database of five thousand equilibrium conformations that were used for initializing the polymers.

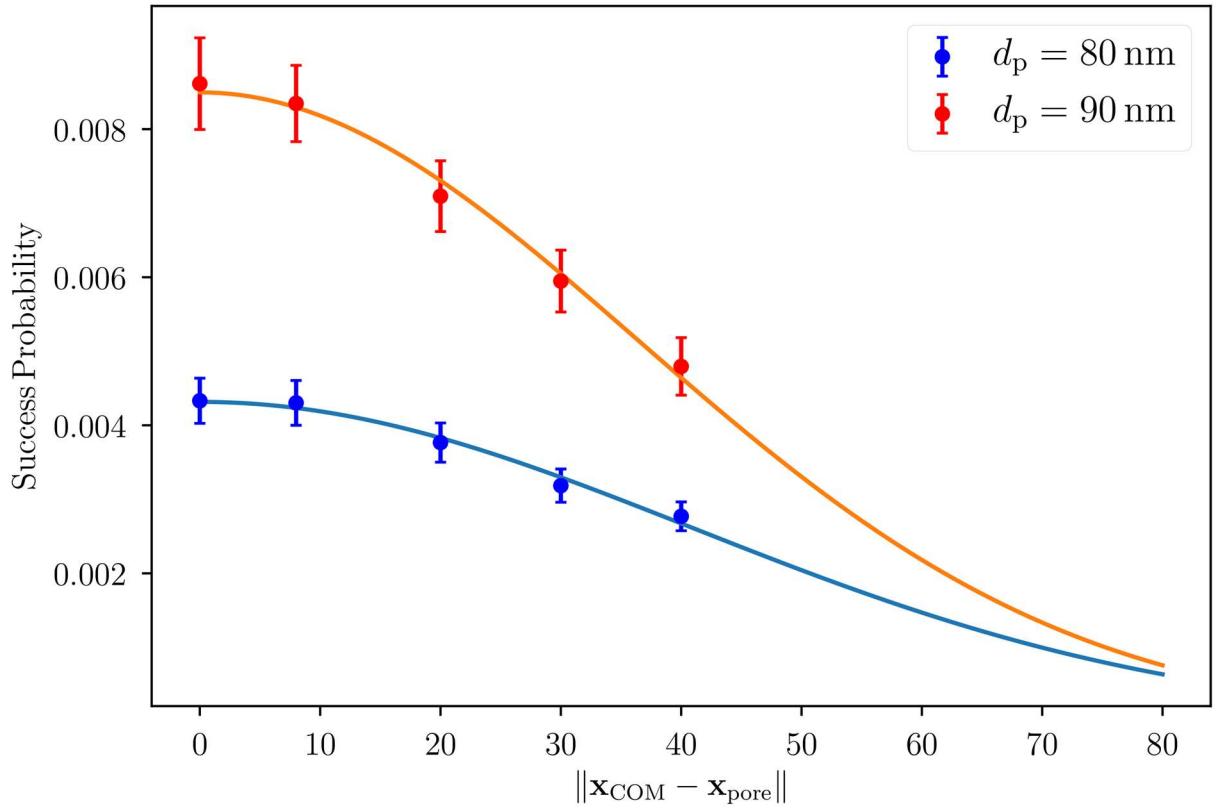

Figure S4: Success probability as a function of initial distance from the central axis of the nanopore to the COM. The solid lines are the fits to the data. The fit parameters can be found in Table S1.

When feasible, simulations were run for two hundred successful events for all pore radii. However, given the infrequency of successful events at smaller pores that was not always possible. As such, instead of running for a set number of successful events, some pore sizes were run for a set number of failures, as displayed in Figure 4 of the main text. The probability of escape through the pore was computed as the number of successful events divided by the total number of events,

$$P_e = \frac{n_{successes}}{n_{failures} + n_{successes}} \tag{12}$$

As shown in Figure S4, we found that as we varied the initial axial offset of the COM on the disk, the variations in the probabilities were well fit by a Gaussian function of the form

$$p_{fit}(r) = a_0 \exp\left[-\left(\frac{r}{a_1}\right)^2\right], \tag{13}$$

where a_0 and a_1 are fit parameters, shown in the Table S1. Note that for diameters of 70 and 100 nm, we only changed a_0 to be the on-axis probability and did not change a_1. As a result, when coupling CGLD to BD, we were able to compute the probability of escape through a pore after the COM had interacted with any point in a disk around the pore. It was this result that led to our choice for the disk radius described in the preceding section.

Table S1: Fit parameters for the success probability.

$\sigma = 5$ nm		
d_p (nm)	a_0	a_1
70 (*)	0.00295832	1.44520178
80	0.00431574	1.44520178
90	0.00849688	1.28618592
100(*)	0.01259953	1.28618592

The half-life of M13

Simulations were also used to gain some insight on the effectiveness of the nanofiltered nanopore device as a trap for M13. Given the size of M13 (7 kbp), conducting similar simulations to those described in the preceding sections would be infeasible. As a result, instead of simulating M13, we simulated the longest chains we feasibly could and extrapolated to obtain a conservative estimate of the trapping time for M13.

With the length scale chosen for the model described in the previous sections simulating polymers longer than 2 kbp becomes computationally challenging as the number of monomers becomes very large. As such, we modified the length correspondence by choosing the monomer size to be $\sigma = 10$ nm. The most salient effect of this change is that all the lengths in simulation units were halved, including the effective dimensions the nanopore. Given that all the simulations lengths were modified, we repeated the CGLD simulations explained in the previous section to obtain the probabilities of translocation, as shown in Figure S5.

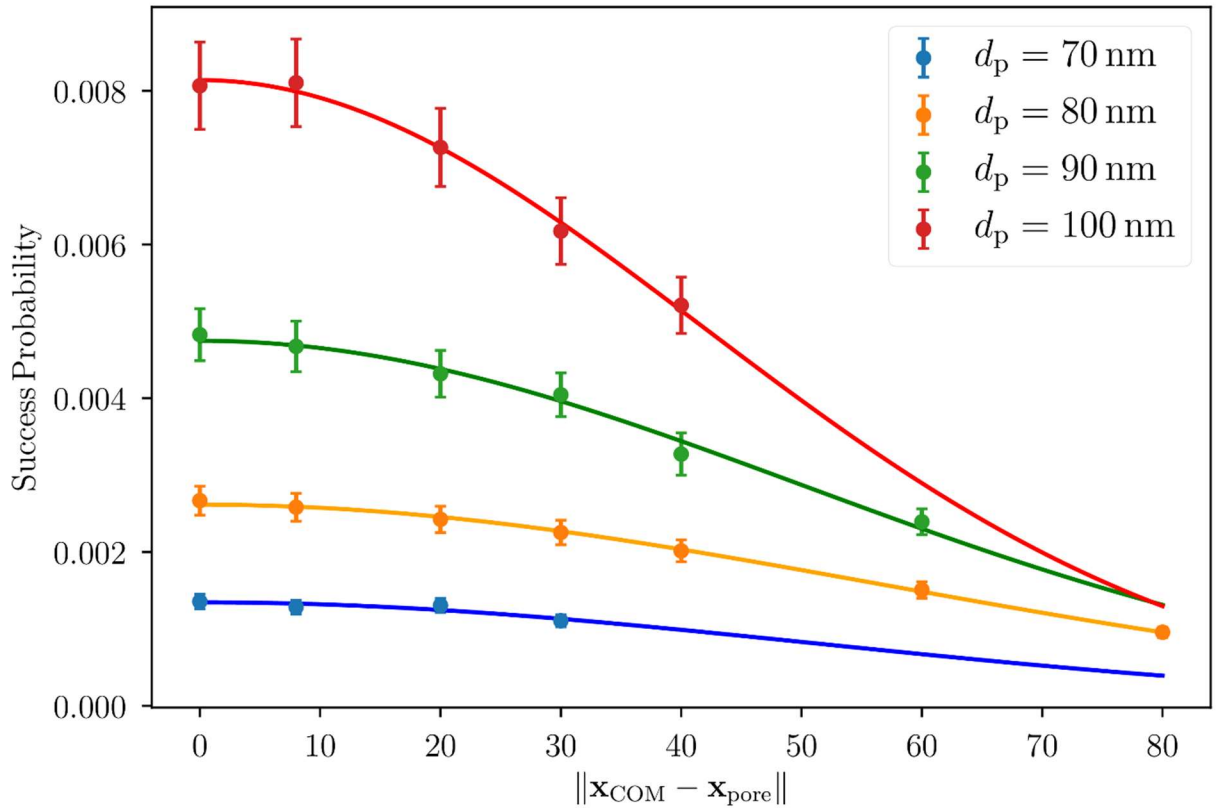

Figure S5: Success probability for a different length correspondence to Figure S4.

Table S2: Fit parameters for the success probability using $\sigma = 10$ nm.

d_p (nm)	a_0	a_1
70	0.00134558	1.79900229
80	0.00261617	1.99259571
90	0.00474791	1.76365758
100	0.00813947	1.47562624

The different length correspondence allowed us to use CGLD to simulate longer chains. Using the methodology described in the previous section we conducted BD simulations for 1.2 kbp, 1.5 kbp, 2.2 kbp, 2.9 kbp, and 3.7 kbp.

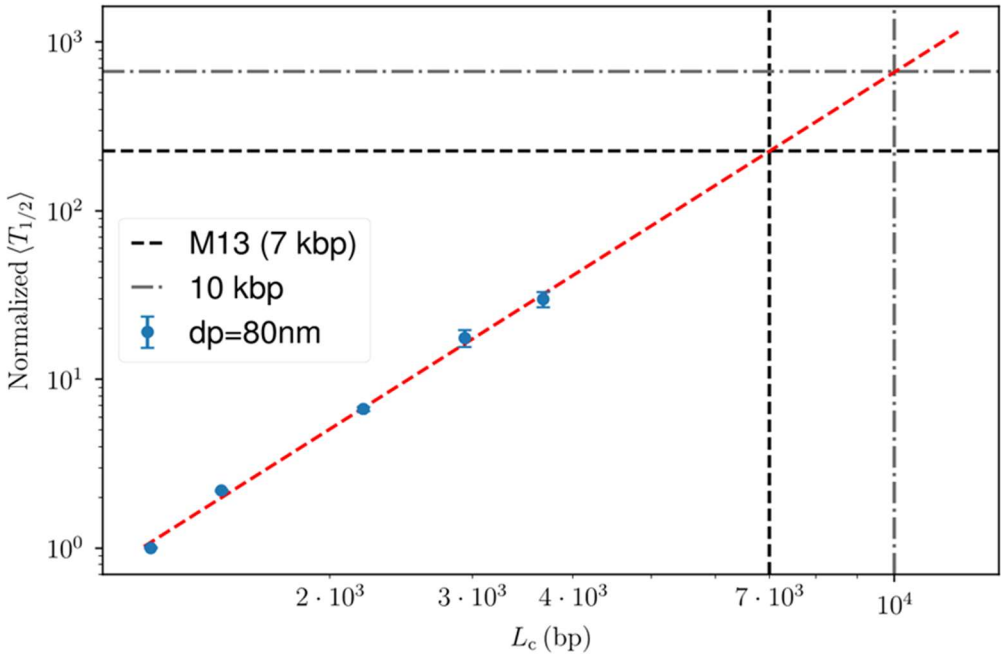

Figure S6: Normalized time for half the molecules to escape the device. The values are normalized by the value at L_c = 1.2 kbp as that is the only value for which both experimental and simulation results are available. The red dashed line is a power law fit to data with the exponent being 3.0238.

Figure S6 shows the half-life is well fit by a power law at the polymer lengths simulated. By extrapolating the fit to the length of M13 and 10 kbp we estimated the half-life to be 230 and 670 times longer than that of 1.2 kbp, respectively. Given that the half-life for 1.2 kbp is around 10 seconds, the half-life for M13 would be ≈40 minutes. This estimated time is in agreement with the experimental results, where virtually no escape events were recorded within 30 seconds of waiting.

Supporting Information Section S2: Effective Pore Diameter Distribution

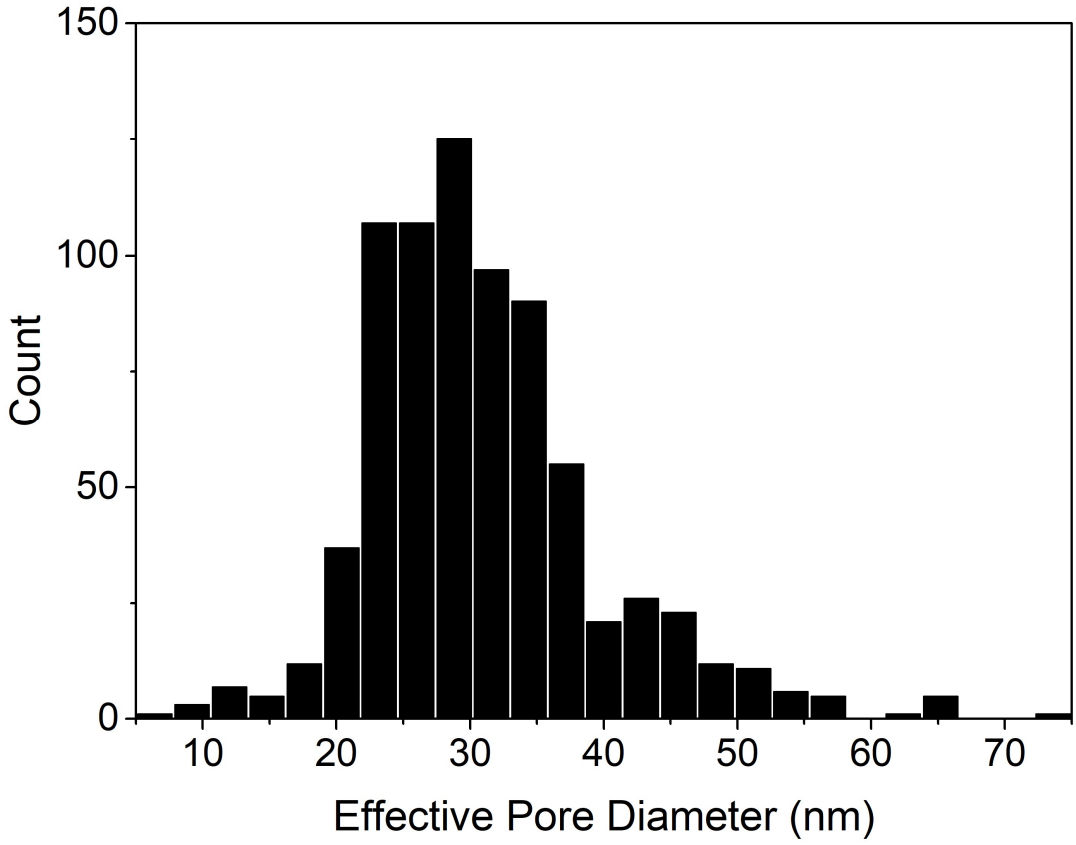

Figure S7: The distribution of effective pore diameter distribution, estimated as the geometric mean of the major and minor axes of the fitting ellipse.

Supporting Information Section S3: Additional Event Traces

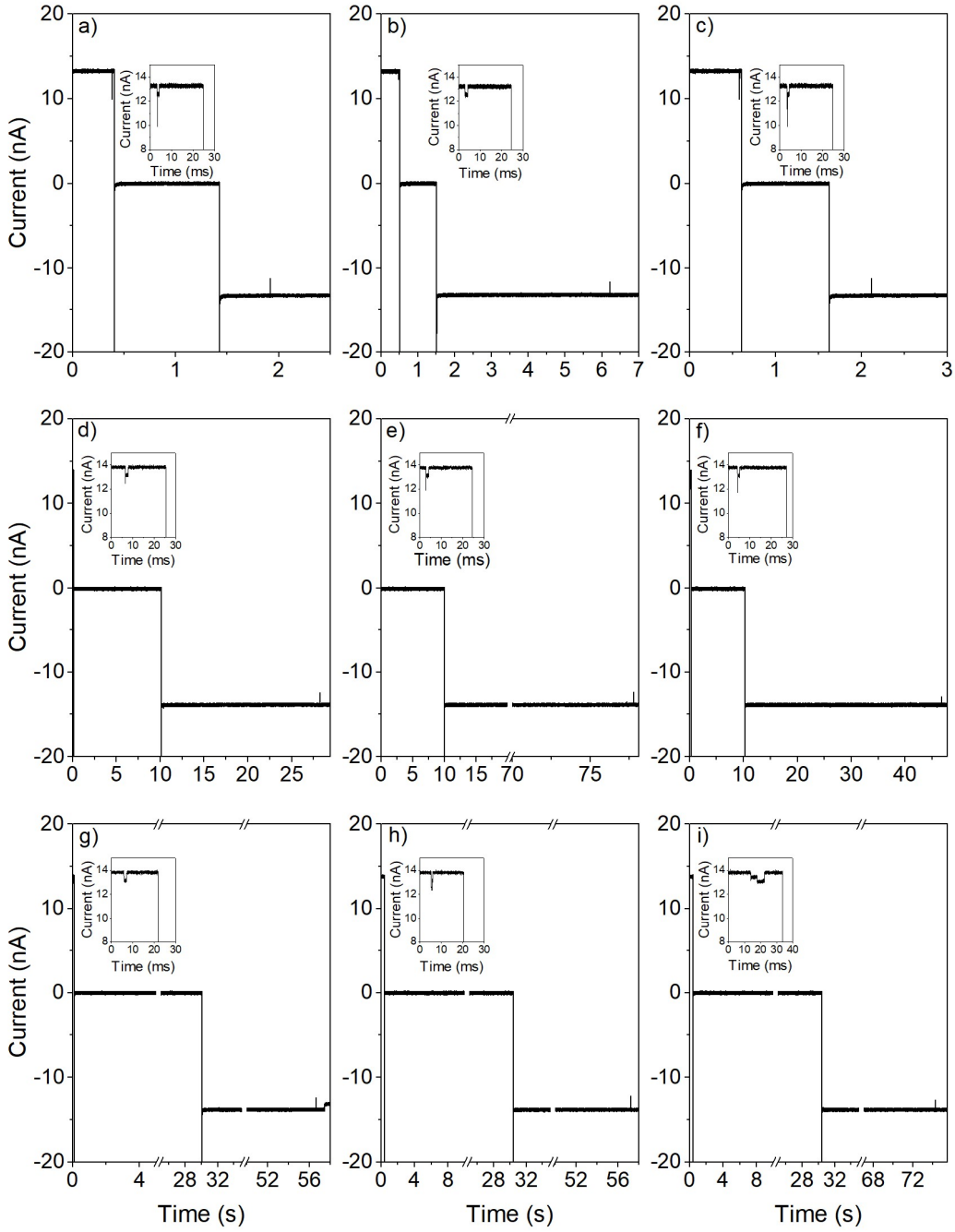

Figure S8: Additional single-molecule 10 kbp DNA trapping events in the diffusive mode for (a-c) 1s delay times, (d-f) 10s delay times, and (g-i) 30s delay times using Device C from the main text. Insets show the loading events. Note axis breaks in some cases where delay times are long.

References

(1) Petrov, E. P.; Ohrt, T.; Winkler, R. G.; Schwille, P. Diffusion and Segmental Dynamics of Double-Stranded DNA. *Phys. Rev. Lett.* **2006**, *97* (25), 258101. https://doi.org/10.1103/PhysRevLett.97.258101.

(2) Slater, G. W.; Holm, C.; Chubynsky, M. V.; de Haan, H. W.; Dube, A.; Grass, K.; Hickey, O. A.; Kingsburry, C.; Sean, D.; Shendruk, T. N.; et al. Modeling the Separation of Macromolecules: A Review of Current Computer Simulation Methods. *Electrophoresis* **2009**, *30* (5), 792–818. https://doi.org/10.1002/elps.200800673.

(3) Glaser, J.; Nguyen, T. D.; Anderson, J. A.; Liu, P.; Spiga, F.; Millan, J. A.; Morse, D. C.; Glotzer, S. C. Strong Scaling of General-Purpose Molecular Dynamics Simulations on GPUs. *Comput. Phys. Commun.* **2015**, *192*. https://doi.org/10.1016/j.cpc.2015.02.028.

(4) Anderson, J. A.; Lorenz, C. D.; Travesset, A. General Purpose Molecular Dynamics Simulations Fully Implemented on Graphics Processing Units. *J. Comput. Phys.* **2008**, *227* (10), 5342–5359. https://doi.org/10.1016/j.jcp.2008.01.047.

(5) Grest, G. S.; Kremer, K. Molecular Dynamics Simulation for Polymers in the Presence of a Heat Bath. *Phys. Rev. A* **1986**, *33* (5), 3628–3631. https://doi.org/10.1103/PhysRevA.33.3628.

(6) Landau, L. D.; Lifshitz, E. M.; Sykes, J. B.; Reid, W. H. Course of Theoretical Physics. In *Vol. 7 Theory of Elasticity*; Elsevier, 2013.

(7) Sobel, E. S.; Harpst, J. A. Effects of Na+ on the Persistence Length and Excluded Volume of T7 Bacteriophage DNA. *Biopolymers* **1991**, *31* (13), 1559–1564. https://doi.org/10.1002/bip.360311311.

(8) Savelyev, A. Do Monovalent Mobile Ions Affect DNA's Flexibility at High Salt Content? *Phys. Chem. Chem. Phys.* **2012**, *14* (7), 2250. https://doi.org/10.1039/c2cp23499h.

Appendix C

Nanopore in HOOMD-blue

The nanopore in the simulations was implemented using the framework that HOOMD-blue provides for adding external potentials to the package. As mentioned in the introduction, the nanopore was constructed with WCA potentials. The code below is the header file that gets used by cuda and the internal constructors of HOOMD to apply the external potential to all particles in the simulated system.

In brief, the geometry of the nanopore is that of a cylindrical exclusion in a planar membrane. The walls of the nanopore were modelled using WCA potentials. The potentials were used to define regions of interaction for the particles in the simulation. Once a particle was within these pre-defined regions, the interactions would occur. Outside of these regions, there is no interaction with the nanopore. In other words, it is as if the geometry of the pore is constructed from the same particles as the ones in the simulation, and so once the particle of interest approaches the nanopore the number of interactions becomes rather large and creates overhead the calculations. However, unlike the case where the pore is explicitly constructed with particles, only one interaction needs to be computed with this code.

In addition to the nanopore, the electric field used in Chapter 2 was also imple-

mented in HOOMD. The implementation of the electric field is more straightforward. We make the transformation from oblate spheroidal coordinates to cartesian and then use the particle positions to compute the electric field. The force then informs the update on the particle positions.

The validity of these implementation was tested by running simulations and checking for invalid behaviour, such as particles entering the walls of the nanopore, or being ejected from the simulation upon touching the walls. For the electric field, since we have an analytic form (as given in Chapter 2), we tested whether or not particles moved according to the field lines, as they should in the absence of any thermal motion.

Listed below is the code for the nanopore and the code for the electric field.

```
1
2
3  #ifndef __EVALUATOR_PORE_FIELD_H__
4  #define __EVALUATOR_PORE_FIELD_H__
5
6  #ifndef NVCC
7  #include <string>
8  #endif
9
10 #include <math.h>
11 #include "hoomd/HOOMDMath.h"
12 #include "hoomd/BoxDim.h"
13
14 /*! \file EvaluatorPoreField.h
15     \brief Defines the external potential evaluator to construct a
    nanopore from repulsive interactions
16 */
17
```

```
18 // need to declare these class methods with __device__ qualifiers
       when building in nvcc
19 // DEVICE is __host__ __device__ when included in nvcc and blank
       when included into the host compiler
20 #ifdef NVCC
21 #define DEVICE __device__
22 #else
23 #define DEVICE
24 #endif
25
26 //! Class for evaluating nanopore field
27 /*! <b>General Overview</b>
28     Using WCA potentials to define repulsive interactions between
       particles and nanopore walls
29 */
30 class EvaluatorPoreField
31     {
32     public:
33
34         //! type of parameters this external potential accepts
35         typedef Scalar4 param_type;
36         typedef Scalar3 field_type;
37
38         //! Constructs the constraint evaluator
39         /*! \param X position of particle
40             \param box box dimensions
41             \param params per-type parameters of external potential
42         */
43         DEVICE EvaluatorPoreField(Scalar3 X, const BoxDim& box,
       const param_type& _params, const field_type& field)
44             : m_pos(X),
```

```
45              m_box(box),
46              m_field(field), lj1(_params.x), lj2(_params.y), rpore(
    _params.z), tpore(_params.w)
47          {
48          }
49
50      //! Nanopore doesn't need diameters
51      DEVICE static bool needsDiameter() { return false; }
52      //! Accept the optional diameter value
53      /*! \param di Diameter of particle i
54      */
55      DEVICE void setDiameter(Scalar di) { }
56
57      //! Nanopore doesn't need charges
58      DEVICE static bool needsCharge() { return true; }
59      //! Accept the optional diameter value
60      /*! \param qi Charge of particle i
61      */
62      DEVICE void setCharge(Scalar qi) { m_qi = qi; }
63
64      DEVICE static bool requestFieldVirialTerm() { return true; }
65
66      //! Evaluate the force, energy and virial
67      /*! \param F force vector
68          \param energy value of the energy
69          \param virial array of six scalars for the upper
    triangular virial tensor
70      */
71      DEVICE void evalForceEnergyAndVirial(Scalar3& F, Scalar&
    energy, Scalar* virial)
72          {
```

```
73
74
75              Scalar cx = m_pos.x - m_field.x;
76              Scalar cy = m_pos.y - m_field.y;
77              Scalar cz = m_pos.z - m_field.z;
78              Scalar rxy = sqrt(cx*cx + cy*cy);
79
80
81
82              // WCA parameters
83
84
85              Scalar rtop ;
86              Scalar rbot ;
87
88              Scalar rtop2;
89              Scalar rbot2;
90
91              Scalar rtop2inv;
92              Scalar rbot2inv;
93
94              Scalar WCAforcemag = Scalar(0.0);
95
96              // WCA Cutoff
97              Scalar rcut = 1.12246204831;
98
99              // Inter-pore parameters
100             Scalar theta;
101             Scalar htpore = tpore*0.5;
102             Scalar zmax = htpore + rcut;
103             Scalar rxy2 = (rxy-rpore)*(rxy-rpore);
```

```
104             Scalar rxy2inv = Scalar(1.0)/rxy2;
105             Scalar rxy6inv = rxy2inv * rxy2inv * rxy2inv;
106             Scalar phi;
107             Scalar R2inv;
108             Scalar R6inv;
109             Scalar Fmag;
110             Scalar R2;
111
112
113
114
115             // Force initialization
116             F.x = 0;
117             F.y = 0;
118             F.z = 0;
119             Scalar Ftheta;
120
121             if (rxy <= rpore-rcut){
122                 F.x = 0;
123                 F.y = 0;
124                 F.z = 0;
125
126             } else if (abs(cz) >= zmax ){
127                     F.x = 0;
128                     F.y = 0;
129                     F.z = 0;
130                     } else if (rxy >= rpore && abs(cz) >= htpore) {
131
132                     if (cz > 0) {
133                         rtop = cz - (htpore);
134                         rtop2 =rtop*rtop;
```

```
135                         rtop2inv = Scalar(1.0)/rtop2;
136                         Scalar rtop6inv= rtop2inv*rtop2inv*rtop2inv;
137                         WCAforcemag = rtop*rtop2inv * rtop6inv * (
    Scalar(12.0)*lj1*rtop6inv - Scalar(6.0)*lj2);
138                         F.x = F.y = 0;
139                         F.z = WCAforcemag;
140                     } else {
141                         rbot = cz + (htpore);
142                         rbot2 =rbot*rbot;
143                         rbot2inv = Scalar(1.0)/rbot2;
144                         Scalar rbot6inv= rbot2inv*rbot2inv*rbot2inv;
145                         WCAforcemag = rbot*rbot2inv * rbot6inv * (
    Scalar(12.0)*lj1*rbot6inv - Scalar(6.0)*lj2);
146                         F.x = F.y = 0;
147                         F.z =  WCAforcemag;
148                     }
149 
150                 } else if (abs(cz) <= htpore  && rxy > rpore - rcut)
    {
151                         theta = atan2(cy,cx);
152 
153                          Ftheta = (rxy-rpore)*rxy2inv * rxy6inv * (
    Scalar(12.0)*lj1*rxy6inv - Scalar(6.0)*lj2);
154                          F.z = 0 ;
155                          F.x = Ftheta*cos(theta);
156                          F.y = Ftheta*sin(theta);
157 
158                 } else if (abs(cz) >= htpore && rxy > rpore -rcut) {
159 
160                 theta = atan2(cy,cx);
161                 Scalar rxycorner = sqrt((cx-rpore*cos(theta))*(cx-
```

```
rpore*cos(theta)) + (cy-rpore*sin(theta))*(cy-rpore*sin(theta)));
162             R2 = (rxycorner)*(rxycorner) + ((abs(cz)-htpore))*((
abs(cz)-htpore));
163
164                 if (R2 <= rcut*rcut){
165                     R2inv = Scalar(1.0)/R2;
166                     R6inv = R2inv*R2inv*R2inv;
167                     Fmag  = sqrt(R2)*R2inv * R6inv * (Scalar
(12.0)*lj1*R6inv - Scalar(6.0)*lj2);
168
169
170
171                     if (cz >= 0) {
172                         phi = atan2(cz - htpore,rxycorner);
173                         F.x = -Fmag*cos(phi)*cos(theta);
174                         F.y = -Fmag*sin(theta)*cos(phi);
175                         F.z = Fmag*sin(phi);
176                     } else {
177                         phi = atan2(cz + htpore,rxycorner);
178                         F.x = -Fmag*cos(phi)*cos(theta);
179                         F.y = -Fmag*sin(theta)*cos(phi);
180                         F.z = Fmag*sin(phi);
181
182                     }
183                 } else { F.x = F.y= F.z= 0 ;}
184             }
185         }
186
187
188     #ifndef NVCC
189     //! Get the name of this potential
```

```
190         /*! \returns The potential name. Must be short and all
    lowercase, as this is the name energies will be logged as
191             via analyze.log.
192         */
193         static std::string getName()
194             {
195             return std::string("nanopore");
196             }
197         #endif
198
199     protected:
200         Scalar3 m_pos;                  //!< particle position
201         BoxDim m_box;                   //!< box dimensions
202         Scalar m_qi;                    //!< particle charge
203         Scalar3 m_field;                //!< the field vector
204         Scalar lj1;                     //!< lj1 parameter extracted
    from the params passed to the constructor
205         Scalar lj2;                     //!< lj2 parameter extracted
    from the params passed to the constructor
206         Scalar rpore;                   //!< Radius of Pore
207         Scalar tpore;                   //!< Thickness of Pore
208     };
209
210
211 #endif // __EVALUATOR_PORE_FIELD_H_
```

```
1
2
3 #ifndef __EVALUATOR_EFIELD_H__
4 #define __EVALUATOR_EFIELD_H__
5
6 #ifndef NVCC
```

```
7  #include <string>
8  #endif
9
10 #include <math.h>
11 #include "hoomd/HOOMDMath.h"
12 #include "hoomd/BoxDim.h"
13
14 /*! \file EvaluatorEField.h
15     \brief Defines the electric field for a nanopore found in the
       paper by Farahpour et al.
16 */
17
18 // need to declare these class methods with __device__ qualifiers
       when building in nvcc
19 // DEVICE is __host__ __device__ when included in nvcc and blank
       when included into the host compiler
20 #ifdef NVCC
21 #define DEVICE __device__
22 #else
23 #define DEVICE
24 #endif
25
26 //! Class for evaluating an electric field
27
28 class EvaluatorExternalFarahpour
29     {
30     public:
31
32         //! type of parameters this external potential accepts
33        //!typedef struct param{} param_type;
34         typedef Scalar param_type;
```

```
35        typedef Scalar3 field_type;
36
37        //! Constructs the constraint evaluator
38        /*! \param X position of particle
39            \param box box dimensions
40            \param params per-type parameters of external potential
41        */
42        DEVICE EvaluatorExternalFarahpour(Scalar3 X, const BoxDim&
  box, const param_type& params, const field_type& field)
43            : m_pos(X),
44              m_box(box),
45              m_field(field)
46            {
47                m_applied = params;
48            }
49
50        //! External Periodic doesn't need diameters
51        DEVICE static bool needsDiameter() { return false; }
52        //! Accept the optional diameter value
53        /*! \param di Diameter of particle i
54        */
55        DEVICE void setDiameter(Scalar di) { }
56
57        //! External Periodic doesn't need charges
58        DEVICE static bool needsCharge() { return true; }
59        //! Accept the optional diameter value
60        /*! \param qi Charge of particle i
61        */
62        DEVICE void setCharge(Scalar qi) { m_qi = qi; }
63
64        //! Declares additional virial cotribututions are needed for
```

```
 the external field
65          /*! No contribution
66          */
67          DEVICE static bool requestFieldVirialTerm() { return true; }
68
69          //! Evaluate the force, energy and virial
70          /*! \param F force vector
71              \param energy value of the energy
72              \param virial array of six scalars for the upper
    triangular virial tensor
73          */
74          DEVICE void evalForceEnergyAndVirial(Scalar3& F, Scalar&
    energy, Scalar* virial)
75              {
76
77
78              Scalar cx = 0;
79              Scalar cy = 0;
80              Scalar cz = 0;
81              Scalar pi = M_PI;
82
83              Scalar rx = m_pos.x - cx;
84              Scalar ry = m_pos.y - cy;
85              Scalar rz = m_pos.z - cz;
86
87              Scalar V0 =  m_field.x;
88              Scalar a = m_field.y;
89              Scalar c = m_field.z;
90
91
92
```

```
93
94          Scalar mu,nu,phi;
95          Scalar rho,d1,d2;
96          Scalar3 E;
97          Scalar pref;
98          Scalar factor;
99
100         rho=sqrt(rx*rx + ry*ry);
101         d1=sqrt( (rho+c)*(rho+c) + rz*rz);
102         d2=sqrt( (rho-c)*(rho-c) + rz*rz);
103
104
105         mu=fabs(acosh( (d1+d2)/(2*c)));
106         nu=acos( (d1-d2)/(2*c));
107
108         phi=atan2(ry,rx);
109
110         factor=V0/(pi*a*cosh(mu)*sqrt( sinh(mu)*sinh(mu) + sin(
    nu)*sin(nu) ) );
111         pref=1.0/sqrt( sinh(mu)*sinh(mu) + sin(nu)*sin(nu) );
112         if(rz<0){
113               E.x=-factor*pref*sinh(mu)*cos(nu)*cos(phi);
114               E.y=-factor*pref*sinh(mu)*cos(nu)*sin(phi);
115         }else{
116               E.x=factor*pref*sinh(mu)*cos(nu)*cos(phi);
117               E.y=factor*pref*sinh(mu)*cos(nu)*sin(phi);
118         }
119         E.z=factor*pref*cosh(mu)*sin(nu);
120
121         F = m_applied * E;
122
```

```
123             virial[0] = F.x*m_pos.x;
124             virial[1] = F.x*m_pos.y;
125             virial[2] = F.x*m_pos.z;
126             virial[3] = F.y*m_pos.y;
127             virial[4] = F.y*m_pos.z;
128             virial[5] = F.z*m_pos.z;
129             }
130
131         #ifndef NVCC
132         //! Get the name of this potential
133         /*! \returns The potential name. Must be short and all
    lowercase, as this is the name energies will be logged as
134             via analyze.log.
135         */
136         static std::string getName()
137             {
138             return std::string("efield");
139             }
140         #endif
141
142     protected:
143         Scalar3 m_pos;                  //!< particle position
144         BoxDim m_box;                   //!< box dimensions
145         Scalar m_qi;                    //!< particle charge
146         Scalar3 m_field;                //!< the field vector
147         Scalar m_applied;               //!< application of the field
148     };
149
150
151 #endif
```

The following Python code is defining a class that allows for control over the

parameters of the external potential header file at the Python interface of HOOMD. In other words, this script is adding the functionality we implemented in the HOOMD source code to the HOOMD Python API.

```
1
2  R""" External forces.
3
4  Apply an external force to all particles in the simulation. This
       module organizes all external forces.
5  """
6
7  from hoomd import _hoomd
8  from hoomd.md import _md
9  from hoomd.md import force
10 import hoomd
11
12 import sys
13 import math
14
15
16 """-------------------------------------------------------"""
17
18
19 class nanopore(_external_force):
20     R"""
21     """
22
23     def __init__(self, field, name=""):
24         hoomd.util.print_status_line()
25
26         # initialize the base class
27         _external_force.__init__(self, name)
```

```
28
29          # create the c++ mirror class
30          if not hoomd.context.exec_conf.isCUDAEnabled():
31              self.cpp_force = _md.PotentialPoreField(
32                  hoomd.context.current.system_definition, self.name)
33          else:
34              self.cpp_force = _md.PotentialPoreFieldGPU(
35                  hoomd.context.current.system_definition, self.name)
36
37          hoomd.context.current.system.addCompute(
38              self.cpp_force, self.force_name)
39
40          # setup the coefficient options
41          # changing this for farahpour
42          self.required_coeffs = ['epsilon', 'sigma', 'rpore', 'tpore'
    ]
43
44          self.field_coeff = tuple(field)
45
46      def process_coeff(self, coeff):
47          # pass;
48          epsilon = coeff['epsilon']
49          sigma = coeff['sigma']
50          rpore = coeff['rpore']
51          tpore = coeff['tpore']
52
53          lj1 = 4.0 * epsilon * math.pow(sigma, 12.0)
54          lj2 = 4.0 * epsilon * math.pow(sigma, 6.0)
55          return _hoomd.make_scalar4(lj1, lj2, rpore, tpore)
56
57      def process_field_coeff(self, field):
```

```
58          return _hoomd.make_scalar3(field[0], field[1], field[2])
59
60
61  """-----------------------------------------------------"""
```